THE UNIVERSITY OF CALGARY

An Ultra-Wideband Magnetic-Electric Dipole Antenna

and

A Shielded Slot Antenna

by

Tin Chau Choi

A THESIS

SUBMITTED TO THE FACULTY OF GRADUATE STUDIES

IN PARTIAL FULFILLMENT OF THE REQUIREMENTS FOR THE

DEGREE OF MASTER OF SCIENCE

DEPARTMENT OF ELECTRICAL AND COMPUTER ENGINEERING

CALGARY, ALBERTA

DECEMBER, 1998

0-612-38622-8

Abstract

The explosive growth of personal communications systems is leading to the proposed utilization of most of the electromagnetic spectrum. There is a need to find ways of increasing the bandwidth of the existing antennas or the development of new broadband antennas. Also, parallel with the increasing use of cellular telephones, public concern about their safety has grown.

Two novel ultra-wideband antennas and a shielded slot antenna have been researched and developed that are suitable for portable communications devices.

Both the computer simulations and the experimental measurements show that the two novel ultra-wideband antennas are extremely broadband. In addition to the broadband characteristics, the antennas include the advantages of compactness, robustness and high radiation efficiency. Computer simulations and the test results also show that the shielded slot antenna is an effective shielded radiator which has strong radiation on one side but significantly reduced radiation on the other side.

Acknowledgements

I would like to express my appreciation for the supervision and guidance of Dr. R. H. Johnston and for the invaluable knowledge he has shared with me. It is also appropriate to thank all the secretaries in the office of the Department of Electrical and Computer Engineering.

A special note of appreciation must go to the technicians of the University of Calgary, especially John Shelley, Warren Flaman, and Frank Hickli for their assistance in building the various antennas.

I would also like to thank TR Labs and the University of Calgary for providing the scholarship and funding which supported me during these years at school.

Finally, my deepest gratitude goes towards my family, especially Fanny for the typing and drawing of the diagrams.

Table of Contents

List of Tables

List of Figures

Chapter 8

List of Symbols and Abbreviations

A	magnetic vector potential
ANSI	American National Standards Institute
B_{ED}	susceptance of an electric dipole
C_{ED}	capacitance of an electric dipole
Coax	coaxial transmission line
dB	Decibels
$D(\theta,\phi)$	Directivity
$\underline{E}$	electric field vector
$\lvert E \rvert$	magnitude of electric field
$\mathbf{E}_A$	electric field due to the **A** potential
ED	electric dipole antenna
$\mathbf{E}_F$	electric field due to the **F** potential
E_x	electric field intensity in the x direction
E_y	electric field intensity in the y direction
E_z	electric field intensity in the z direction
f	Frequency
F	electric vector potential
FCC	Federal Communications Commission
G_{ED}	conductance of an electric dipole
GHz	gigahertz, 10^9 hertz
$\underline{H}$	magnetic field vector
$\mathbf{H}_A$	magnetic field due to the **A** potential
$\mathbf{H}_F$	magnetic field due to the **F** potential
I_{in}	input current
IEEE	Institute of Electrical and Electronics Engineering
j	imaginary number
J	electric current source
k	wave number

k_0	wave number in free space
kHz	kilohertz, 10^3 hertz
M	magnetic current source
MD	magnetic dipole antenna
MED	magnetic-electric dipole antenna
MHz	megahertz, 10^6 hertz
P_{in}	Power delivered to a network
P_L	power lost
P_{rad}	power radiated into free space
R_{ED}	radiation resistance of an electric dipole
R_L	loss resistance
R_{MD}	radiation resistance of a magnetic dipole
R_{rad}	radiation resistance
SAR	specific absorption rate
S_{11}	reflection coefficient, expressed as an S parameter
S_{21}	transmission coefficient, expressed as an S parameter
S_{11FS}	free space S_{11} value
S_{11wg}	waveguide S_{11} value
TEM	Transverse Electric-Magnetic
V_{in}	input voltage
VSWR	Voltage Standing Wave Ratio
w/g	Waveguide
Y_0	characteristic admittance of a transmission line
Z	intrinsic impedance of an unbounded medium
Z_{ED}	input impedance of an electric dipole
Z_{MD}	input impedance of a magnetic dipole
Z_0	characteristic impedance of a transmission line
ε	permittivity ($\varepsilon_r \varepsilon_0$)
ε_0	permittivity of free space, 8.854 x 10^{-12} F/m

ε_r	relative permittivity
η	intrinsic impedance of a medium (Section 2.2,2.4) or efficiency (Section 3.4)
λ	Wavelength
λ_g	wavelength in waveguide
λ_0	wavelength in free space
μ	Permeability
μ_0	permeability of free space, $4\pi \times 10^{-7}$ H/m
ρ	material density
σ	Conductivity
Ω	Ohms
ω	angular frequency, $2\pi f$

Chapter 1: Introduction

1.1 Background

Wireless communications play a more and more important role in our daily life today. Satellite TV permits people around the world to watch Olympic games, World soccer, and any news instantly. Cellular phones and pagers let people contact each other without geographical location limitation. Wireless modem, walkie-talkie, and radio broadcasting are also parts of our life. The various wireless apparatuses mentioned above, though different applications, all need a means of transferring energy or signal from the apparatus to free space in the form of electromagnetic waves or vice versa. A device used for this function is called an antenna. The function of an antenna when used at a transmitter is to convert the energy generated by a transmitter into a radiated electromagnetic wave. When used at the receiver, the function of an antenna is to convert the radiated wave into useful radio frequency energy for the receiver. There are many different kinds of antennas depending on the specific applications. For instance, an antenna for cellular phone is normally a one-quarter wavelength monopole with an omnidirectional radiation pattern. In the case of satellite TV, the antenna is a radio reflective, shallow parabolic reflector that concentrates the received signal to a focus point. It can be made of fine mesh wire, or be all metal, or have a shell of fiberglass with metal or wire mesh imbedded in it. Other antennas include microstrip antennas, slot antennas, loop antennas, aperture antennas, and horn antennas, etc.

1.2 Ultra-Wideband Antenna

The numerous applications of electromagnetic wave to the advancement of technology have necessitated the exploration and utilization of most of the electromagnetic spectrum. The need for an ultra-wideband antenna is fueled by the many possible applications of such a device. In addition, the advent of broadband systems has demanded the design of ultra-wideband antennas. A single ultra-wideband antenna can replace a large set of narrowband antennas that are normally used to cover the entire frequency band of interest. For example, this type of antenna is useful in satellite communications where space and weight are conserved by supporting many communication channels with only one antenna.

After many months of experimentation and extensive work, two novel ultra-wideband antennas have been developed. The antennas are made up of a parasitic electric dipole capacively coupled to a magnetic dipole. The resulting ultra-wideband magnetic-electric dipole antennas can be transformed into their equivalent monopole structures which are small enough to fit in many portable devices such as multi-channel cellular phones which require broadband applications. Chapter 2 covers background theory while experimental testing procedures can be found in Chapter 3. Chapter 4 contains details of the antenna development and Chapter 5 contains a summary of the results. Chapter 6 shows the transmission line model of the antennas and Chapter 9 contains conclusions and suggestions about future work that should be done on the antennas.

1.3 Shielded Slot Antenna

Cellular telephones are becoming widely used consumer products. In parallel with the wider use of such devices, public concern about their safety has grown. Many public controversies about health concerns as well as loss of property values have arisen over the siting of wireless communications base stations and satellite uplink dishes. More recently, health issues concerning the power, though much weaker than the power from the base stations, radiated from hand-held cellular phone unit have also become public controversies. Research on biological effects of electromagnetic radiation in radio and microwave frequencies dates back to before World War II [1]. In recent literature, a number of studies concerning electromagnetic energy absorption in the near field of antennas are cited. Several studies investigated the frequency range of hand-held devices between 300MHz and 3GHz. Experimental studies were performed on homogeneous phantom models or human models [2,3,4] and heterogeneous human models simulating anatomical details [5,6,7]. These models were either radiated by laboratory dipoles or commercially available transmitters. Numerical computations were performed simulating homogeneous or layered spheres human models [8].

Since the beginning of 1997, the U.S. Federal Communications Commission (FCC) requires the routine specific absorption rate (SAR) evaluation of mobile telecommunications devices prior to equipment authorization or use [9]. The specific absorption rate is defined as

$$SAR = \sigma|E|^2 / \rho$$

where σ is the conductivity and ρ is the material density. The ANSI/IEEE standard also suggests that the SAR averaged over any 1g of tissue for 30 minutes or more should remain under 1.6mW/g [10]. A paper using the finite-difference time-domain (FDTD) electromagnetic simulation approach to investigate the interaction between various commercial handset-mounted antennas and human tissue has found that for a head-handset separation of 2cm, the SAR in the head has a peak value between 0.9 and 3.8mW/g for 1W of delivered power [11]. Also, the head and hand absorb between 53 and 68% of the power delivered to the antenna. Another paper generally supports the results [12]. This means that more than half of the energy radiated from the cellular phone antennas is wasted. Battery life is a primary concern in portable units. A battery adds bulk and weight, so it is desirable to reduce the power absorbed by human tissue so that the phone units may be made more compact. In view of this, and the possible health effects, a shielded slot antenna (SSA) has been build after extensive computer simulations using WIPL-D. The proposed antenna is a dipole structure which can be transformed to its equivalent monopole structure to fit in a cellular phone unit. Chapter 7 contains details of the antenna development and Chapter 8 contains a summary of the experimental results. Chapter 9 contains the conclusions.

Notes

[1] K. R. Foster, "Health effects of electromagnetic fields: defusing the controversy," *Microwave Journal*, vol. 40, May 1997.

[2] Q. Balzano, O. Garay, and F. R. Steel, "Energy deposition in biological tissue near portable radio transmitters at VHF and UHF," *27th Conference IEEE Vehicular Technology Group*, March 1977, pp. 25-39.

[3] I. Chatterjee, Y. G. Gu, and O. P. Gandhi, "Quantification of electromagnetic absorption in humans from body-mounted communication transceivers," *IEEE Transactions Vehicular Technology*, vol. VT-34, May 1985, pp.55-62.

[4] A. W. Guy and C. K. Chou, "Specific absorption rates of energy in man models exposed to cellular UHF mobile-antenna fields," *IEEE Transactions Microwave Theory Technology*, vol. MTT-34, June 1986, pp. 671-680.

[5] S. S. Stuchly, M. A. Stuchly, A. Kraszewski, and G. W. Hartsgrove, "Energy deposition in a model of man: Frequency effects," *IEEE Transactions Biomedical Engineering*, vol. BME-33, July 1986, pp.702-711.

[6] M. A. Stuchly, A. Kraszewski, S. S. Stuchly, G. W. Hartsgrove, and R. J. Spiegel, "RF energy deposition in a heterogeneous model of man: Near-field exposures," *IEEE Transactions Biomedical Engineering*, vol. BME-34, Dec. 1987, pp.944-950.

[7] R. F. Cleveland and W. T. Athey, "Specific absorption rate (SAR) in models of the human head exposed to hand-held UHF portable radios," *Bioelectromagnetic*, vol. 10, Jan. 1989, pp.173-186.

[8] A. Hizal and Y. K. Baykal, "Heat potential distribution in an inhomogeneous spherical model of a cranial structure exposed to microwaves due to loop or dipole antennas," *IEEE Transactions Microwave Theory Technology*, vol. MTT-26, Aug. 1978, pp.607-612.

[9] K. Meier, V. Hombach, R. Kastle, R. Y. Tay, and N. Kuster, "The dependence of electromagnetic energy absorption upon human-head modeling at 1800MHz," *IEEE Transactions on Microwave Theory and Techniques*, vol. 45, no. 11, Nov. 1997.

[10] American National Standards Institute, IEEE C95.1-1991: *IEEE Standard for Safety Levels with Respect to Human Exposure to Radio Frequency Electromagnetic Fields, 3 kHz to 300 GHz*, 1991, Piscataway, NJ 08855-1331.

[11] M. A. Jensen and Y. Rahmat-Samii, "EM interaction of handset antennas and a human in personal comunications," *Proceedings of the IEEE*, vol. 83, no. 1, Jan. 1995.

[12] M. Okoniewski and M. A. Stuchly, "A study of the handset antenna and human body interaction," *IEEE Transactions on Microwave Theory and Techniques*, vol. 44, no. 10, Oct. 1996.

Chapter 2: Background Theory

2.1 Electric Dipole Antenna

Since electric dipole and magnetic dipole antennas are the essential and also the only building blocks of the ultra-broadband antennas presented in this thesis, we should review some of their basic properties and characteristics.

Figure 2.1 shows a simple half-wave electric dipole antenna.

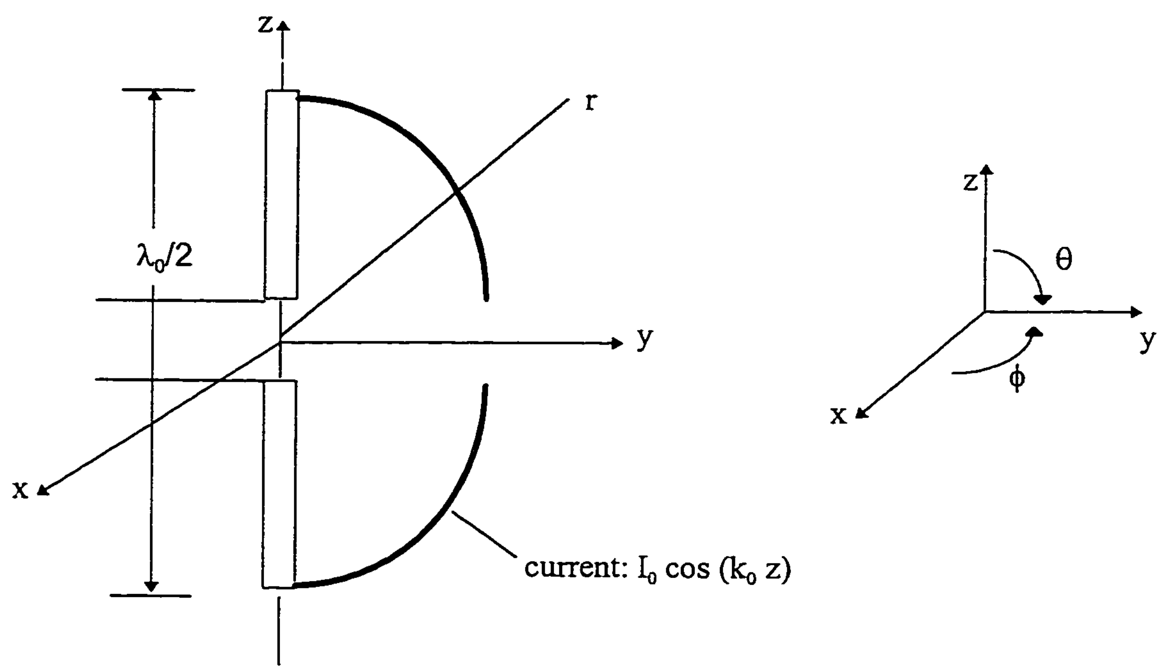

Figure 2.1 The half-wave electric dipole antenna.

Such a dipole is usually fed from a balanced two-wire transmission line or fed from an unbalanced coaxial cable through the use of a balun. Each arm of the antenna is about one-quarter wavelength long. It can be shown that the current distribution on a thin half-wave electric dipole antenna is closely approximated by a sinusoidal standing wave of the form

[1]:

$$I = I_0 \cos k_0 z \qquad -\lambda_0/4 \leq z \leq \lambda_0/4 \qquad (2\text{-}1)$$

where $k_0 = 2\pi/\lambda_0$ is the wave number, and λ_0 is the wavelength in free space. Such an electric dipole antenna is known as a standing wave antenna. The far-zone radiated $\underline{E}$ and $\underline{H}$ fields of the half-wave electric dipole antenna shown in Figure 2.1 can be found by equations (2-2) and (2-3) [1]:

$$\underline{E} = \frac{jI_0 Z_0}{2\pi r} \; e^{-jk_0 r} \; \frac{\cos(\frac{\pi}{2}\cos\theta)}{\sin\theta} \; \underline{a}_\theta \qquad (2\text{-}2)$$

and

$$\underline{H} = \frac{jI_0}{2\pi r} \; e^{-jk_0 r} \; \frac{\cos(\frac{\pi}{2}\cos\theta)}{\sin\theta} \; \underline{a}_\phi \qquad (2\text{-}3)$$

The radiation pattern in the $\underline{E}$ plane is shown in Figure 2.2 [1]. The half-power beam width is 78°.

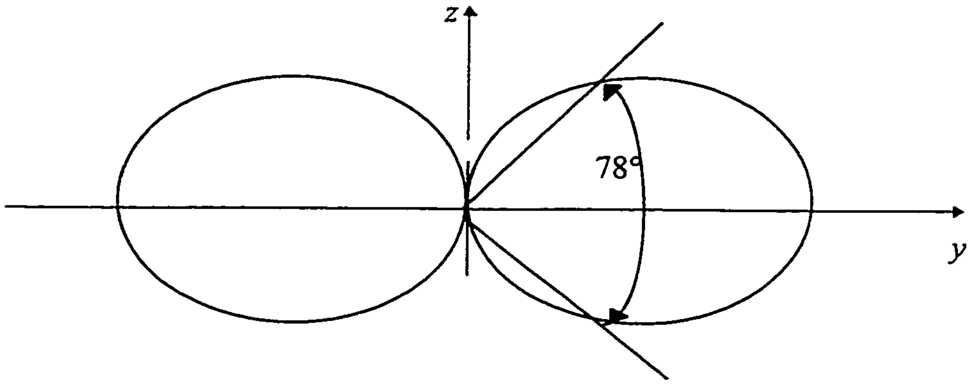

Figure 2.2 Principal E-plane radiation pattern for a half-wave electric dipole antenna.

The directivity function for the half-wave electric dipole antenna can be shown as [1]:

$$D(\theta,\phi) = 1.64\left[\frac{\cos(\frac{\pi}{2}\cos\theta)}{\sin\theta}\right]^2 \tag{2-4}$$

and the maximum directivity is 1.64.

The input impedance of an electric dipole antenna of total physical length l made from a cylindrical rod of various diameter d were measured by Brown and Woodward [2]. It can be seen that when $l/\lambda_0 \cong 0.48$, the reactance is zero and the radiation resistance is about 73Ω.

2.2 The Magnetic Dipole and the Duality Theorem

Before discussing the characteristics of a magnetic dipole antenna, we should understand one of the fundamental electromagnetic theorems, called Duality Theorem. A magnetic dipole is considered as the "dual" or the "complement" of an electric dipole of similar shape. The concept of the Duality Theorem can be summarized as:

> "When two equations that describe the behavior of two different variables are of the same mathematical form, their solutions will also be identical. The variables in the two equations that occupy identical positions are known as dual quantities and a solution of one can be formed by a systematic interchange of symbols to the other." [3]

The dual equations and their dual quantities are listed in Tables 2.1 and 2.2 for electric and magnetic sources, respectively [3].

Table 2.1 Dual Equations for Electric (J) and Magnetic (M) Current Sources

Electric Sources ($\mathbf{J} \neq 0, \mathbf{M} = 0$)	**Magnetic Sources ($\mathbf{J} = 0, \mathbf{M} \neq 0$)**
$\nabla \times \mathbf{E}_A = -j\omega\mu\mathbf{H}_A$	$\nabla \times \mathbf{H}_F = j\omega\varepsilon\mathbf{E}_F$
$\nabla \times \mathbf{H}_A = \mathbf{J} + j\omega\varepsilon\mathbf{E}_A$	$-\nabla \times \mathbf{E}_F = \mathbf{M} + j\omega\mu\mathbf{H}_F$
$\nabla^2\mathbf{A} + k^2\mathbf{A} = -\mu\mathbf{J}$	$\nabla^2\mathbf{F} + k^2\mathbf{F} = -\varepsilon\mathbf{M}$
$\mathbf{A} = \frac{\mu}{4\pi}\iiint_v J\frac{e^{-jkR}}{R}dv'$	$\mathbf{F} = \frac{\varepsilon}{4\pi}\iiint_v M\frac{e^{-jkR}}{R}dv'$
$\mathbf{H}_A = \frac{1}{\mu}\nabla \times \mathbf{A}$	$\mathbf{E}_F = -\frac{1}{\varepsilon}\nabla \times \mathbf{F}$
$\mathbf{E}_A = -j\omega\mathbf{A} - j\frac{1}{\omega\mu\varepsilon}\nabla(\nabla\bullet\mathbf{A})$	$\mathbf{H}_F = -j\omega\mathbf{F} - j\frac{1}{\omega\mu\varepsilon}\nabla(\nabla\bullet\mathbf{F})$

Table 2.2 Dual Quantities for Electric (J) and Magnetic (M) Current Sources

Electric Sources ($\mathbf{J} \neq 0, \mathbf{M} = 0$)	Magnetic Sources ($\mathbf{J} = 0, \mathbf{M} \neq 0$)
$\mathbf{E}_A$	$\mathbf{H}_F$
$\mathbf{H}_A$	$-\mathbf{E}_F$
$\mathbf{J}$	$\mathbf{M}$
$\mathbf{A}$	$\mathbf{F}$
ε	μ
μ	ε
k	k
η	$1/\eta$
$1/\eta$	η

Duality theorem can be used in an abstract manner to explain the operations and characteristics of a magnetic dipole antenna when compared to an electric dipole antenna because the motion of magnetic charges giving rise to magnetic currents can be explained, when compared to their dual quantities of moving electric charges creating electric currents. However, it should be noted that the Duality Theorem is only a mathematical tool, and magnetic charges and currents are purely fictitious quantities which do not exist in nature.

Back to the discussion of the magnetic dipole antenna. A narrow slot, one-half wavelength long, cut in a conducting sheet of metal, is the dual of a half-wave electric dipole antenna. This magnetic dipole is shown in Figure 2.3.

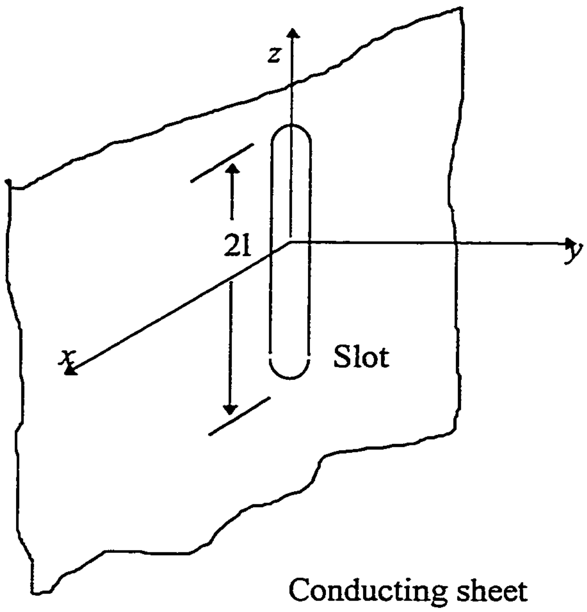

Figure 2.3 Magnetic dipole antenna which is the dual of a half-wave electric dipole.

Figure 2.4 shows one of the feeding arrangements and the electric field distribution across the slot of the magnetic dipole antenna.

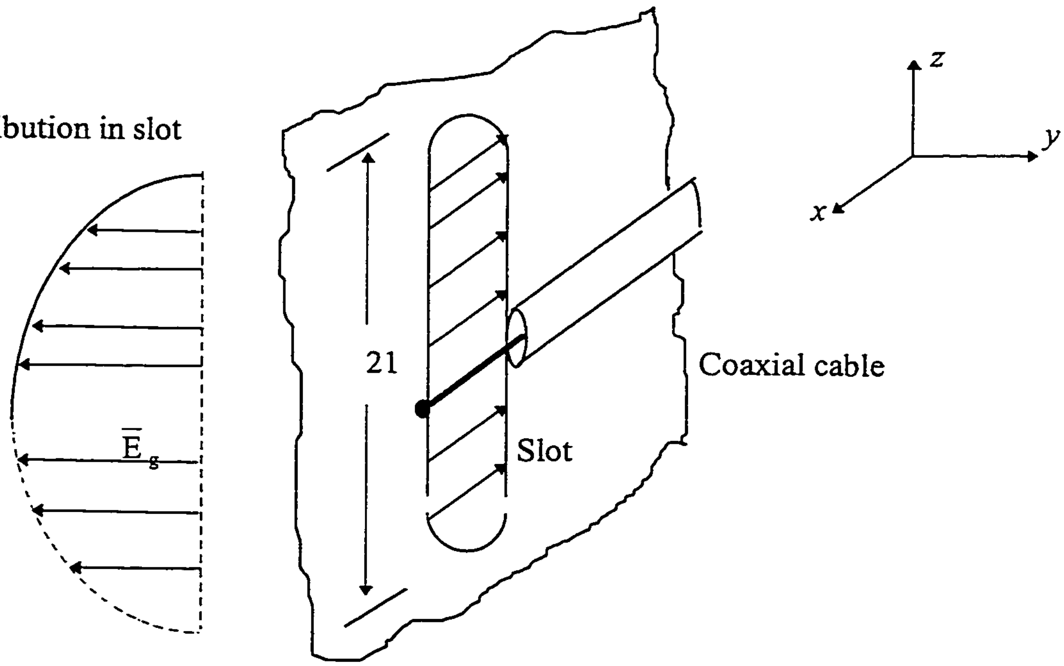

Figure 2.4 The $\underline{E}$ field distribution and feeding network of the magnetic dipole antenna.

The electric field across the slot has a standing wave pattern, and can be expressed by [4]:

$$E = E_g \sin(k_0(l-|z|)) \tag{2-5}$$

The far-zone radiated fields of the magnetic dipole antenna shown in Figure 2.3 can be deduced from the field equations of the half-wave electric dipole antenna (equations 2-2 and 2-3) by applying the Duality Theorem. The details of the mathematics are covered in [4].

$$\underline{H} = j \frac{I_{mo} Y_o}{2\pi r} e^{-jk0r} \frac{\cos(\frac{\pi}{2}\cos\theta)}{\sin\theta} \underline{a}_\theta \tag{2-6}$$

and

$$\underline{E} = -j \frac{I_{mo}}{2\pi r} e^{-jk0r} \frac{\cos(\frac{\pi}{2}\cos\theta)}{\sin\theta} \underline{a}_\phi \tag{2-7}$$

Note the dual nature of the radiated fields between the electric and magnetic dipoles, i.e., the interchange of the role of $\underline{E}$ and $\underline{H}$ in equations (2-2) and (2-6), (2-3) and (2-7). The radiation pattern and directivity of the magnetic dipole antenna are the same as those for the electric dipole antenna. The magnetic dipole antenna in Figure 2.3 will become resonant when its length is about $0.5\lambda_0$. At resonant, the radiation resistance will be [4]:

$$R_{MD} = Z_0^2/4R_{ED} = 377^2/(4\times 73) = 487\Omega$$

where R_{MD} and R_{ED} are the radiation resistance of the magnetic and electric dipole antennas respectively and Z_0 is the intrinsic impedance of free space. The above expression involves the Babinet's principle which will be discussed in section 2.4.

2.3 Other Shapes of Electric and Magnetic Dipole Antennas

Besides the simple shapes shown in Figure 2.1 and 2.3, electric and magnetic dipole antennas can take many other shapes. Some of them are shown in Figure 2.5.

(a)

(b)

(c)

Figure 2.5 Some of the dual pairs of electric and magnetic dipole antennas.

The electric dipole antenna shown in Figure 2.5 (a) is called the "bow-tie" antenna. It is a simple approximation to the very broadband biconical antenna. The details of the biconical and bow-tie antenna are covered in [5] and [6]. Figure 2.5 (b) shows a dual pair of "H" shape electric and magnetic dipole antennas. Dubost [7] has studied the characteristics of the "H" shape magnetic dipole antenna intensively. The input impedance of the dual pair in Figure 2.5 (a) and (c) were measured experimentally and will be covered in Chapter 4 since they constitute the final antenna in this thesis.

2.4 Babinet's Principle

As discussed in section 2.2, an electric dipole antenna and the corresponding magnetic dipole antenna form a dual pair, or are referred to as complementary structures of each other. When combined together, they form a single solid screen with no overlap; therefore, one may ask if there is any relationship between them. If the answer is yes, how are they related? The question can be answered by Babinet's principle which in optics states that:

> "When the field behind a screen with an opening is added to the field of a complementary structure, the sum is equal to the field when there is no screen." [8]

Figure 2.6 illustrates an extension of Babinet's principle for antenna theory [8].

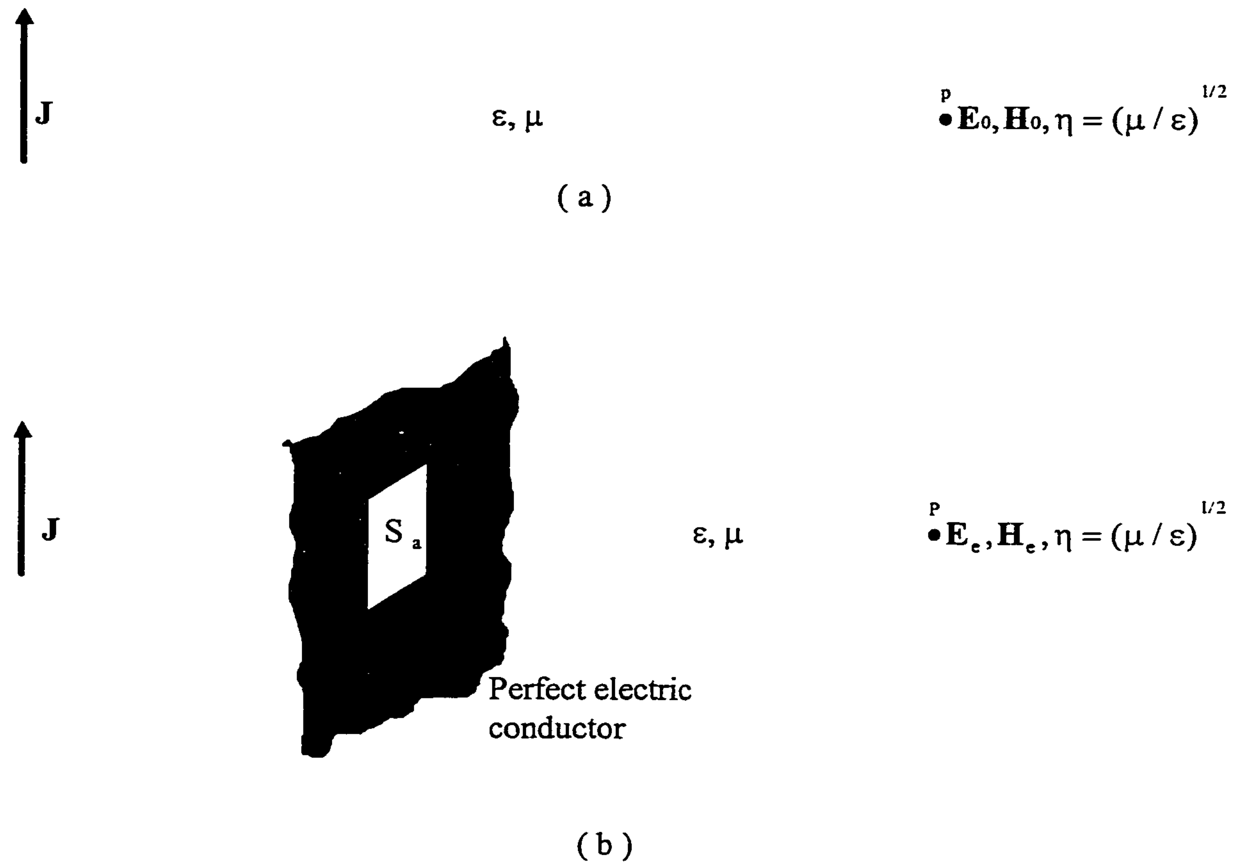

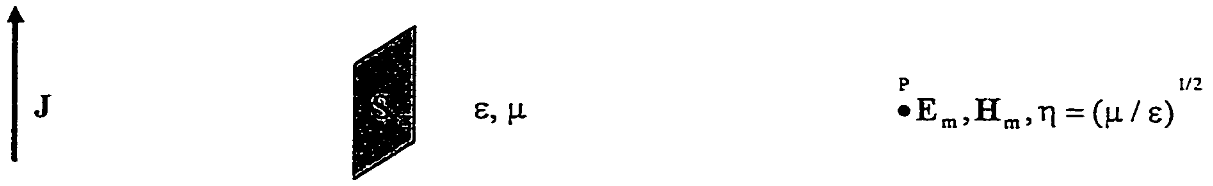

(c)

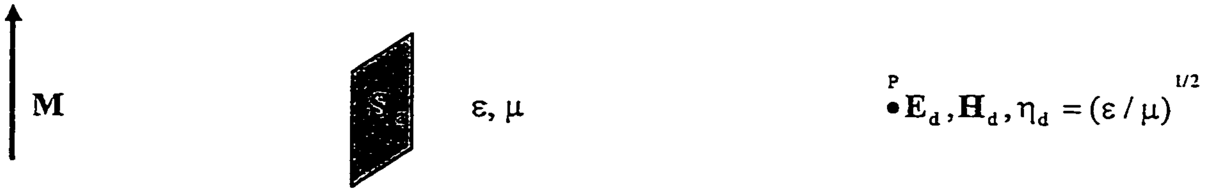

(d)

Figure 2.6 Illustration of the extension of Babinet's principle.

Referring to Figure 2.6 (a), if an electric source **J** radiates into an unbounded medium of intrinsic impedance $\eta = (\mu/\varepsilon)^{1/2}$ and produces at point P the fields $\underline{E}_0$, $\underline{H}_0$, the same fields can be obtained by combining the fields when the electric source **J** radiates in a medium of intrinsic impedance $\eta = (\mu/\varepsilon)^{1/2}$ in the presence of :

1. an infinite, planar, very thin, perfect electric conductor with a slot S_a, which produces at P the fields $\underline{E}_e$, $\underline{H}_e$ as in Figure 2.6 (b), and
2. a flat, very thin, perfect magnetic conductor S_a, which produces at P the fields $\underline{E}_m$, $\underline{H}_m$ as in Figure 2.6 (c).

That is,

$$\underline{E}_0 = \underline{E}_e + \underline{E}_m \qquad (2\text{-}8)$$

$$\underline{H}_0 = \underline{H}_e + \underline{H}_m \tag{2-9}$$

One can obtain Figure 2.6 (d) from Figure 2.6 (c) by applying the duality theorem in Section 2.2. Referring to Table 2.2, we can replace **J** by **M**, $\mathbf{E}_m$ by $\mathbf{H}_d$, $\mathbf{H}_m$ by -$\mathbf{E}_d$, ε by μ, and μ by ε. As a result, we can obtain the same fields in Figure 2.6 (a) by combining the fields of Figure 2.6 (b) and a magnetic source **M** radiating in a medium with intrinsic impedance $\eta_d = (\varepsilon/\mu)^{1/2}$ in the presence of a flat, very thin, perfect electric conductor S_a, which produce at P the fields $\underline{E}_d$, $\underline{H}_d$ as in Figure 2.6 (d).

That is,

$$\underline{E}_0 = \underline{E}_e + \underline{H}_d \tag{2-10}$$

$$\underline{H}_0 = \underline{H}_e - \underline{E}_d \tag{2-11}$$

Equation (2-8) to (2-11) may be considered as the scattering version of Babinet's principle; however, for the purpose of this thesis, it is more relevant to look at the impedance version of Babinet's principle. Consider a dual pair of electric and magnetic dipole antennas of arbitrary shape shown in Figure 2.7.

(a) (b)

magnetic dipole electric dipole

Figure 2.7 A dual pair of (a) magnetic dipole and (b) electric dipole antenna.

The magnetic dipole is excited across the gap ab, and the electric dipole is excited across the gap cd. Their input impedances are related by [9]

$$Z_{MD}Z_{ED} = Z^2/4 \tag{2-12}$$

where Z_{MD} and Z_{ED} are the input impedance of the magnetic dipole and the electric dipole in Figure 2.7(a) and (b) respectively. $Z = \sqrt{\frac{\mu}{\varepsilon}}$ is the intrinsic impedance of the unbounded medium where both dipoles are situated.

The magnetic dipole considered so far in this section is a slot of arbitrary shape cut into a plane conductor which is flat, very thin and infinite in size. It is obvious that such a conductor is not realizable in practice. However, if the plane conductor, where the slot cut into, is large compared to the wavelength and the dimensions of the slot, the behavior predicted by Babinet's principle can be realized to a high degree; and the impedance properties of the slot may not be affected as much by the finite dimensions of the plane as would be its pattern [8]. Far away from the slot, the currents will go to nearly zero; at that point, the conducting sheet may be cut away.

We can see from equation (2-12) that Z_{MD} and Z_{ED} always have opposite reactances. Therefore, if we combine the electric and magnetic dipoles into a single antenna, the resultant input reactance might be tuned out or reduced to some extent, so that a broadband characteristic can be achieved. This is the fundamental idea of the magnetic-electric dipole antenna in this thesis.

2.5 Image Theory

To analyze the performance of an antenna near an infinite plane conductor, virtual source (image) will be introduced to account for the reflections as shown in Figure 2.8 [10].

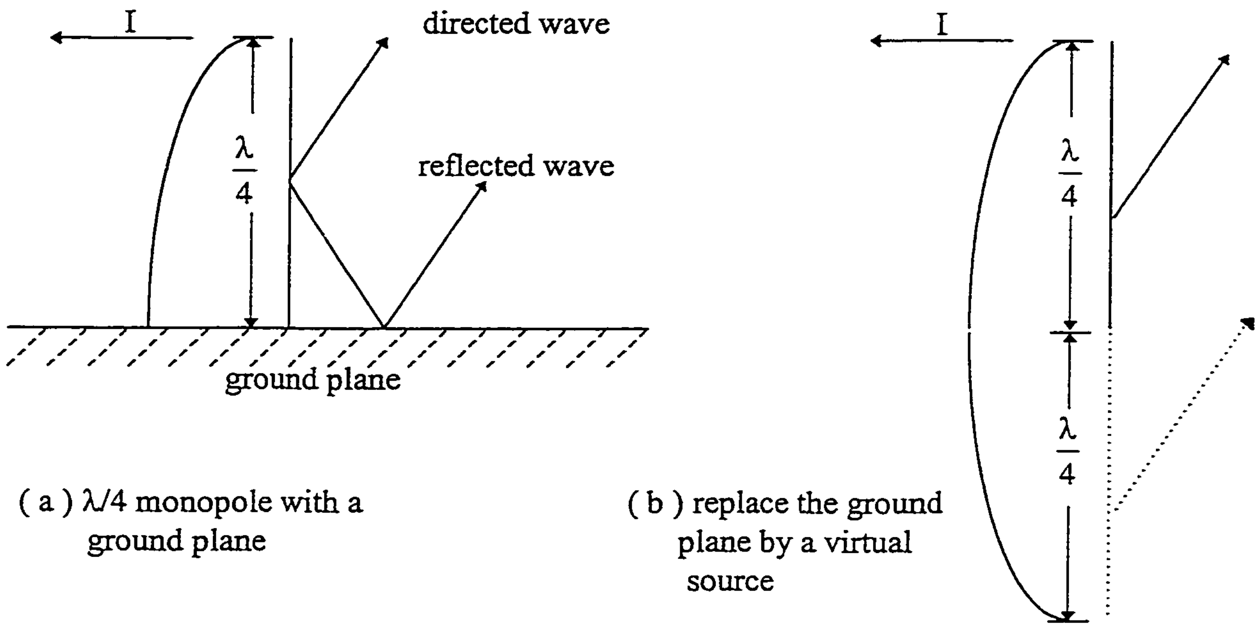

(a) λ/4 monopole with a ground plane

(b) replace the ground plane by a virtual source

Figure 2.8 Illustration of Image Theory.

The virtual source in Figure 2.8 (b) combined with the real source to form an equivalent system as in Figure 2.8 (a). The equivalent system gives the same radiated field on and above the ground plane as the actual system. However, the fields below the ground plane in the actual system is zero, and so the equivalent system does not give the correct field below the ground plane. We can transform a half-wave dipole antenna to an equivalent λ/4 monopole with a ground plane through the image theory.

Notes

[1] R. E. Collin, *Antennas and Radiowave Propagation*, McGraw-Hill, 1985, pp. 32-38.

[2] G. H. Brown and O. M. Woodward, Jr., "Experimentally determined impedance characteristics of cylindrical antennas," *Proceedings. IRE*, vol. 33, 1945, pp. 257-262.

[3] C. A. Balanis, *Antenna Theory : Analysis and Design*, John Wiley & Sons, 1997, pp. 126-127.

[4] R. E. Collin, *Antennas and Radiowave Propagation*, McGraw-Hill, 1985, pp. 261-265.

[5] C. A. Balanis, *Antenna Theory : Analysis and Design*, John Wiley & Sons, 1997, pp. 442-450.

[6] R. E. Collin, *Antennas and Radiowave Propagation*, McGraw-Hill, 1985, pp. 87-93.

[7] G. Dubost, *Flat Radiating Dipoles and Applications to Arrays*, John Wiley & Sons, 1981, pp.48-59.

[8] C. A. Balanis, *Antenna Theory : Analysis and Design*, John Wiley & Sons, 1997, pp. 616-620.

[9] Y. T. Lo and S. W. Lee, *Antenna Handbook : Antenna Fundamentals and Mathematical Techniques*, Chapman & Hall, 1993, pp. 2-13 to 2-16.

[10] C. A. Balanis, *Antenna Theory : Analysis and Design*, John Wiley & Sons, 1997, pp. 164-165.

Chapter 3: Measurement Procedures

3.1 The Network Analyzer

The input impedance, input reflection coefficients, and S parameters for near field, radiation pattern and efficiency measurements of the proposed antennas were measured with a Hewlett Packard™ HP 8720C network analyzer. It can make accurate measurements over a broad frequency range, from 50MHz to 20GHz, with a frequency resolution of 100kHz. Figure 3.1 illustrates an antenna measurement setup.

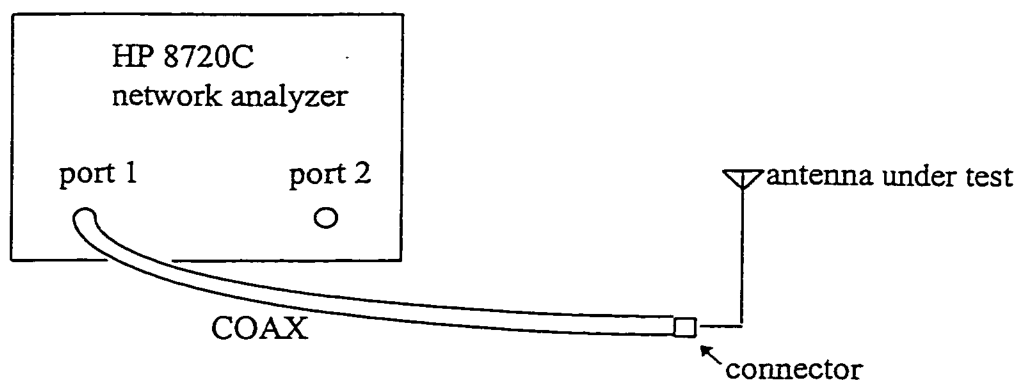

Figure 3.1 Antenna Measurement Setup

In any high frequency measurement, there are certain measurement errors associated with the system that contribute uncertainty to the results. Some of the errors come from interconnecting cables and connectors which introduce variations in magnitude and phase that can mask the actual performance of the antenna under test. Therefore, before any measurement, the network analyzer must be calibrated. During calibration, the analyzer measures the magnitude and phase response of known standard devices, and compares the measurement with actual antenna data [1]. It uses the results to effectively remove the systems errors from the measurement data of the test antenna. The known standard devices used for calibration are 85052D 3.5mm Economy calibration kit which includes the following standards: opens, shorts and broadband loads. During calibration, the above standards are replaced in turn according to the on-screen menu of the analyzer. To obtain high accuracy, step measurements are made with 201 data points and an averaging factor of 16. Calibrations are always performed relative to the connection point nearest to the antenna, so that any phase change included by the connecting cables and connectors are removed.

3.2 Near-field Measurement

The space surrounding an antenna is usually subdivided into three regions: (a) reactive near-field, (b) radiation near-field (Fresnel) and (c) far-field (Fraunhofer) regions as shown in Figure 3.2 [2], Far-field (Fraunhofer) region

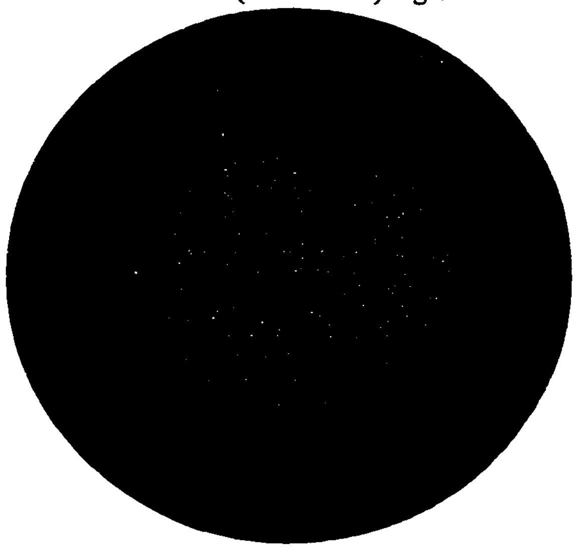

$$R_1 = 0.62\sqrt{D^3/\lambda}$$

$$R_2 = 2D^2/\lambda$$

D is the largest dimension of the antenna.

Figure 3.2 Field regions of an antenna.

The boundaries separating these regions are not unique, and there are various criteria used to identify the regions.

The near field information of the Magnetic-Electric Dipole Antenna in Chapter 4 is of less interest in practice; therefore, the near field measurement was only performed on the shielded slot antenna (SSA) for hand-held phone in Chapter 7, where the near field information is the main issue. Based on the near field measurement, one can estimate in a relative sense the specific absorption rate (SAR) in the head of the mobile phone user.

Figure 3.3 is the experimental setup for near field measurement.

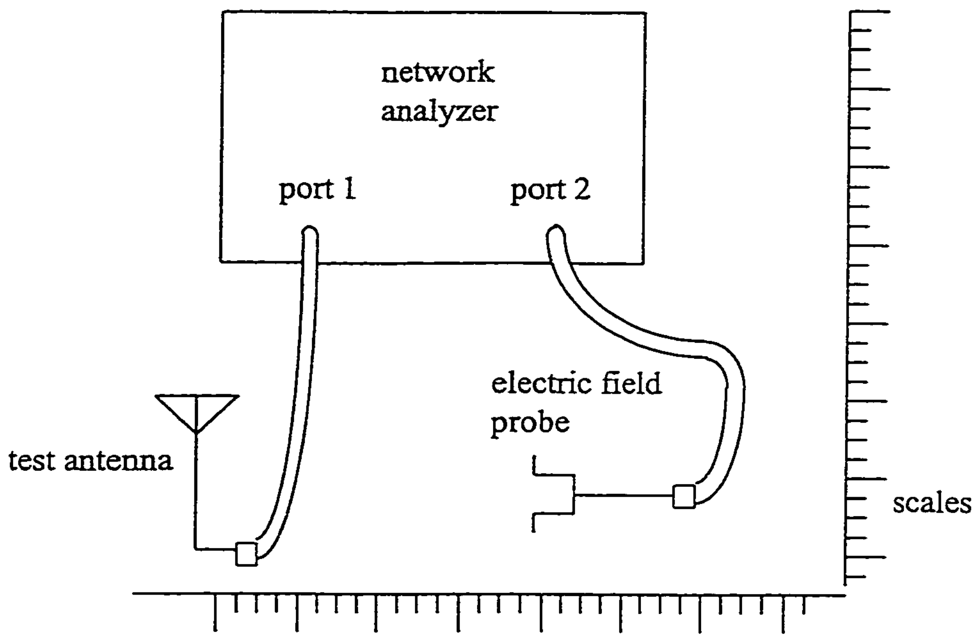

Figure 3.3 Near field measurement setup.

During the experiment, the test antenna is fixed, and the electric field probe is moved along the x, y and z coordinates. The S_{21} data are measured and recorded. To minimize fluctuations, all measurements were averaged 16 times.

3.3 Radiation Pattern Measurement (Far-field)

Radiation pattern measurements were performed inside an anechoic chamber so that multipath interference can be eliminated. Figure 3.4 illustrates the experimental setup.

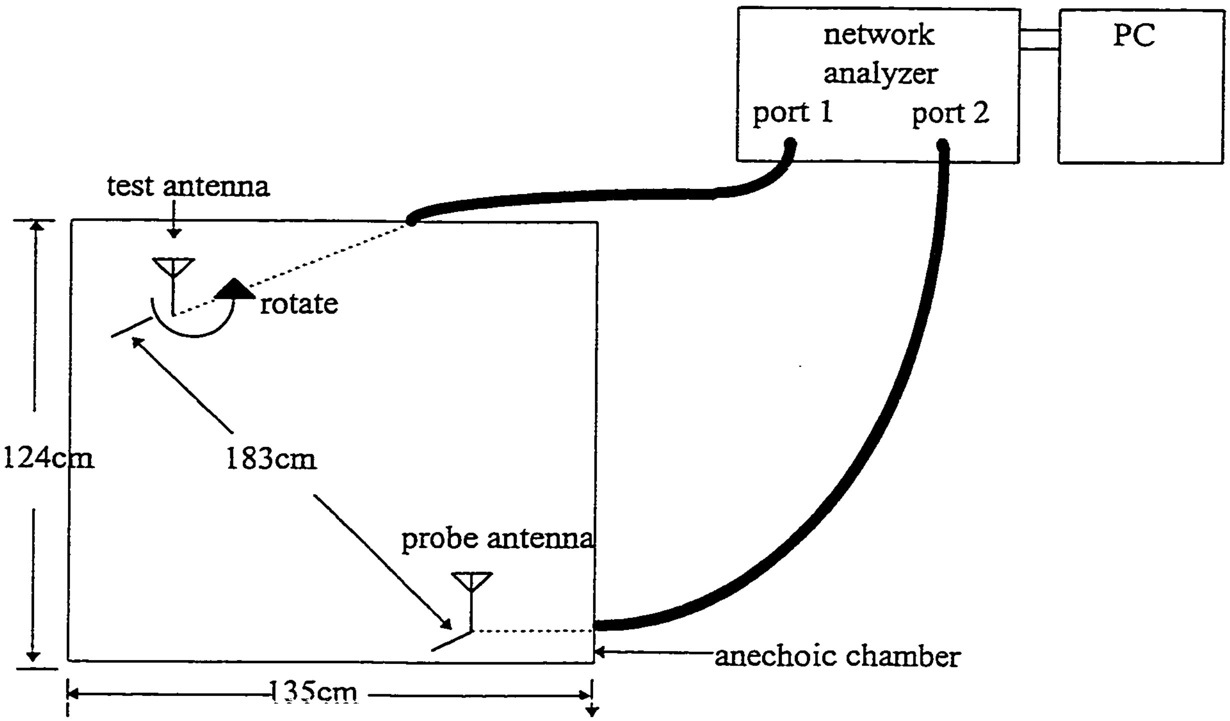

Figure 3.4 Radiation pattern measurement setup (top view).

Inside the anechoic chamber, the bottom is a metal plane surface, the remaining five surfaces are made up of absorbing foams in the shape of triangular pyramids. The test antenna was mounted on a rotor underneath such that the antenna under test can be rotated 360° in a horizontal plane. Both the test antenna and the probe antenna were connected to the network analyzer through coaxial cables. A PC was used to control and monitor the rotation of the test antenna, and to record the measured data (S_{21}). The measured S_{21N} data were then normalized by the maximum value such that $|S_{21Nnor}| = |S_{21N}| / |S_{21max}|$. $|S_{21Nnor}|$ then can be plotted versus the angle (0° - 360°) on a polar graph.

3.4 Efficiency Measurement

Antenna efficiency is an important parameter in a communication system. It is defined as the power delivered to the load (radiation into free space) relative to the power delivered to the network (power input to the antenna less the power reflected from the antenna) [3, 4],

$$\eta = \frac{P_{rad}}{P_{in}} = \frac{P_{rad}}{P_{rad} + P_L} = \frac{R_{rad}}{R_{rad} + R_L} \tag{3-1}$$

where P_{rad} = power radiated into free space

P_{in} = power delivered to the network

P_L = power lost

R_{rad} = radiation resistance

R_L = loss resistance.

The Wheeler Cap method is regarded as the most accurate and simple for determining the efficiency of a small simple antenna [3, 4, 5]. The method assumes that the test antenna is modeled as series loss and radiation resistances, which poses limitation on the application of the method. Moreover, the data generated from the Wheeler Cap method may be interpreted in three different ways which can give three significantly different answers for efficiency [6]. In view of this, a new method called reflection method was used for efficiency measurement in this thesis. For the theory behind the reflection method, one can refer to the reference [6].

The measurements were performed inside a rectangular waveguide with internal dimensions of 303mm x 172mm with a length of 2182mm. This gives a practical frequency operating range from about 500MHz to 900MHz. In this frequency range, the waveguide is operating in the $TE_{1,0}$ mode only. See Figure 3.5. The experimental procedures are performed as follows.

(1) Measure S_{11FS} in the free space (2) Place matched load (absorber) in the output end of the w/g, and adjust input sliding short so that S_{11wg} inside w/g is approximately equal to S_{11FS}, then fix the input sliding short in this position (Figure 3.5 (a)). (3) Adjust output sliding short in different positions (normally 10 positions) and record S_{11wgN} (N = 1, 2, ...10) in those positions. See Figure 3.5. (b). The total movement of the output sliding short should span about $\lambda_g/2$ where λ_g is the guide wavelength.

Top view

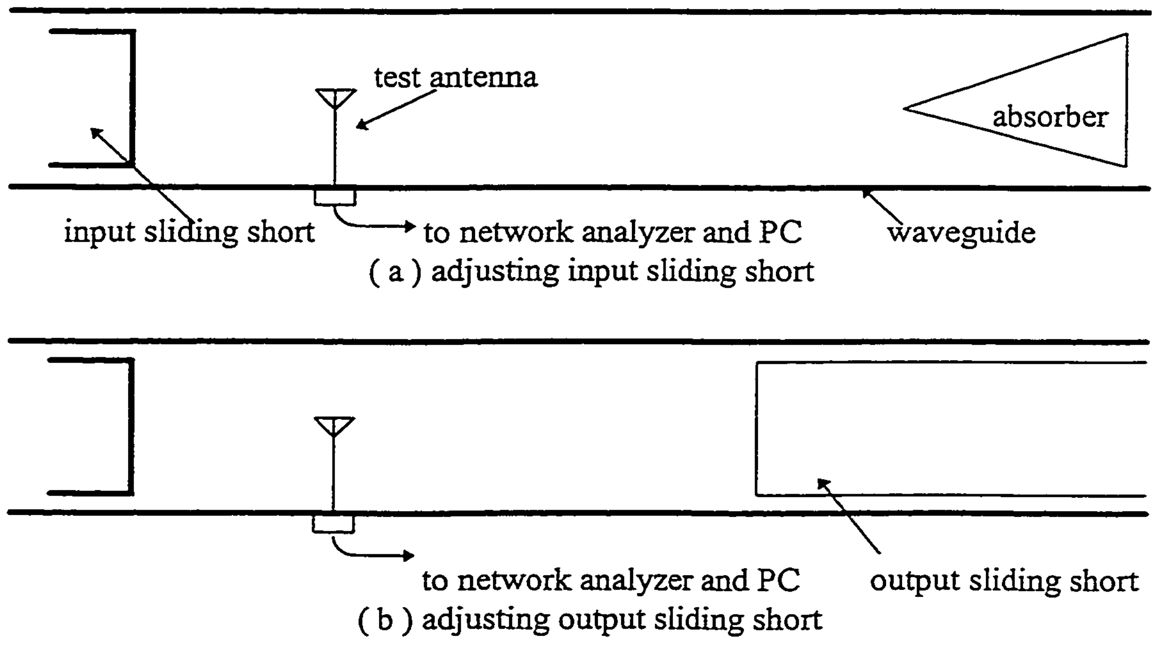

Figure 3.5 Measuring antenna efficiency by the reflection method

The S_{11wgN} values are used to determine a graphical circle. A Matlab program is written that fits a circle through the measured S_{11wgN} points with minimum square error. A typical result is shown in Figure 3.6.

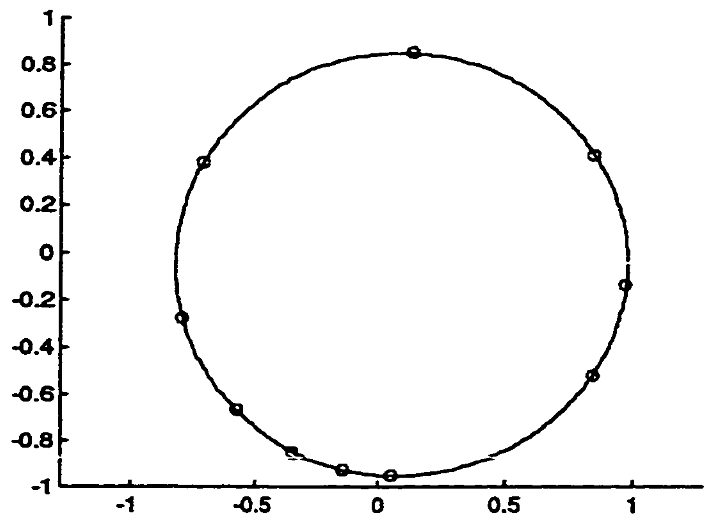

Figure 3.6 Measured input scattering parameter values (circles) with numerically fitted circle (solid line)

After the circle has been plotted and the antenna's S_{11FS} is located on the Smith Chart, two quantities, Δ_{Smin} and Δ_{Smax} can be determined as shown in Figure 3.7.

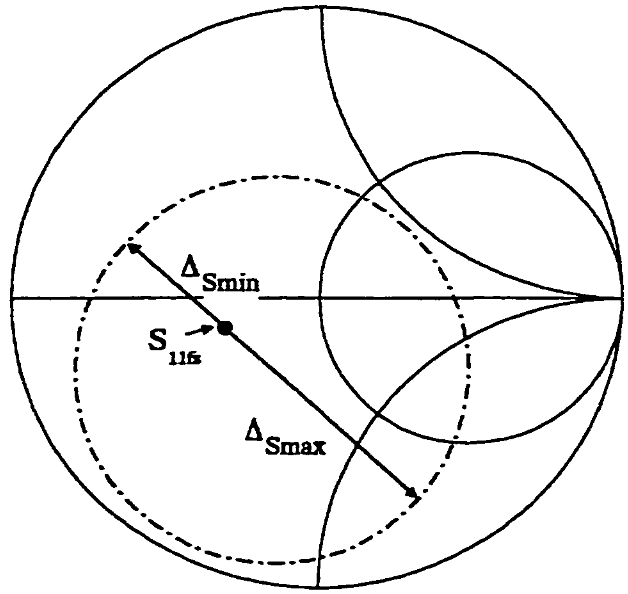

Figure 3.7 Determining the delta values needed to calculate efficiency

and finally the efficiency is calculated as

$$\eta = \frac{2}{(\Delta_{S\min})^{-1} + (\Delta_{S\max})^{-1}} \bullet \frac{1}{\left(1 - |S_{11FS}|^2\right)} \tag{3-2}$$

a Matlab program is also written to calculate and plot η over the desired frequency range once S_{11wgN} and S_{11FS} are obtained.

Notes

[1] *Hewlett Packard HP 8720C Network Analyzer Operating Manual*, Hewlett-Packard Company, 1992.

[2] Y. T. Lo and S. W. Lee, *Antenna Handbook : Antenna Fundamentals and Mathematical Techniques*, Chapman & Hall, 1993, pp. 1-16 to 1-18.

[3] D. M. Pozar and B. Kaufman, "Comparison of three methods for the measurement of printed antenna efficiency," *IEEE Communications*, vol. 36, no. 1, Jan. 1988, pp. 136-139.

[4] E. H. Newman, P. Bohley, and C. H. Walter, "Two methods for the measurement of antenna efficiency," *IEEE Transactions on antenna & propagation*, vol. AP-23, no. 4, July 1975, pp. 457-461.

[5] H. A. Wheeler, "The radiansphere around a small antenna," *Proceedings IRE*, Aug. 1959, pp. 1325-1331.

[6] R. H. Johnston and J. G. McRory, "An improved small antenna efficiency measurement method," *IEEE AP-S magazine*, Oct. 1998.

Chapter 4: Antenna Development

4.1 Magnetic-Electric Dipole Antenna

Examining Equation (2-12) in Section 2.4 again, we have

$$Z_{MD}Z_{ED} = Z^2/4 \qquad (2\text{-}12)$$

where Z_{MD} and Z_{ED} are the input impedance of the magnetic dipole and the corresponding complementary electric dipole respectively. $Z = \sqrt{\mu / \varepsilon}$ is the intrinsic impedance of the unbounded medium where both dipoles are situated, and is equal to 377Ω in free space.

We can deduct that Z_{MD} and Z_{ED} always have opposite reactance. Thus one might think that *if a magnetic dipole and its complementary electric dipole are combined in some ways to form a single radiating structure, and by carefully design their relative dimensions and spacing, the total input reactance of the resulting single antenna might be tuned out or reduced to some extent in a wide range of frequency. The combination of the magnetic dipole and the electric dipole are a more effective radiator into free space than either one individually.* The above concept is the fundamental idea of the Magnetic-Electric dipole antenna in this thesis.

4.2 Design steps and Prototype of the Magnetic-Electric Dipole Antenna

Having proposed the above concept, one should next decide:

1) what are the shapes of the constituent electric dipole and magnetic dipole

2) how should they be coupled together to form a single antenna

3) how should the resultant antenna be fed

It is very natural to use the most simple shape, a rectangular strip and the complimentary rectangular slot, as the constitute electric dipole and magnetic dipole to construct a prototype Magnetic-Electric dipole antenna. The rectangular strip and the rectangular slot used are shown in Figure 4.1.

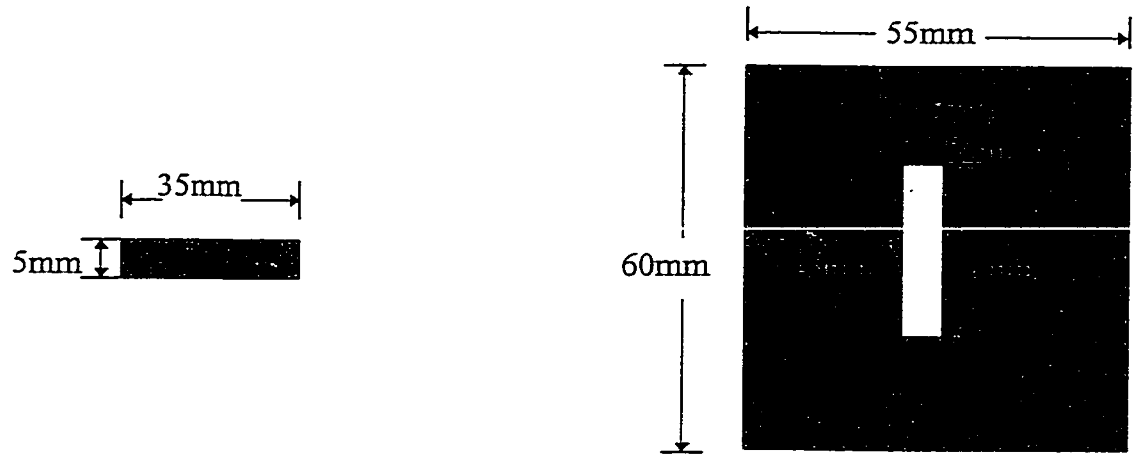

(a) ED　　　　(b) MD

Figure 4.1 (a) Electric dipole (ED) and (b) Magnetic dipole (MD) of the prototype Magnetic-Electric dipole antenna.

Note that the electric dipole and the magnetic dipole in Figure 4.1 form a complimentary pair; and of course, the metallic plane used to construct the magnetic dipole is finite in size. The dimensions of the strip and the slot were arbitrarily chosen.

It is known that the bandwidth of the antenna can be increased proportionately by reducing the dielectric constant [1, 2, 3], and also it is desirable to keep the separation between the electric dipole and the magnetic dipole as minimum as possible to make the antenna more compact and also to allow a better coupling between the two constituent dipoles. A low dielectric spacer was then sandwiched between the electric and magnetic dipole. The function of the spacer is to avoid direct electrical contact, but allow maximum coupling between the electric dipole and the magnetic dipole.

It is clear from Figure 2.6, Equations (2-8) and (2-9) (Section 2.4, Babinet's principle) that if we arrange the antenna in a way such that the rectangular strip and the rectangular slot are aligned, the resulting radiated fields would be as if there is no antenna. It does not make sense to construct an antenna in this way. It is intuitive to conclude that maximum radiation would be achieved if the rectangular strip is orthogonal to the rectangular slot. In this arrangement, the $\underline{E}$ and $\underline{H}$ fields of the individual electric and magnetic dipoles will reinforce each other. The structure of the resulting prototype is shown in Figure 4.2. The dimensions are the same as Figure 4.1.

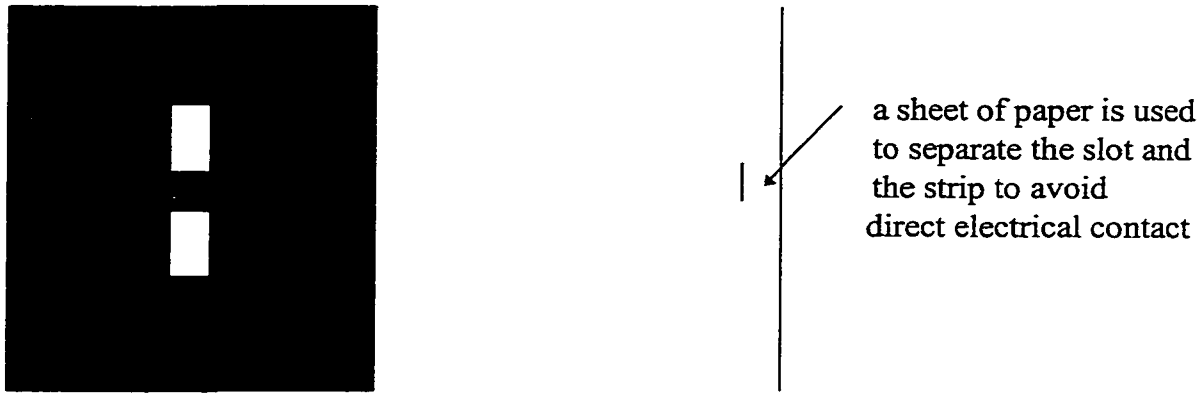

(a) Front view (b) Side view

Figure 4.2 Prototype of the Magnetic-Electric Dipole

This is a single feed antenna; we can feed either the rectangular strip or the rectangular slot. Babinet's principle tells us that the resulting radiated fields would be the same in both cases. It is desirable to feed the slot since the resulting structure will be more robust. Figure 4.3 shows the prototype of the magnetic-electric dipole with the feeding network.

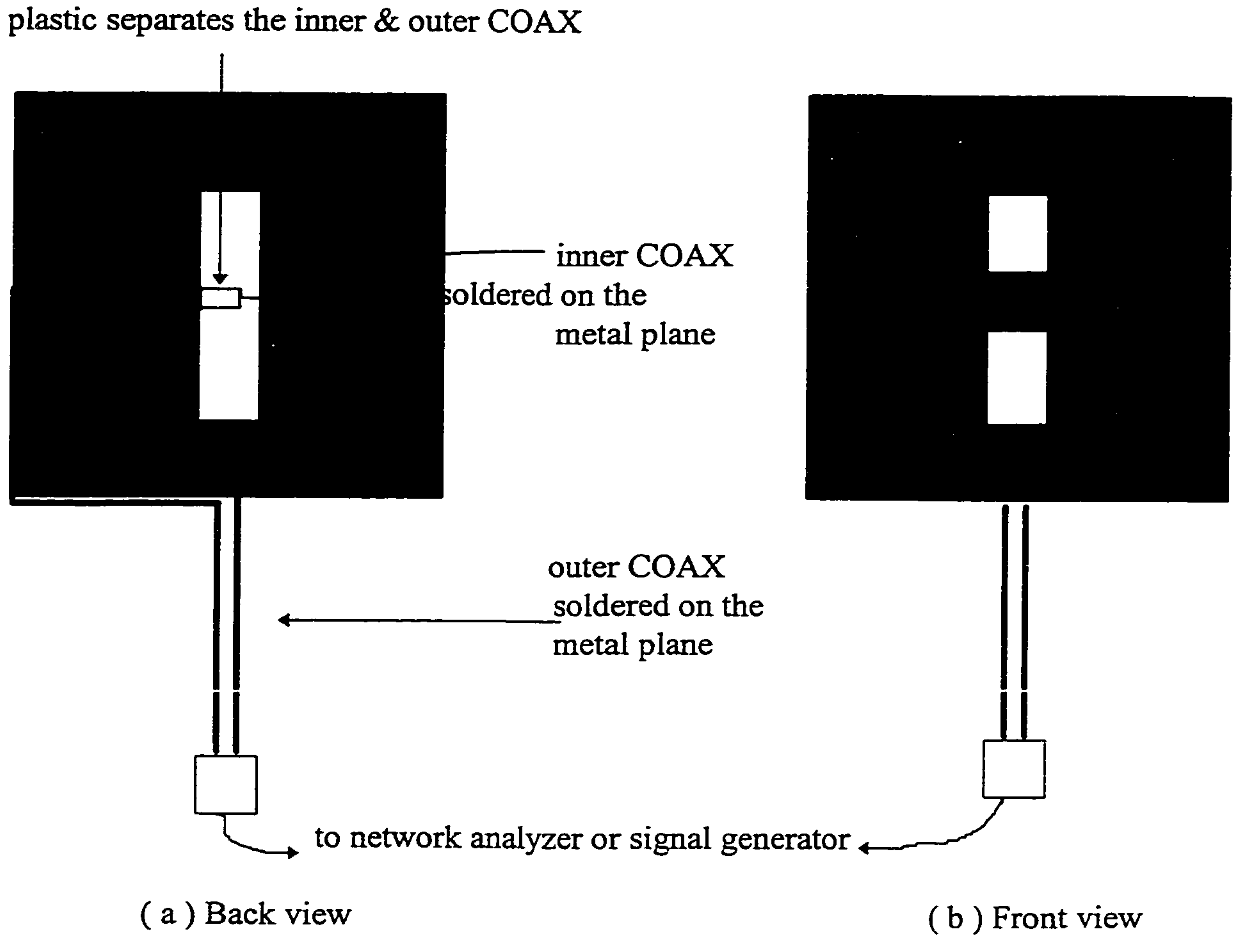

Figure 4.3 Prototype of the Magnetic-Electric dipole with the feeding network.

A potential difference is created across the gap of the slot (a-b). There are two reasons to bend and wrap the coax around as shown in Figure 4.3 (a) : (1) to make the coax feed orthogonal to the rectangular strip (the electric dipole) so that the E field of the antenna will not induce any current flowing on the coax; otherwise, the coax feed would radiate and become part of the antenna; (2) to create a plane of zero potential which is perpendicular to the metal plane and passes through the rectangular slot, so that we can transform the above Magnetic-Electric dipole into an equivalent monopole structure with a ground plane through the Image Theory as shown in Figure 4.4. Image Theory was discussed earlier in section 2.5.

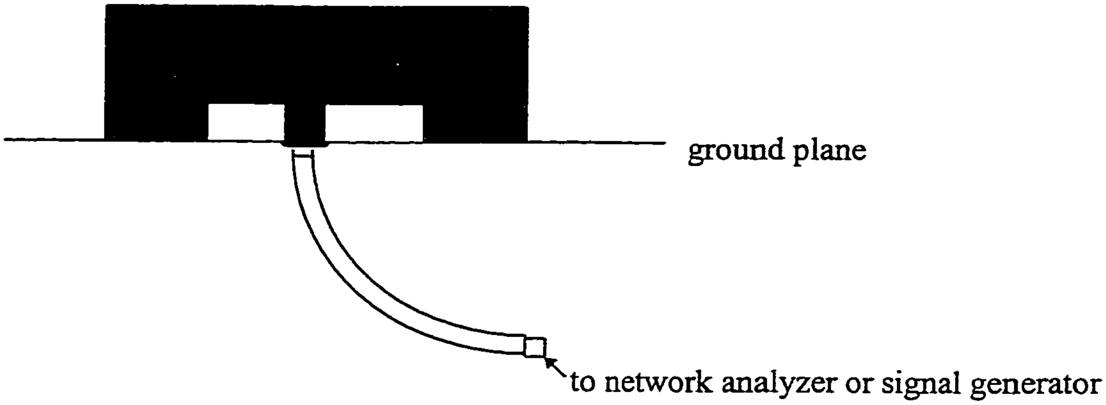

Figure 4.4 The equivalent monopole structure of Figure 4.3.

The monopole structure is a more common and practical structure than the corresponding dipole structure for portable equipments, such as cellular phones. The former one is easier to feed, has a better isolation to the rest of the electronic circuit due to the ground plane, and is only half the height of the other one.

Consider now the prototype antenna of the Magnetic-Electric dipole shown in Figure 4.3. We will now try to verify the concept that we can create a broadband antenna by coupling a slot (MD) and its complimentary (ED) in the proper way. Figure 4.5 shows the input impedance of the magnetic dipole of Figure 4.1 (b) on a Smith Chart from 1.0GHz to 4.0GHz. The input impedance was measured at the feed point (a-b in Figure 4.3 (a)) which is located across the gap at the middle of the slot. The measurement procedure was described in Chapter 3.

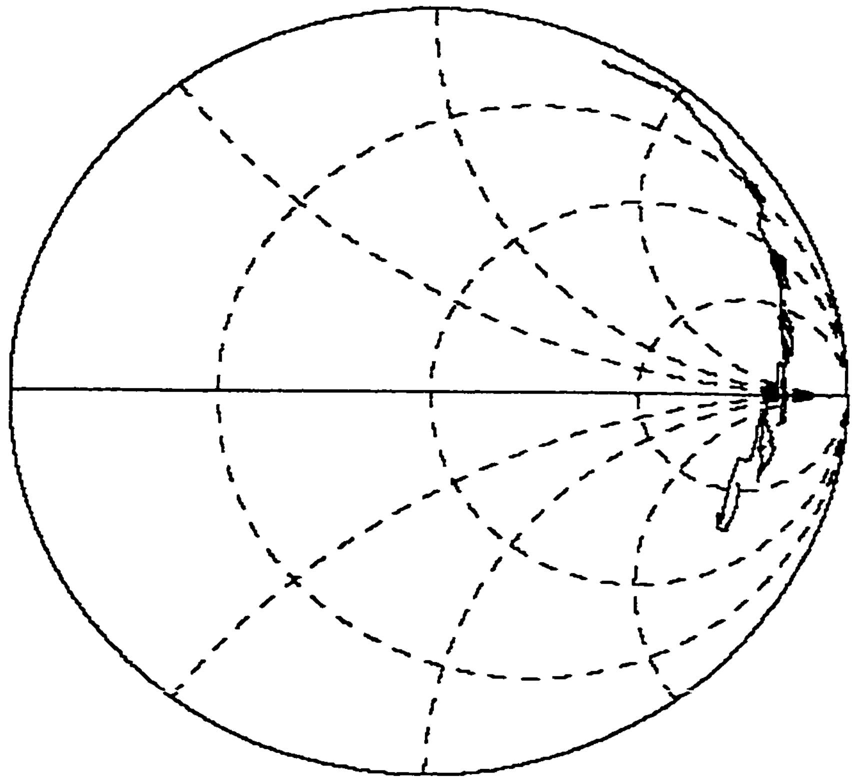

Figure 4.5 Measured input impedance of the magnetic dipole of Figure 4.1 (b)

The input impedance locus is far away from the center of the Smith Chart, which is the 50Ω point, indicating that the magnetic dipole working alone has a poor match to 50Ω from 1.0GHz to 4.0GHz. Next, we coupled the slot (magnetic dipole) and its complementary metallic strip (electric dipole) together and used a dielectric sheet to sandwich between them as depicted in Figure 4.2. Figure 4.6 shows the resulting input impedance locus across the same feed point a-b in Figure 4.3 (a).

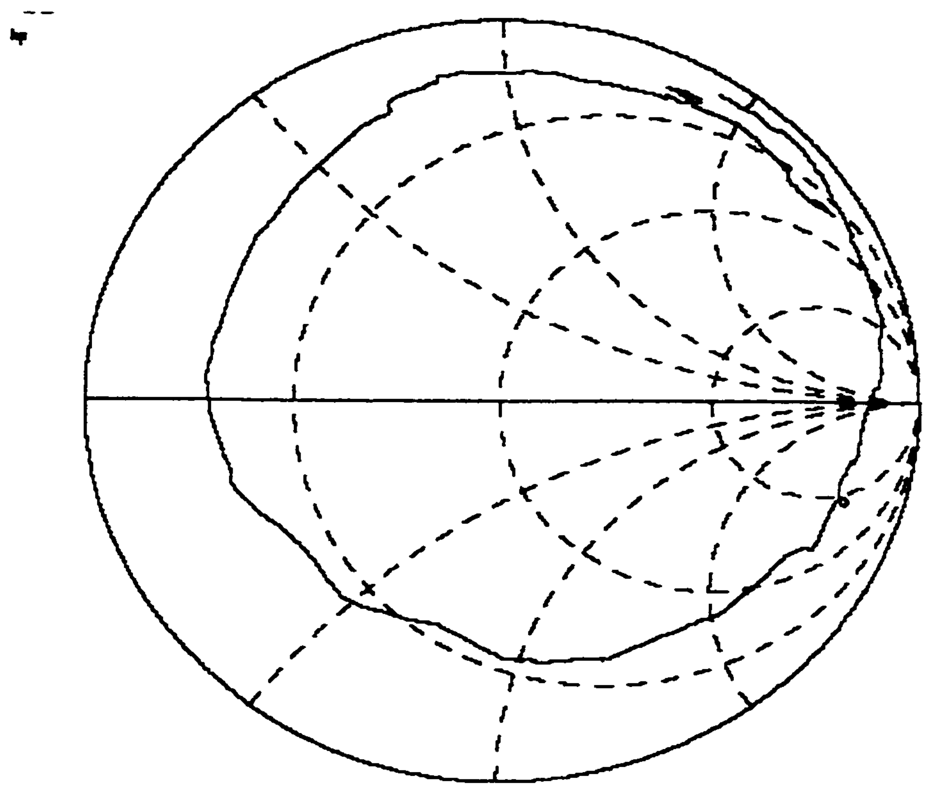

Figure 4.6 Measured input impedance of the magnetic-electric dipole of Figure 4.2

The impedance locus forms a big single loop around the outer edge of the Smith Chart which indicates that the reflection coefficient is very large. This implies that the coupling between the slot and the strip is very small and also the radiation is poor. Figure 4.7 shows the corresponding S_{11} plot or return loss plot of the above antenna.

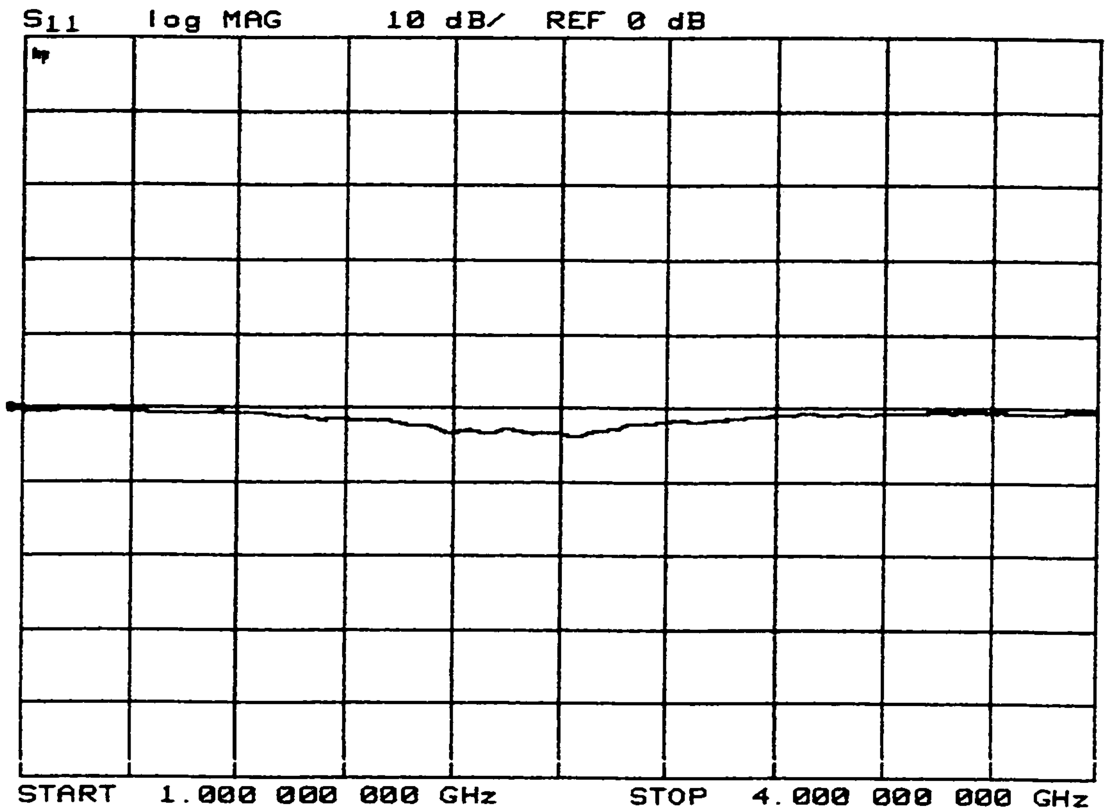

Figure 4.7 Measured return loss of the magnetic-electric dipole of Figure 4.2

The scale is 10dB per division, and we can see from the plot that the best matching point is only around 3dB loss. Then, the thin dielectric was replaced by thicker dielectric such that the spacing between the slot and the strip was 6mm. The thicker dielectric has an ε_r that is essentially one that is very similar to free space, and so its influence is expected to be negligible. The thicker dielectric is used to adjust the spacing between the slot and the strip only. The input impedance locus is shown in Figure 4.8.

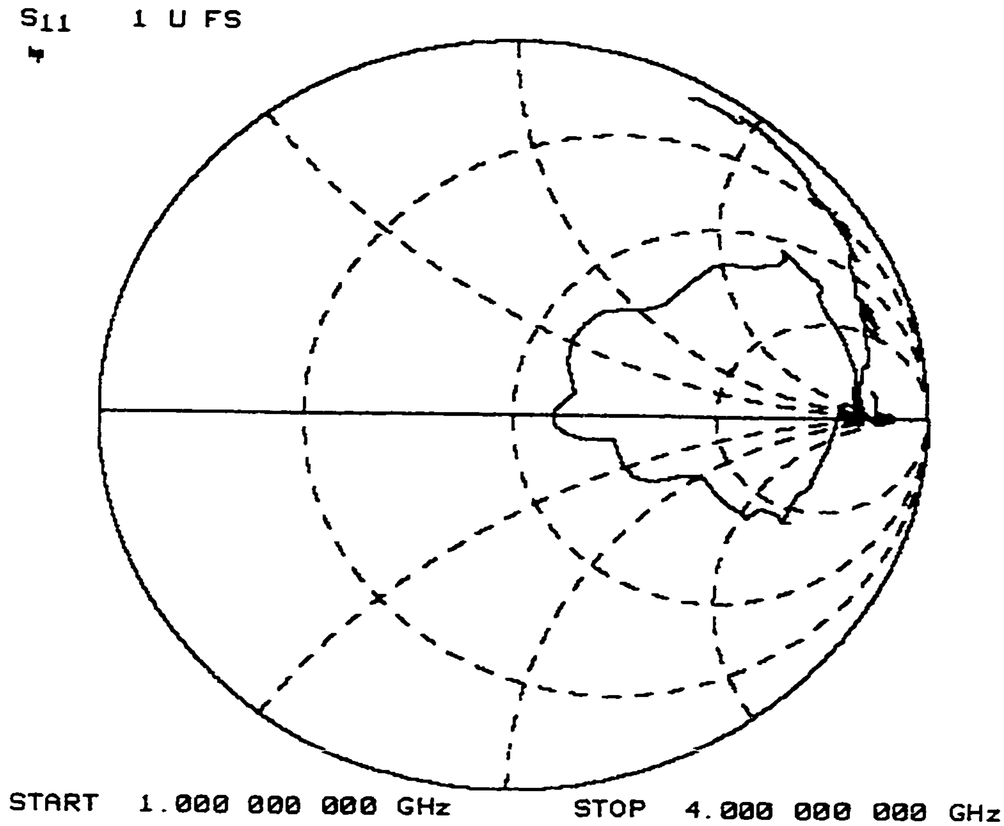

Figure 4.8 Measured input impedance of the magnetic-electric dipole of Figure 4.3 with an electric dipole spacing of 6mm

It can be deducted that the coupling is much better than the previous case since the locus is closer to the center of the Smith Chart. Figure 4.9 is the corresponding return loss plot, where the 10dB bandwidth extends from about 3.20GHz to 3.38GHz which is 5.5% of the centre frequency, or corresponds to a bandwidth ratio of 1:1.06. It is obvious that the response is far better than the previous case where the best matching point is only around 3dB.

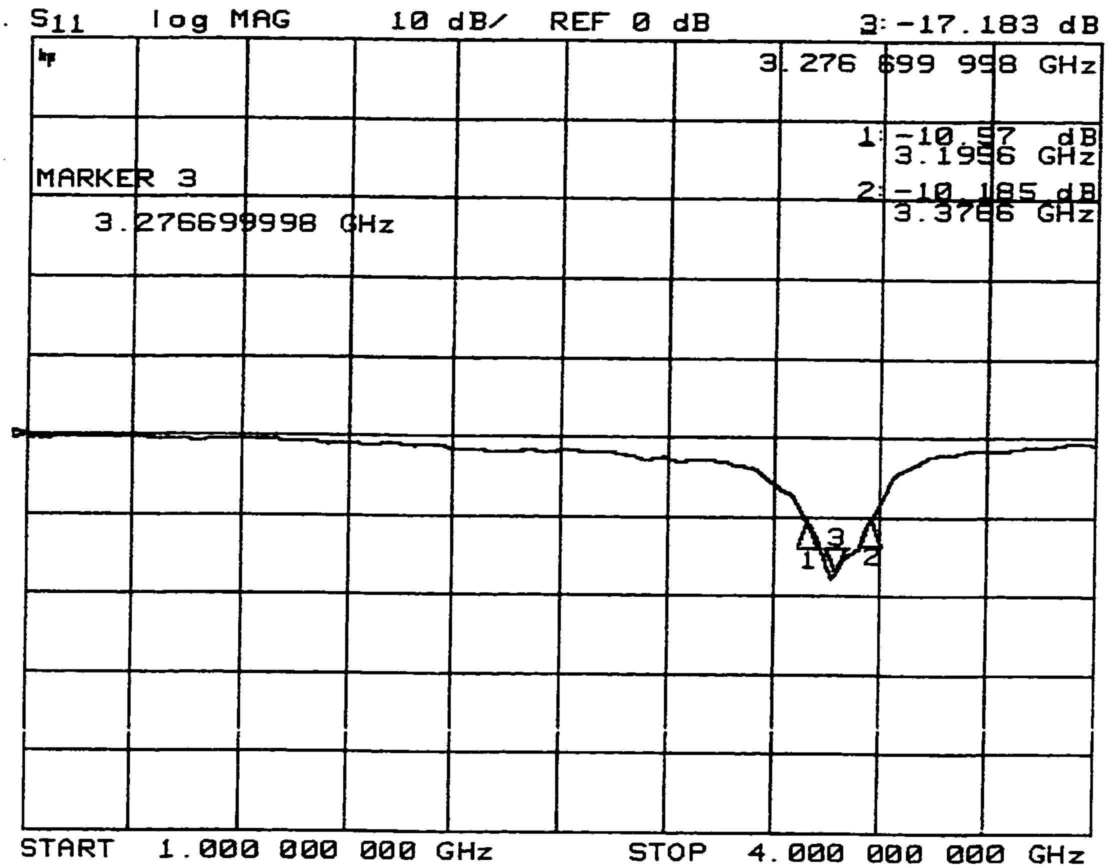

Figure 4.9 The corresponding measured return loss plot of Figure 4.8

Ideally, we want the input impedance locus of an antenna to loop around, close to the centre of the Smith Chart. In Figure 4.8, the loop is on the right hand side of the centre which implies that the resistive components are too high whereas in Figure 4.6, the resistive components are too small. By observing these two figures, we can deduct that the closer the spacing between the slot and the strip, the smaller the resistive components would be. Since 6mm spacing is too much (the resistive part is too large), we tried a 4mm dielectric spacer. Figure 4.10 shows the resulting input impedance.

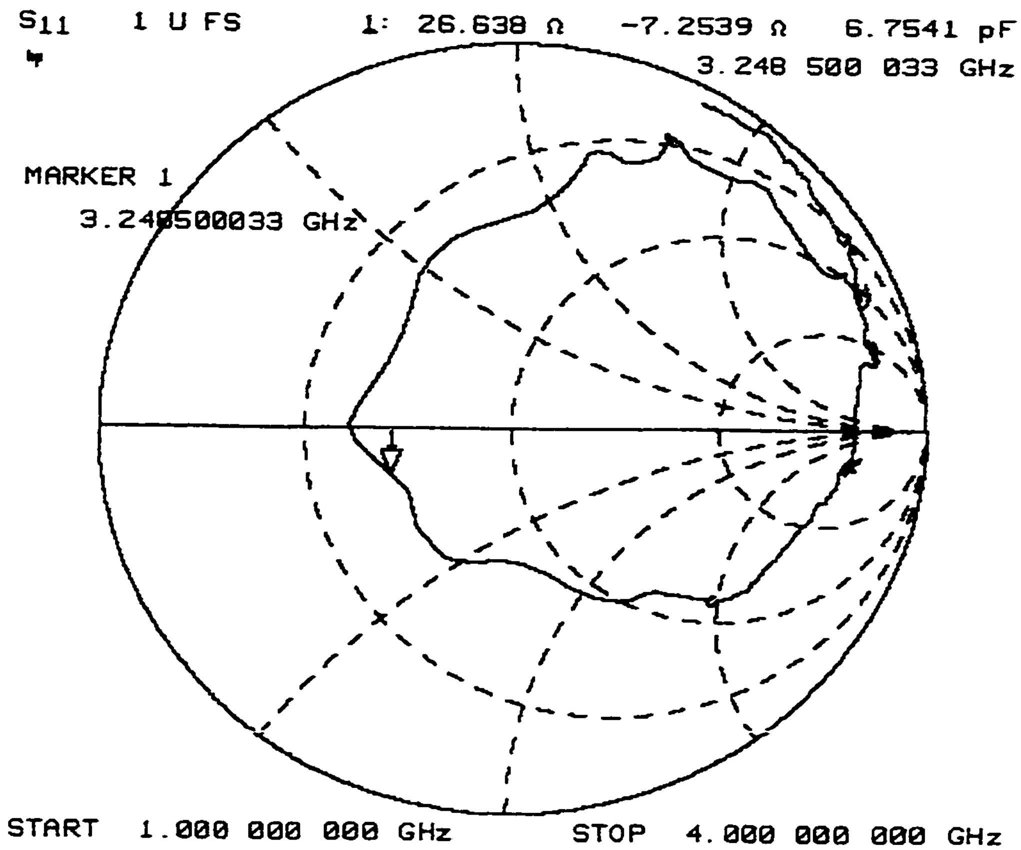

Figure 4.10 Measured input impedance of the magnetic-electric dipole of Figure 4.2 with an electric dipole spacing of 4mm

As predicted, the loop is somewhere between Figure 4.6 and 4.8. The corresponding return loss plot is shown in Figure 4.11, where the best matching point is 10dB; and so the return loss response is more broad band but not as deep as the 6mm spacing case.

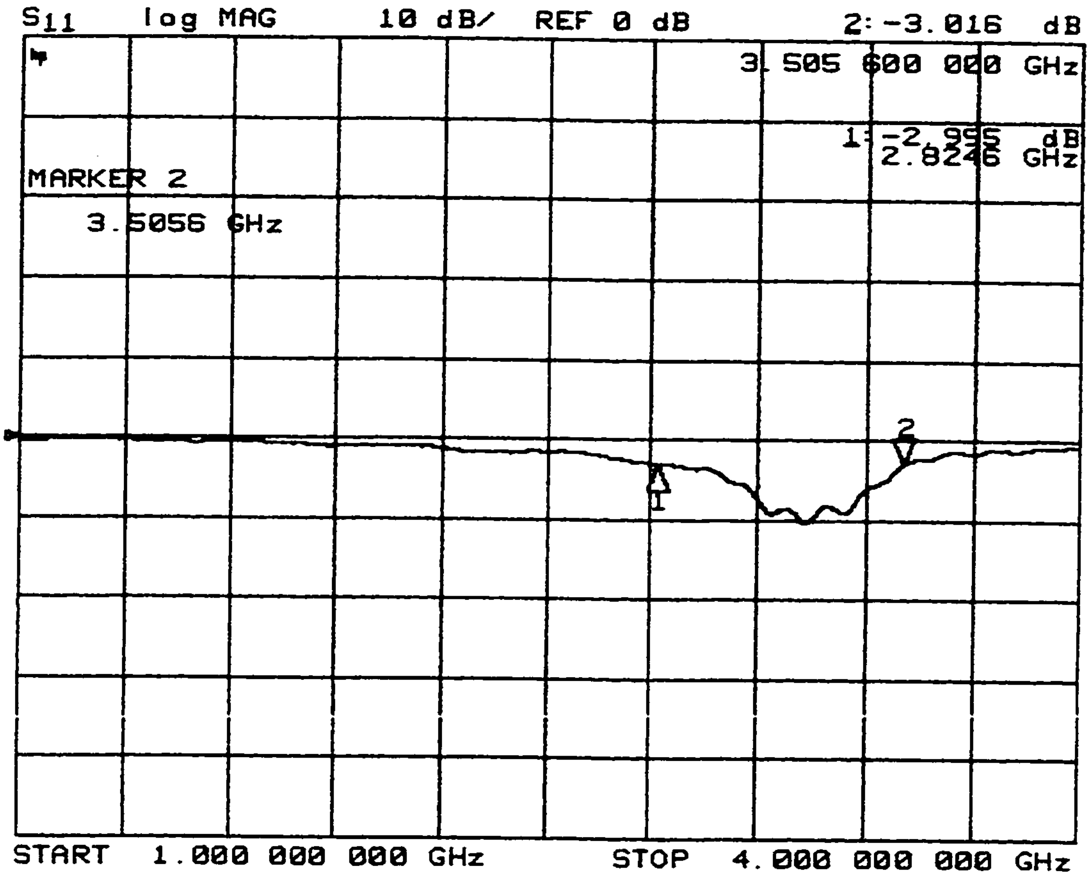

Figure 4.11 The corresponding measured return loss plot of Figure 4.10

In view of the above three cases: spacing = 0.1mm, spacing = 4mm and spacing = 6mm, *it can be concluded that by changing the spacing between the rectangular slot and the complimentary rectangular strip alone is not sufficient to construct a broadband antenna.* We should then try different shapes and sizes of the slot and the strip.

4.3 Computer Simulation

Instead of using the method of "Trial and Error" to build a new Magnetic-Electric dipole of arbitrary shape and dimensions in laboratory, we should find some other way to determine, by theory or by computer simulation, the characteristics of the antenna in advance. This approach permits an antenna engineer to construct a new antenna physically only after he is satisfied with the predicted or theoretical electrical characteristics of the proposed antenna. Of course, physically fine tuning the antenna may be necessary since the theoretical prediction method may not be in exact agreement with the real case. By using the above approach, we can save time, resources, and most importantly, we can understand the working mechanism of the proposed antenna. There are many methods to calculate the input impedance of an antenna. In this section, an integral equation with a numerical technique solution, which is usually referred to as the Moment Method will be discussed. After that, a computer simulation software package, WIPL-D, which utilizes the Moment Method will be introduced.

4.3.1 Pocklington's Integral Equation and Hallén's Integral Equation

Before discussing the Integral Equation method and the Moment Method, let's introduce two classical electric field integral equations, namely Pocklington's integrodifferential equation and Hallén's integral equation. Only the final results of these two equations will be presented here; for the details of the derivation, one can refer to antenna textbooks or papers [4 ,5, 6]. Now refer to Figure 4.12, we obtain

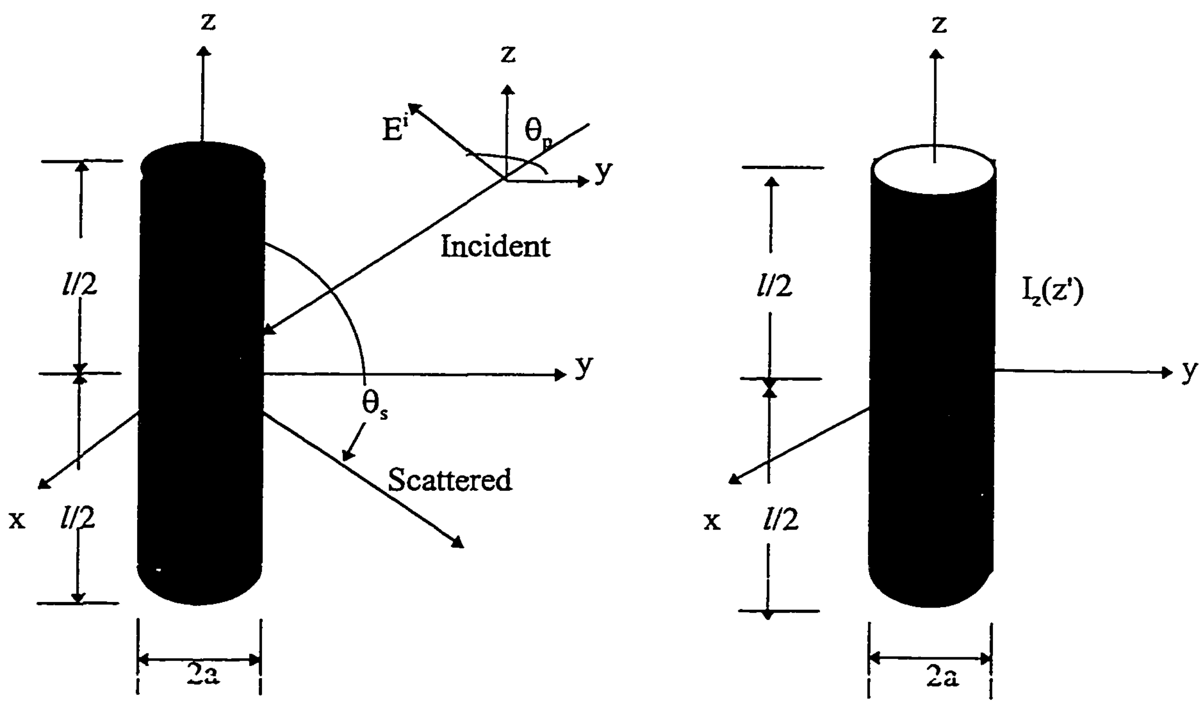

(a) Geometry (b) Equivalent current

Figure 4.12 Uniform plane wave obliquely incident on a conducting wire.

Pocklington's integrodifferential equation:

$$\int_{-l/2}^{+l/2} I_z(z') \left[\left(\frac{\partial^2}{\partial z^2} + k^2 \right) G(z,z') \right] dz' = -j\omega\varepsilon E_z^i(\rho = a) \tag{4-1}$$

and Hallén's integral equation:

$$\int_{-l/2}^{+l/2} I_z(z') \frac{e^{-jkR}}{4\pi R} dz' = -j\sqrt{\frac{\varepsilon}{\mu}} [B_1 \cos(kz) + C_1 \sin(k|z|)] \tag{4-2}$$

In equations(4-1) and (4-2), $I_z(z')$ represents the equivalent filamentary line-source current located on the surface of the wire, as shown in Figure 4.12 (b), and

$$G(z, z') = \frac{1}{2\pi}\int_0^{2\pi} \frac{e^{-jkR}}{4\pi R} d\phi' \tag{4-3}$$

R is the distance from any point on the source to the observation point.

$k = 2\pi/\lambda$ is the wave number;

B_1 is a constant and $C_1 = V_i/2$ where V_i is the applied voltage at the input terminals of the wire.

4.3.2 Moment Method.

Pocklington's integrodifferential Equation (4-1) and Hallén's integral Equation (4-2) each has the form of [4]

$$F(g) = h \tag{4-4}$$

where F is a known linear operator, g is the response function, and h is a known excitation function. F is an integrodifferential operator in equation (4-1) and an integral operator in equation (4-2). Our goal is to determine g if F and h are known.

According to the Moment Method, the unknown response function g has to be expanded as a linear combination of N terms such that [4]

$$g(z') \approx a_1 g_1(z') + a_2 g_2(z') + \ldots + a_N g_N(z') = \sum_{n=1}^{N} a_n g_n(z') \tag{4-5}$$

In (4-5), each a_n is an unknown constant and each $g_n(z')$ is a known function referred to as a basis or expansion function. Substituting (4-5) into (4-4), and since F is a linear operator, one can get

$$\sum_{n=1}^{N} a_n F(g_n) = h \tag{4-6}$$

Since there are N unknowns but only one equation, it is necessary to evaluate equation (4-6) at N different points to yield N linearly independent equations. As a result, one can get

$$\sum_{n=1}^{N} a_n F(g_n) = h_m, m = 1,2,\ldots,N \tag{4-7}$$

Equation (4-7) is more conveniently expressed as a matrix form,

$$[Z_{mn}][I_n] = [V_m] \tag{4-8}$$

where

$$Z_{mn} = F(g_n)$$

$$I_n = a_n$$

$$V_m = h_m$$

Therefore, the unknown coefficients a_n can be solved by

$$[I_n] = [Z_{mn}]^{-1}[V_m] \tag{4-9}$$

The above approach to find $[I_n]$ numerically is known as the Moment Method.

Once the current distribution is found and the applied voltage is specified, we can determine the input impedance by

$$Z_{in} = \frac{V_{in}}{I_{in}} \tag{4-10}$$

The basis or expansion function $g_n(z')$ can be one of the many possible kinds, Figure 4.13 shows some of the practical basis functions.

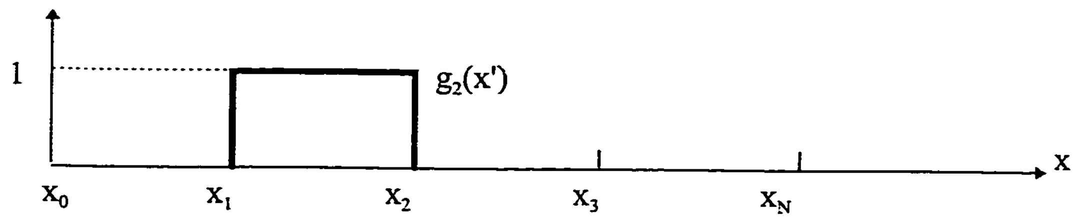

(a) Piecewise constant subdomain function.

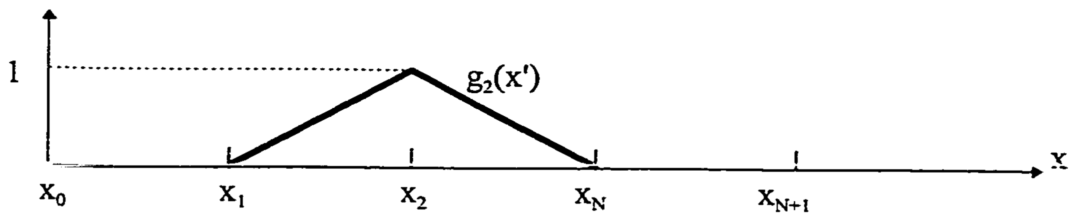

(b) Piecewise linear subdomain function.

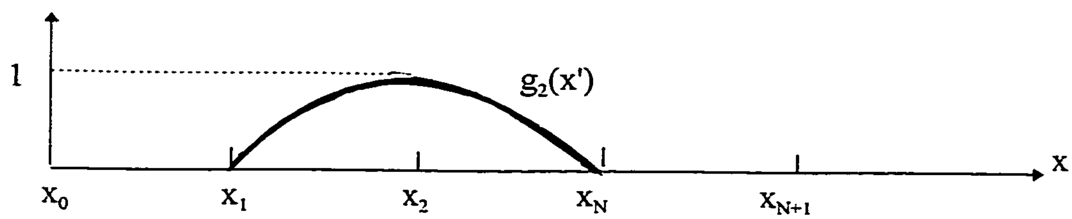

(c) Piecewise sinusoids subdomain function.

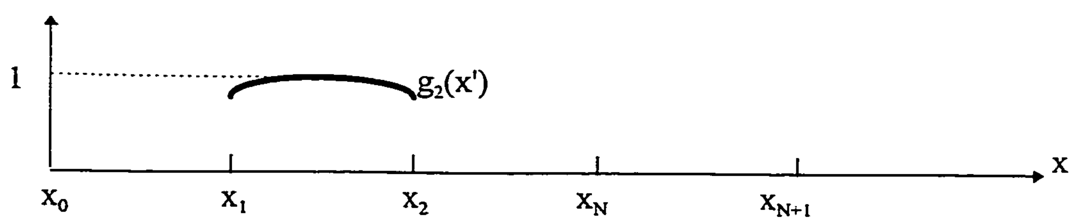

(d) Truncated cosines subdomain function.

Figure 4.13 Some practical basis functions.

As a guideline, one should choose a basis function [4] which has the ability to accurately represent and resemble the anticipated unknown function, while minimizing the computational effort required to employ it.

4.4 WIPL-D

WIPL-D is an user friendly computer software package for electromagnetic modeling of composite metallic and dielectric structures. It employs the Moment Method described in section 4.3.2 to solve for the unknown current distributions on the proposed composite metallic and dielectric structure [7]. Once these current distributions are known, all other quantities of interest such as input impedance, near field and far field, can be easily obtained.

The version we used to simulate the various proposed antenna structures was WIPL-D V1.0, where the maximum number of unknowns (i.e. N in section 4.3.2) can be handled is 2000 which is more than enough for our proposed antenna structures. Therefore, the simulated results were expected to be quite accurate.

To simulate an antenna in WIPL-D, we should first specify all the coordinates of the constituent nodes in the rectangular coordinate system. For a plate of any shape, the nodes are the corners of that plate. For a metallic wire, the nodes are just the two end points. With all the nodes specified, we can then use plates and wires to build an antenna. After this, we have to specify the type of excitation used and the frequency range of interest.

With all the configurations set up properly, we can run the program and the simulated results can either be displayed on the screen or printed out.

Figure 4.14 shows the WIPL-D simulated return loss plot (S11 plot) of the antenna in Figure 4.3, where the spacing between the rectangular slot and the rectangular strip is 4mm.

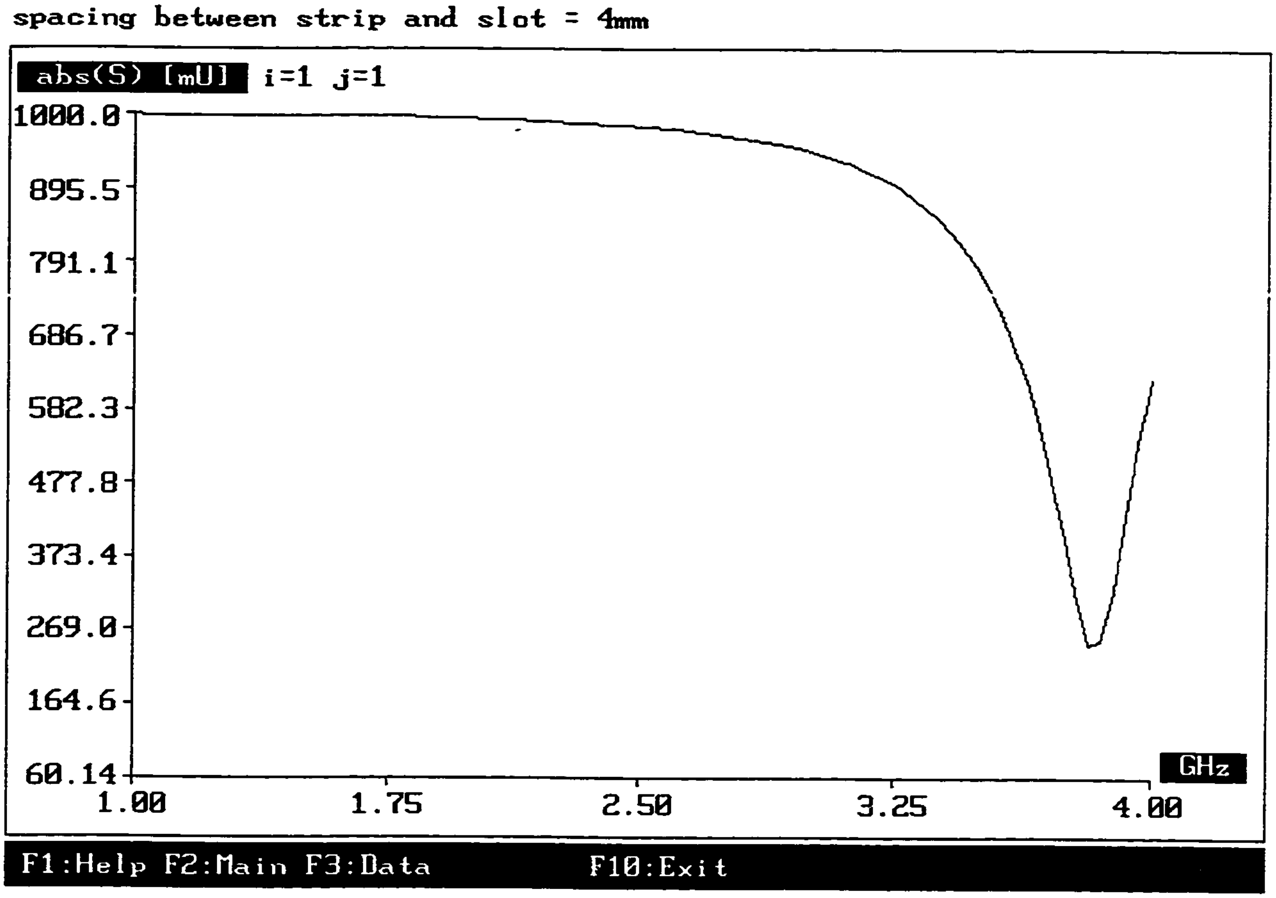

Figure 4.14 WIPL-D simulated return loss of the antenna in Figure 4.3, where the spacing between the slot and the strip is 4mm

Comparing to the actual measurement on the same antenna which is shown in Figure 4.11, the two results are roughly the same except that the simulated result is about 0.7GHz shifted to the right. Note that both the simulation and the actual measurement show that the best match is about a 10dB return loss.

4.5 Development of the Ultra broadband Magnetic-Electric Dipole Antenna

Since the rectangular slot and rectangular strip could not fulfill the broadband requirement, we should seek for other shapes. It is well-known that the "bow-tie" antenna shown in Figure 4.15 is a broadband antenna [8, 9]; so we should then try to couple a "bow-tie slot" (or bow-tie magnetic dipole antenna) and

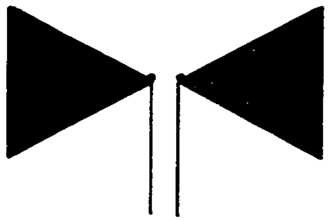

Figure 4.15 Bow-tie Electric dipole antenna

a "bow-tie electric dipole antenna" together. Figure 4.16 (c) and (d) show the resulting Magnetic-Electric dipole antenna constructed from the "bow-tie" shape with all the dimensions. Figure 4.17 is the perspective view of the antenna.

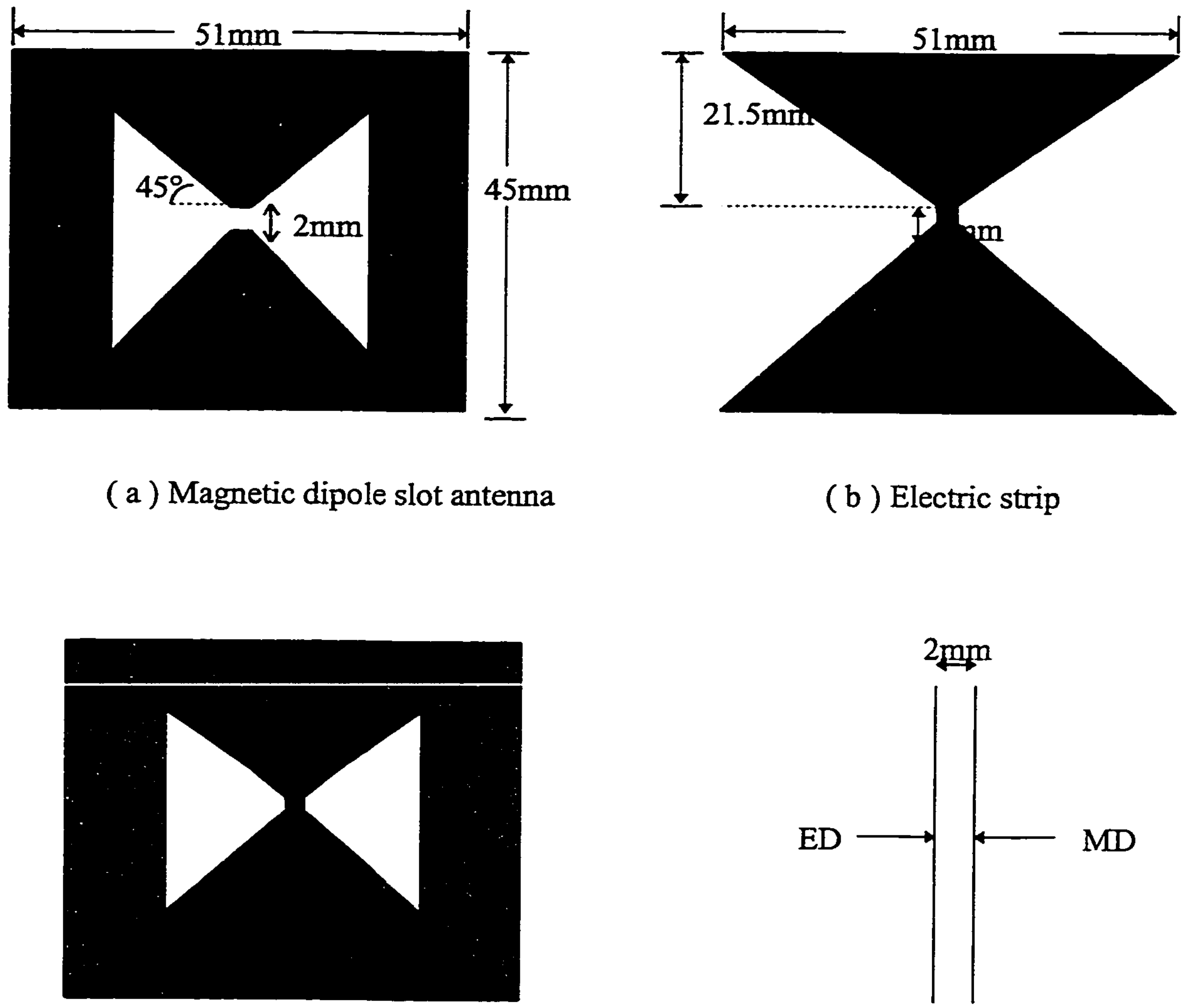

(a) Magnetic dipole slot antenna

(b) Electric strip

(c) Magnetic-Electric Dipole
(front view)

(d) Magnetic-Electric Dipole
(side view)

Figure 4.16 Magnetic-Electric Dipole Antenna made from "bow-tie" shape.

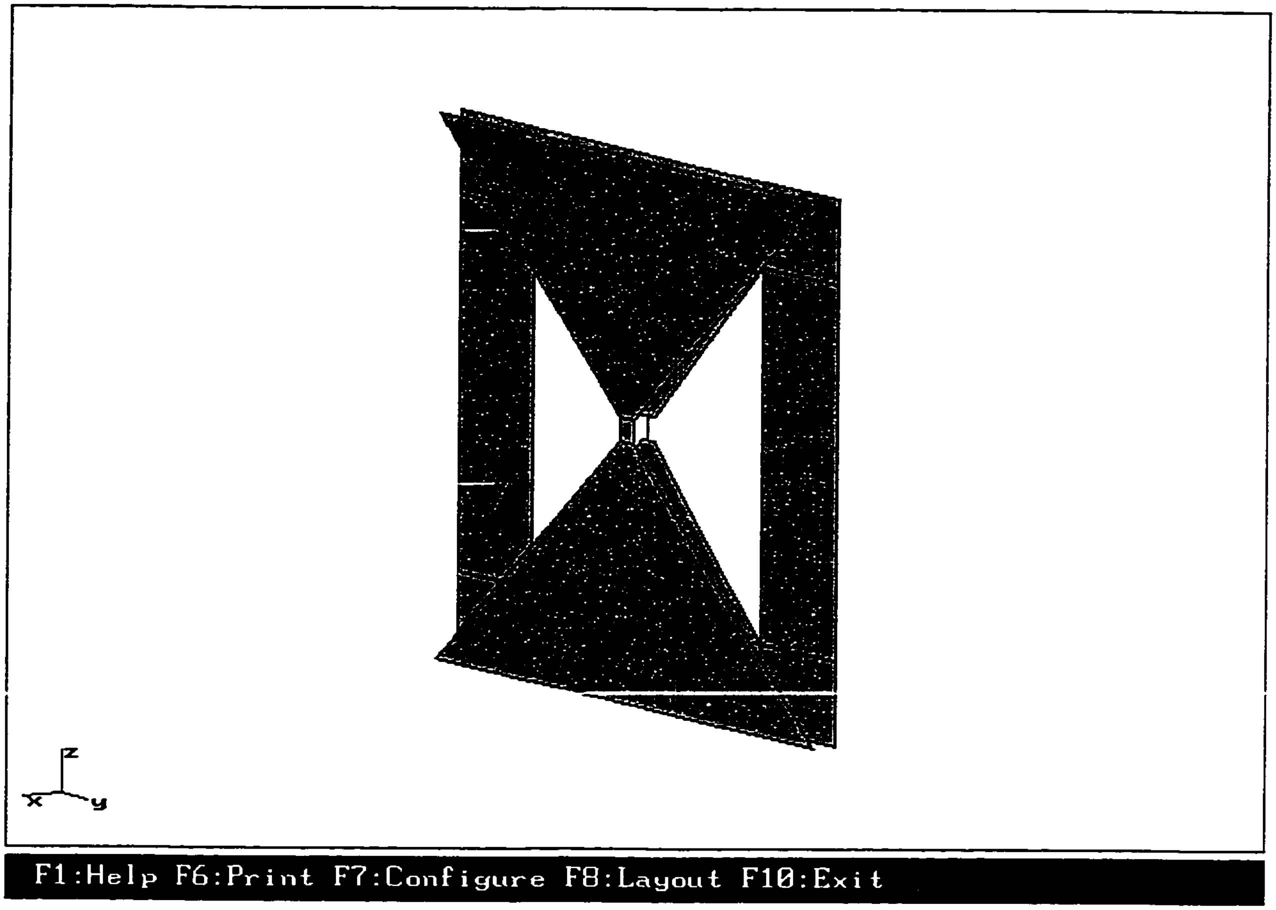

Figure 4.17 Perspective view of the "bow-tie" Magnetic-Electric Dipole

Note that the metallic strip is not the complimentary of the slot anymore, i.e. the strip and the slot are of different dimensions. However, the width and the length of the strip are the same as those of the metallic plane containing the slot. The reason for doing this is: *with the same maximum dimension, it is desirable to have the lowest possible matched frequency*. The maximum dimension is 51mm x 45mm even if the metallic strip was made smaller; however, the larger (longer and wider) the metallic strip, the lower the operating frequencies and the broader the bandwidth would be. Again, the magnetic slot was fed by a voltage source across the gap as in Figure 4.16 (a), and the electric strip acted as a parasitic element. The strip was oriented 90° relative to the slot as shown in Figure 4.17. Figure 4.18 shows the WIPL-D simulated input impedance of the antenna.

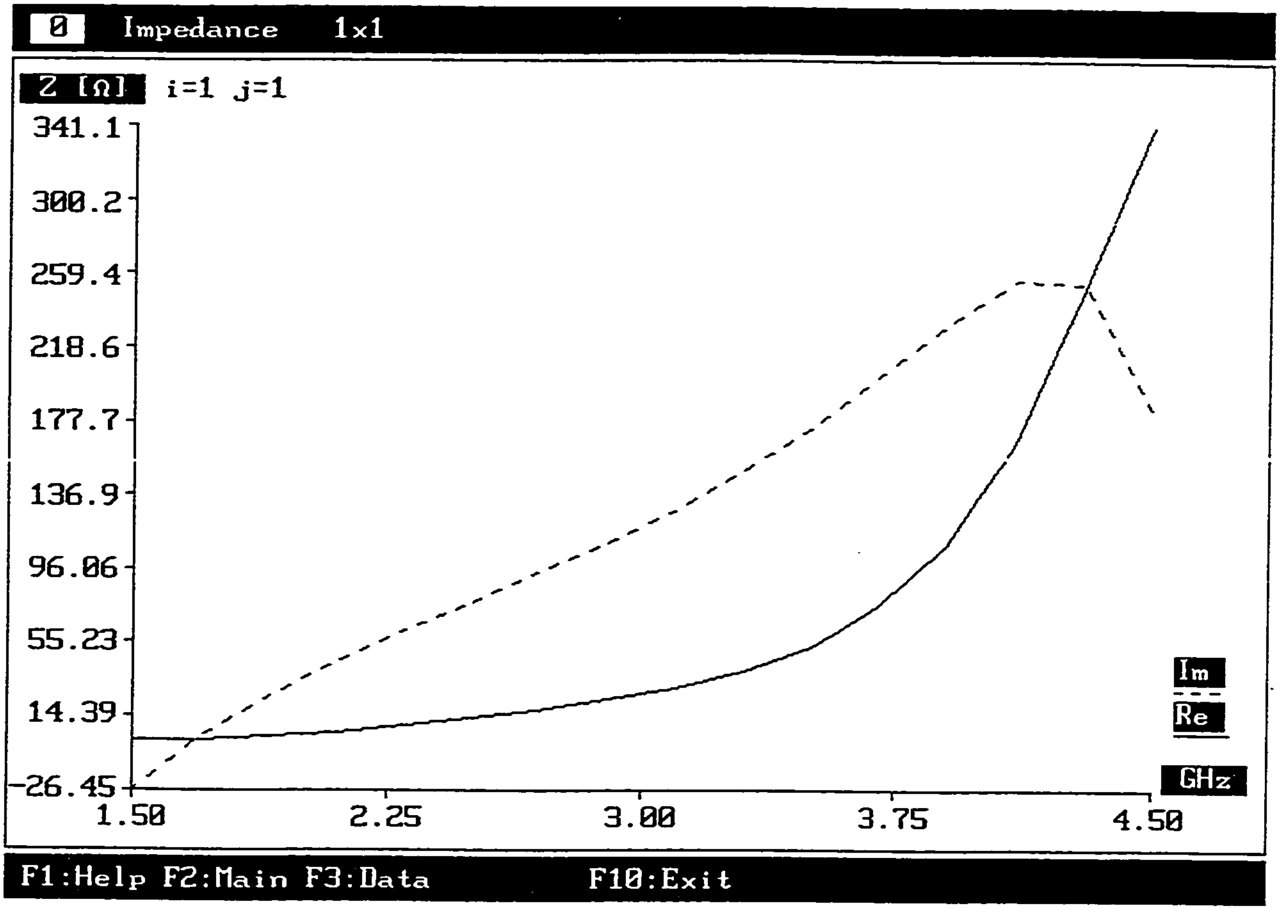

Figure 4.18 WIPL-D simulated input impedance of the antenna shown in Figure 4.17

Ideally, we want the resistive component to be fairly constant and the reactive component to be about zero for a wide range of frequency. The resistive component is quite constant, but small from1.5GHz to 3GHz, so inefficient radiation is expected. From 3GHz to

4.5GHz, the resistive component is too large; so it can be deduced that the matching is very poor from 1.5GHz to 4.5GHz. Figure 4.19 is the return loss plot which illustrates this. The best matching point (match to 50Ω) in this frequency range has a return loss of only 2dB loss which corresponds to 790mU.

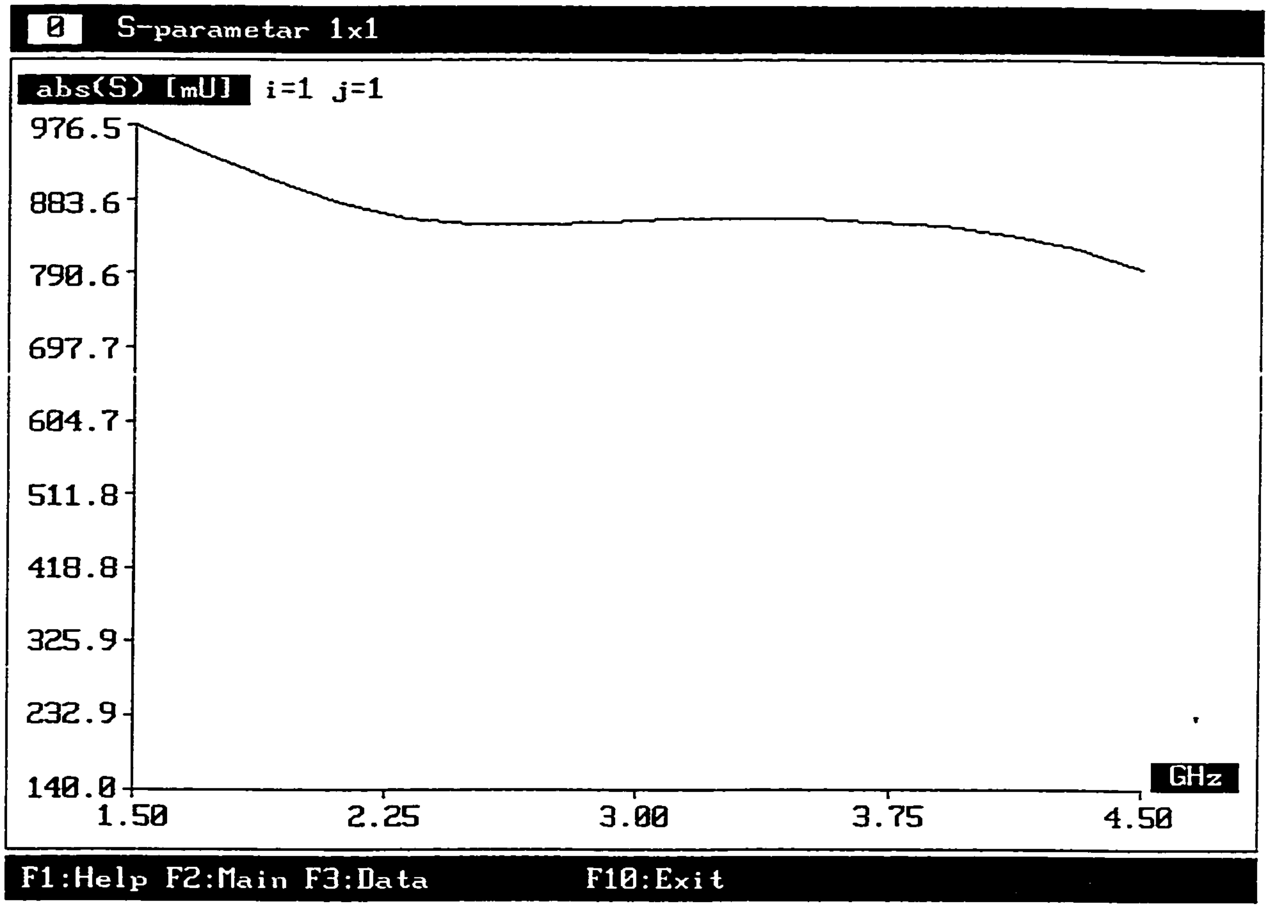

Figure 4.19 WIPL-D simulated return loss of the antenna shown in Figure 4.17

It seems that more control variables are needed in order to construct a broadband antenna. With the spacing between the slot and the strip , and all other dimensions fixed, the only variation this time was that the "bow-tie" strip was bent as shown in Figure 4.20.

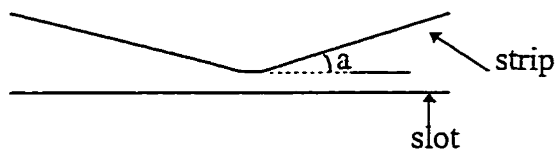

Figure 4.20 Illustration of the modification on the "bow-tie" Magnetic-Electric Dipole Antenna.

The WIPL-D simulated return loss plots for the bend angle a = 10°, 20°, 30°, 40° together with the 'flat' strip (a=0°) in the previous case is shown in Figure 4.21.

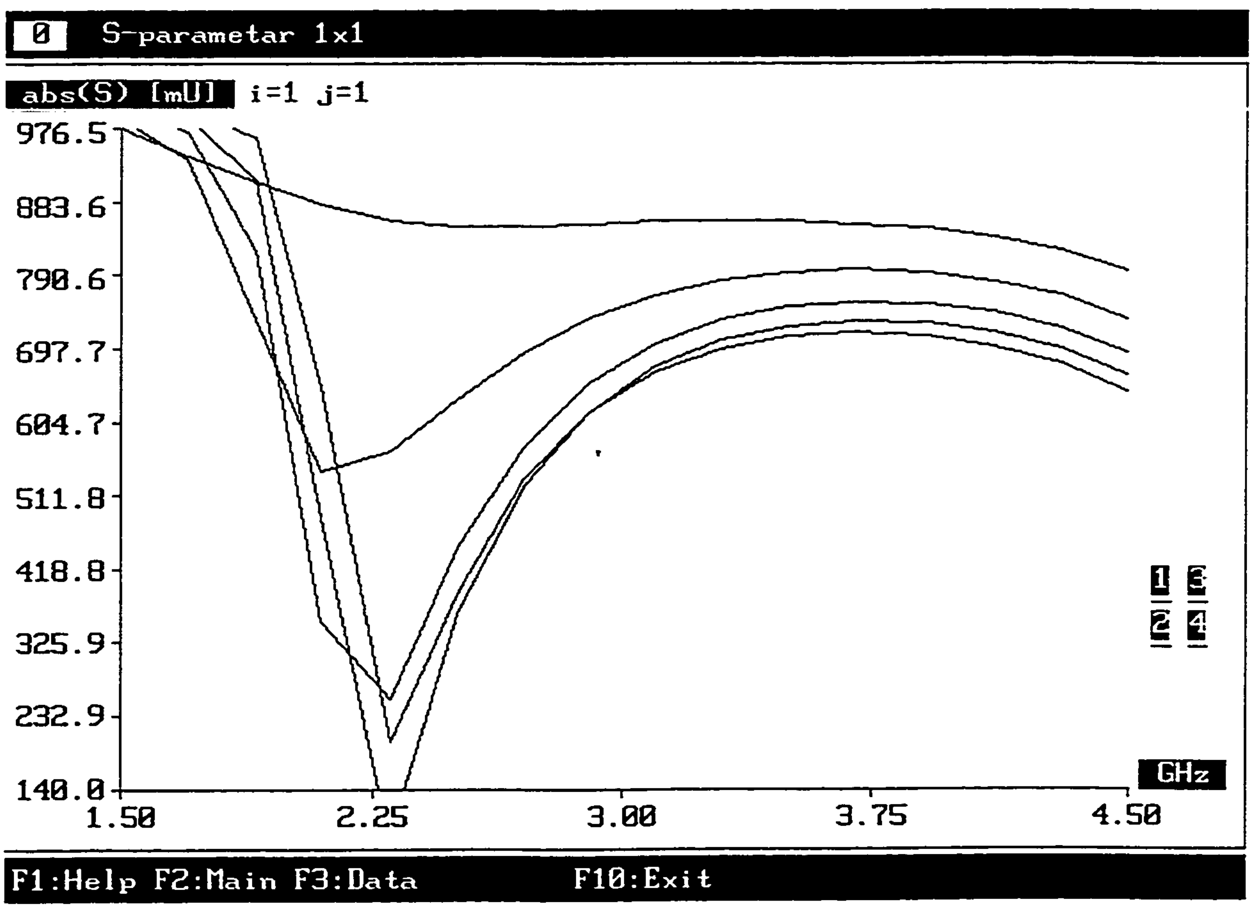

Figure 4.21 Return loss for various bend angles

The response becomes better and better as the bend angle "a" is increased from 0°, and becomes optimum when a=30°. Further increases of the bend angle "a" beyond 30° makes the response even worse.

Having learned from the WIPL-D simulation that a bend angle of 30° is the optimum angle, an actual antenna was built with the same dimensions as Figure 4.16 and a bend angle of 30°. The feeding cable was the same as Figure 4.3 (a) so that a potential difference was created across the gap. The material used was 0.254mm thick copper. Figure 4.22 shows the measured return loss of the antenna.

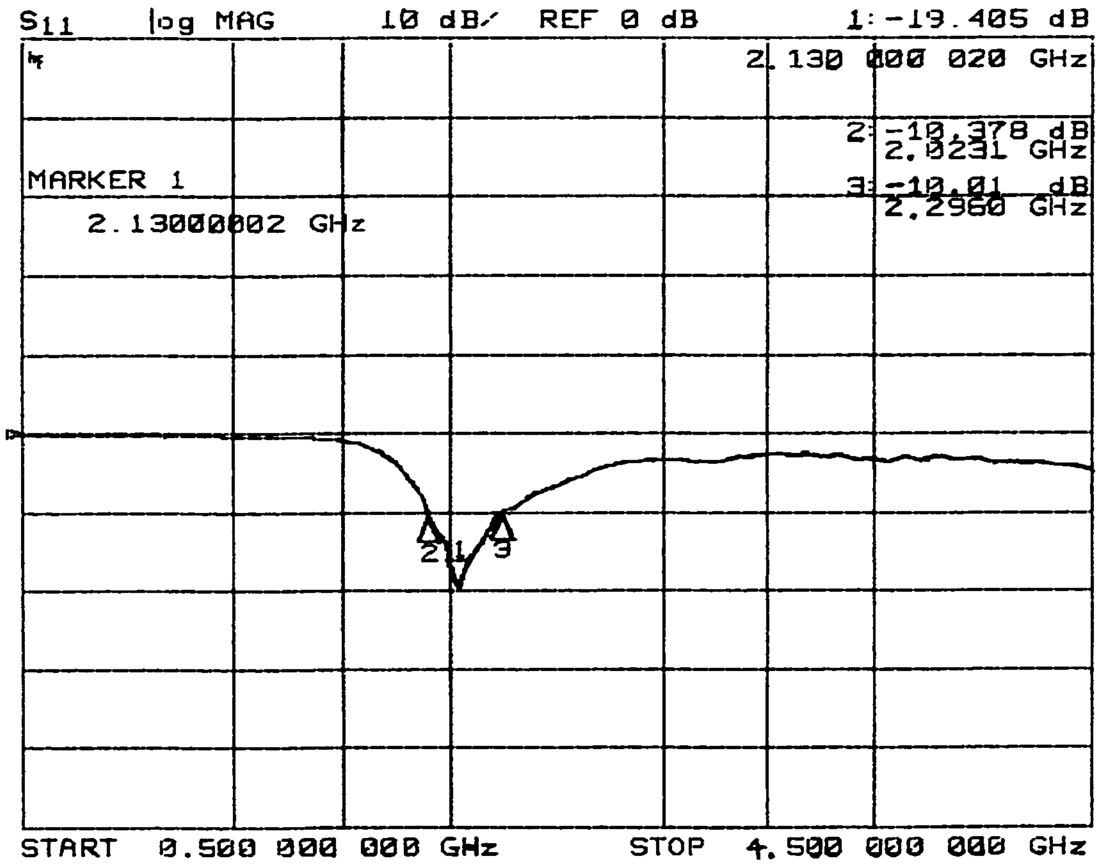

Figure 4.22 Measured return loss of the magnetic-electric dipole of Figure 4.20 for bend angle a = 30°

For clarity, the WIPL-D simulated return loss plot for bend angle a = 30° is repeated in Figure 4.23.

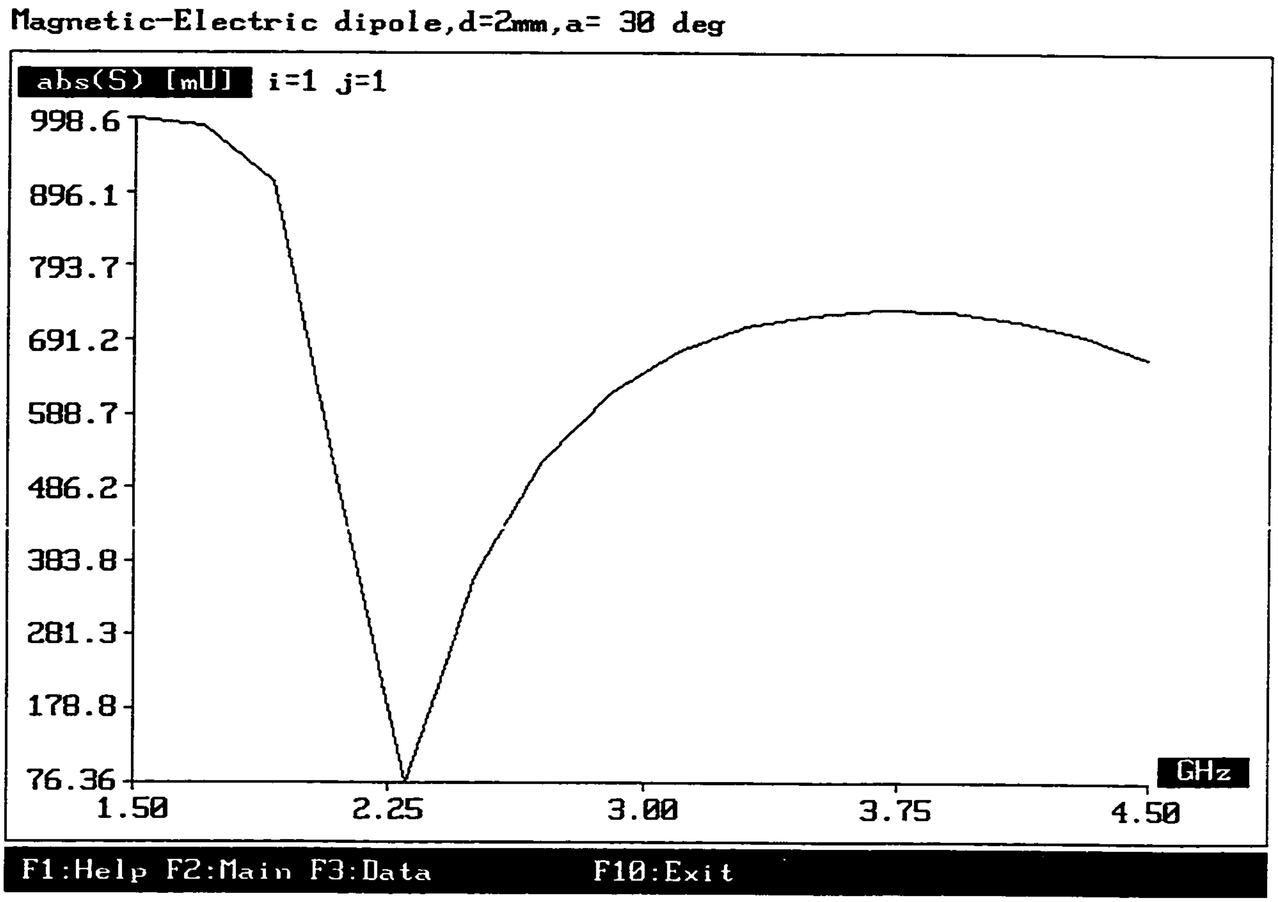

Figure 4.23 WIPL-D simulated return loss of the magnetic-electric dipole of Figure 4.20 for bend angle a = 30°

Both the actual measurement and the simulation reveal that the 10dB bandwidth of the antenna is about 275MHz, which is about 13% of the centre frequency. This is not a true broadband antenna and the bend of the "bow-tie" strip reduces the antenna compactness and robustness. In view of these, we tried to vary the relative dimension between the strip and the slot, and keep the strip flat (a = 0°). Figure 4.24 shows a new antenna where the length and the width of the "bow-tie" strip are about 3 times of those of the "bow-tie" slot. We named this antenna as MED1 (Magnetic-Electric Dipole 1).

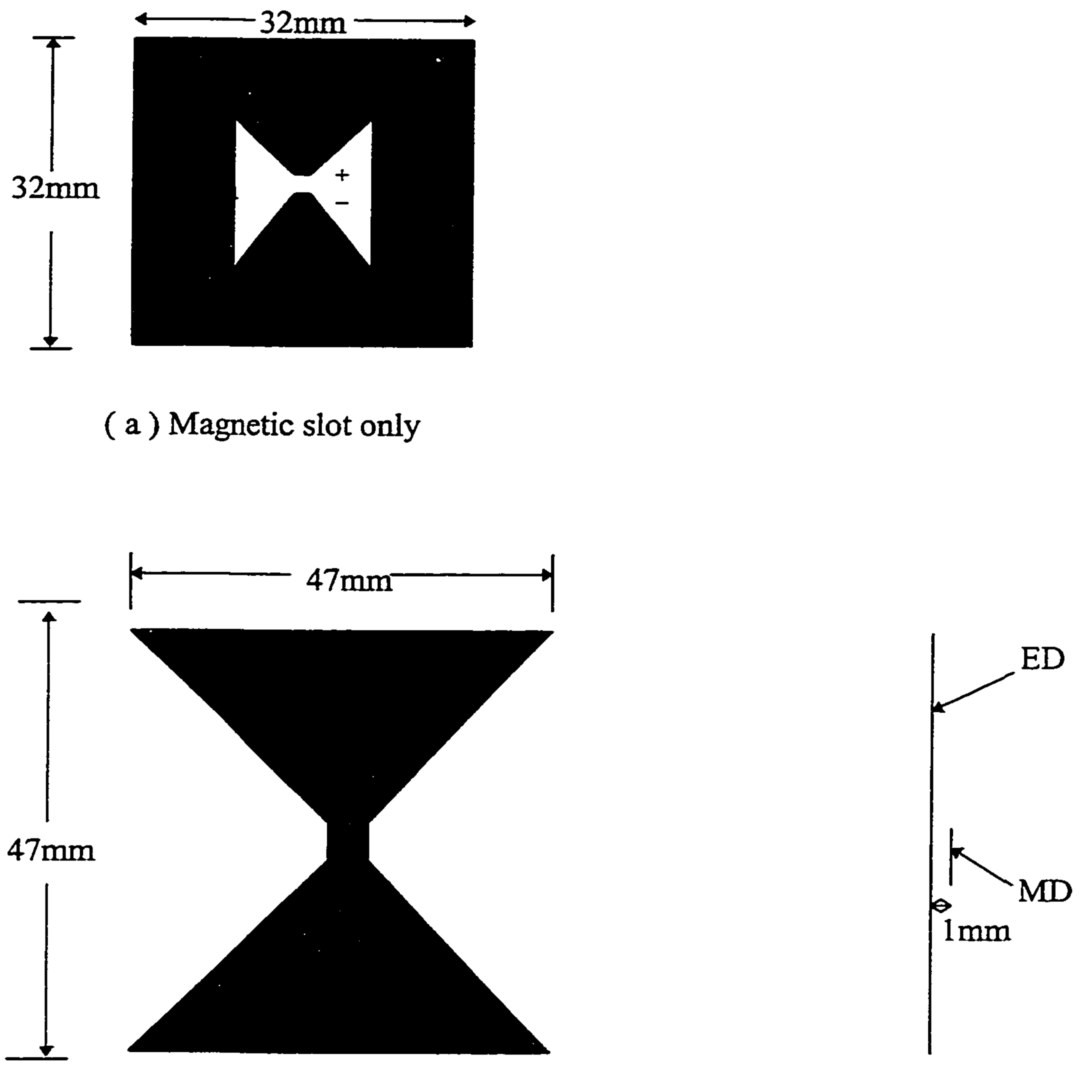

(a) Magnetic slot only

(b) Electric strip only

(c) MED1 (side view)

Figure 4.24 MED1, with dimensions.

Figure 4.25 is a perspective view of MED1. MED1 was simulated on WIPL-D.

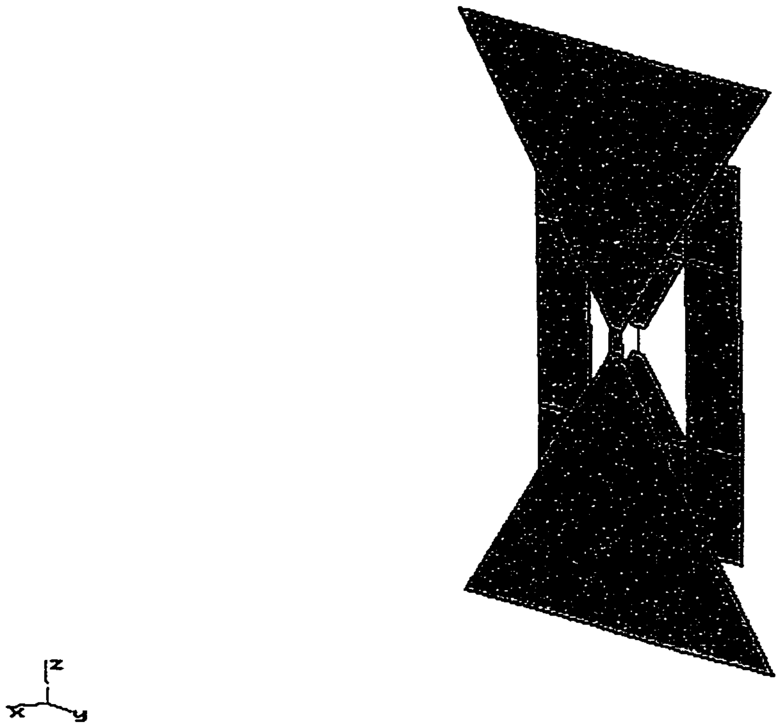

Figure 4.25 Perspective view of MED1

Figure 4.26 shows the simulated input impedance of MED1. Note that the input impedance was taken across the gap of the magnetic slot as shown in Figure 4.24 (a), but with the strip and the slot coupled together as in Figure 4.24 (c).

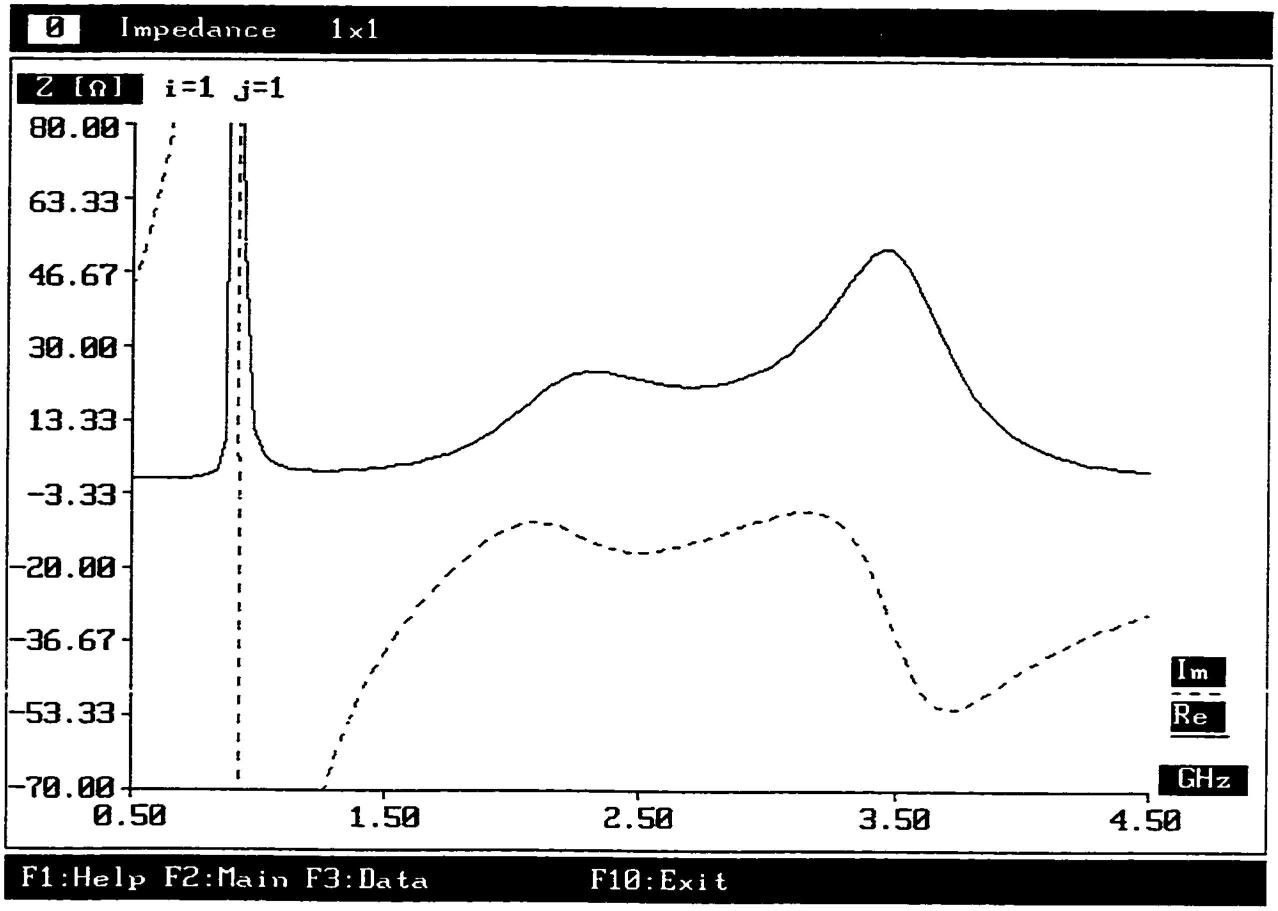

Figure 4.26 WIPL-D simulated input impedance of MED1

Referring to Figure 4.26, the resistive component is fairly constant and the reactive component is quite small from about 2GHz to 3GHz; therefore, it is expected that MED1 is a broadband antenna. Figure 4.27 shows the simulated return loss of MED1. According to the simulation, MED1 has a pretty good response from about 2GHz to 3.6GHz.

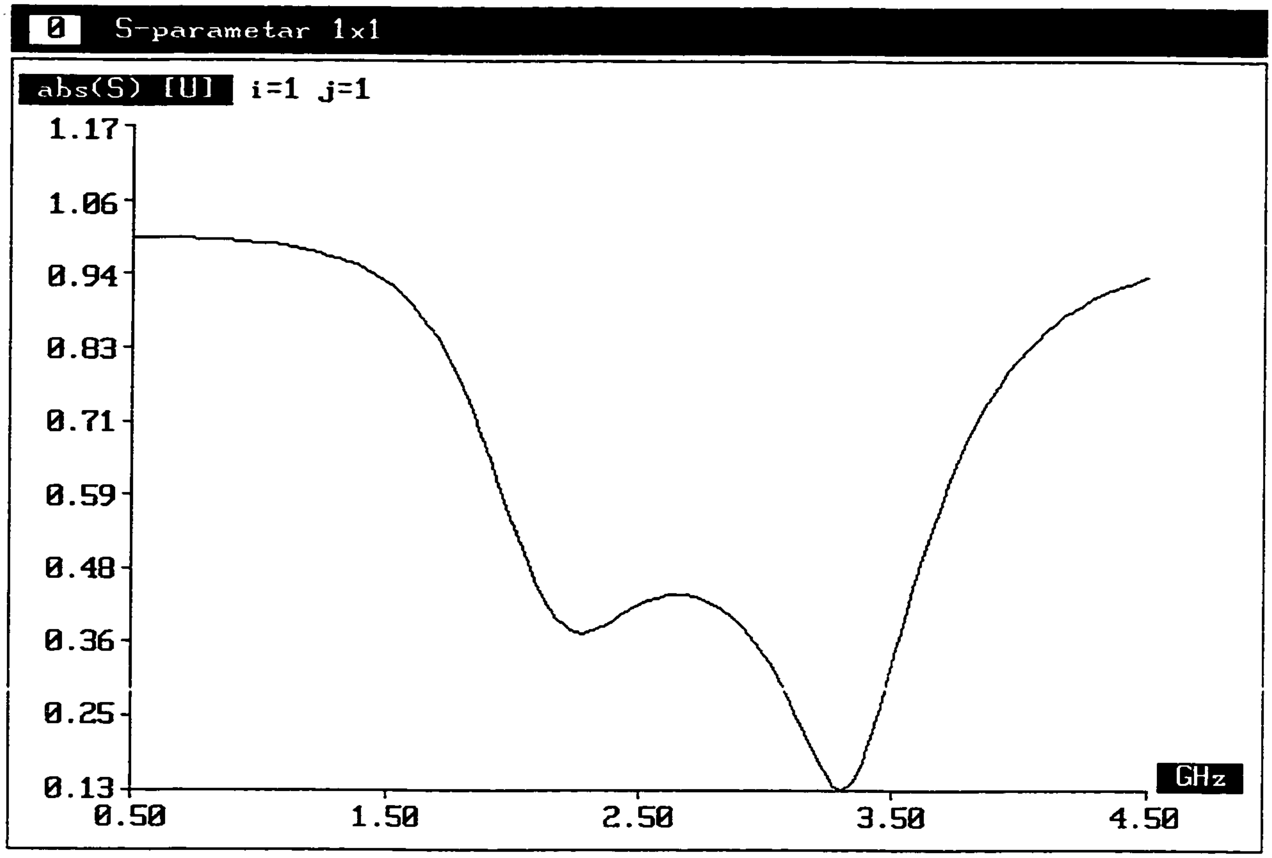

Figure 4.27 WIPL-D simulated return loss of MED1

We have learned from WIPL-D that by making the size of the metallic strip several times larger than that of the slot, the resulting Magnetic-Electric Dipole is quite broadband. Having this idea, we have built MED1 and other antenna MED2 on the bench. The experimental results such as input impedance, return loss, radiation pattern, and efficiency will be presented in Chapter 5. The constitute magnetic slot of MED2 is the same as that of MED1, i.e. a "bow-tie" slot; however, the electric strip and the gap spacing between the slot and the strip are different. Figure 4.28 show the details of MED2.

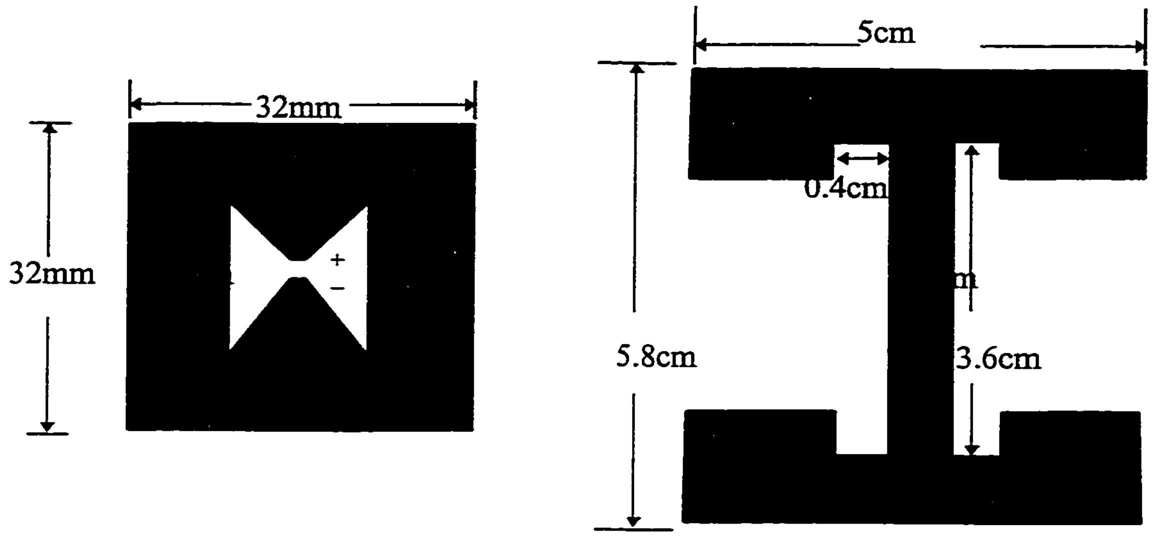

(a) Magnetic slot only

(b) Electric strip only

Figure 4.28 Constitute components of MED2

Figure 4.29 shows the perspective view of MED2.

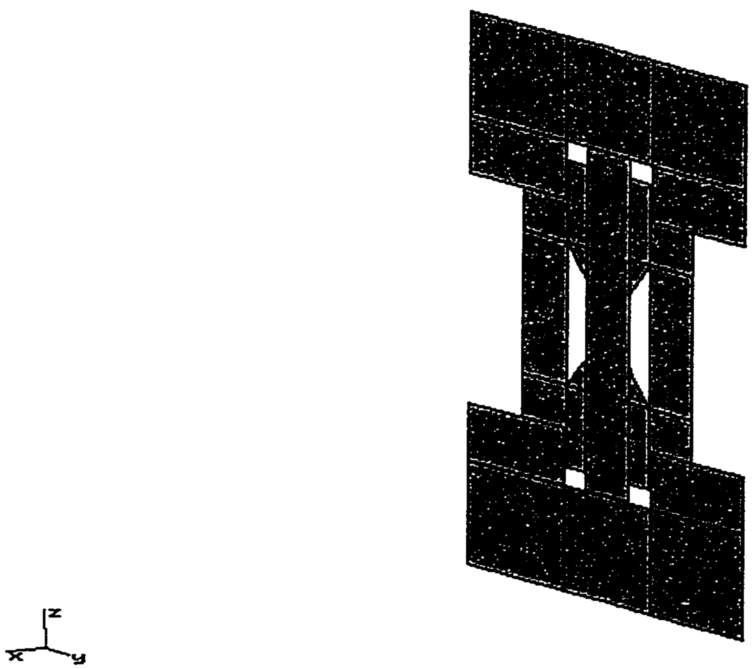

Figure 4.29 Perspective view of MED2

The purpose of the folded arms of the electric strip of MED2 are to act as a type of capacitive hat and reduce the frequency of the low frequency matching point.

Notes

[1] G. Kumar and K. C. Gupta, "Broad-Band microstrip antennas using additional resonators gap-coupled to the radiating edges," *IEEE Transactions on Antennas and Propagation*, vol. AP-32, no.12, Dec. 1984.

[2] P. S. Hall, "New wideband microstrip antenna using log-periodic technique," *Electronics Letters*, vol.16, no. 4, Feb. 1980.

[3] D. Sanchez-Hernandez and I. D. Robertson, "A survey of broadband microstrip patch antennas," *Microwave Journal*, Sept. 1996.

[4] C. A. Balanis, *Antenna Theory : Analysis and Design*, John Wiley & Sons, 1997, pp. 388-404.

[5] C. M. Bulter and D. R. Wilton, "Evaluation of potential integral at singularity of exact kernel in thin-wire calculations," *IEEE Transactions Antennas Propagation*, vol. AP-23, no. 2, March 1975, pp. 293-295.

[6] D. R. Wilton and C. M. Bulter, "Efficient numerical techniques for solving Pocklington's equation and their relationships to other methods," *IEEE Transactions Antennas Propagation*, vol. AP-24, no.1, Jan. 1976, pp. 83-86.

[7] B. M. Kolundzija, J. S. Ognjanovic, T. K. Sarkar, and R. F. Harrington, *WIPL-D V1.0 Operating Menu*, Artech House, 1997.

[8]] C. A. Balanis, *Antenna Theory : Analysis and Design*, John Wiley & Sons, 1997, pp. 447-449.

[9] R. E. Collin, *Antennas and Radiowave Propagation*, McGraw-Hill, 1985, p. 93.

Chapter 5: Experimental Results of MED1 and MED2

5.1 MED1 Measurement

Figure 5.1 gives the shape and the dimensional details of MED1 that was constructed for measuring the electrical performance of the antenna. All the dimensions in the real antenna are the same as those for simulation described in Chapter 4.

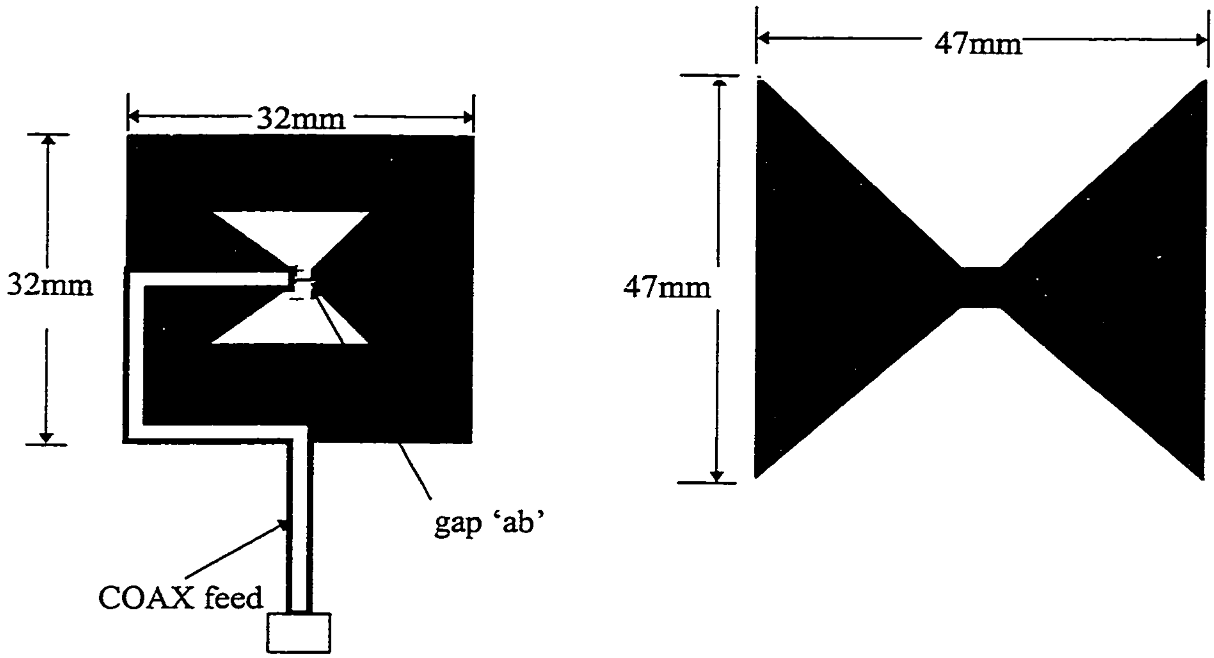

(a) Magnetic slot only (MD) (b) Electric strip only (ED)

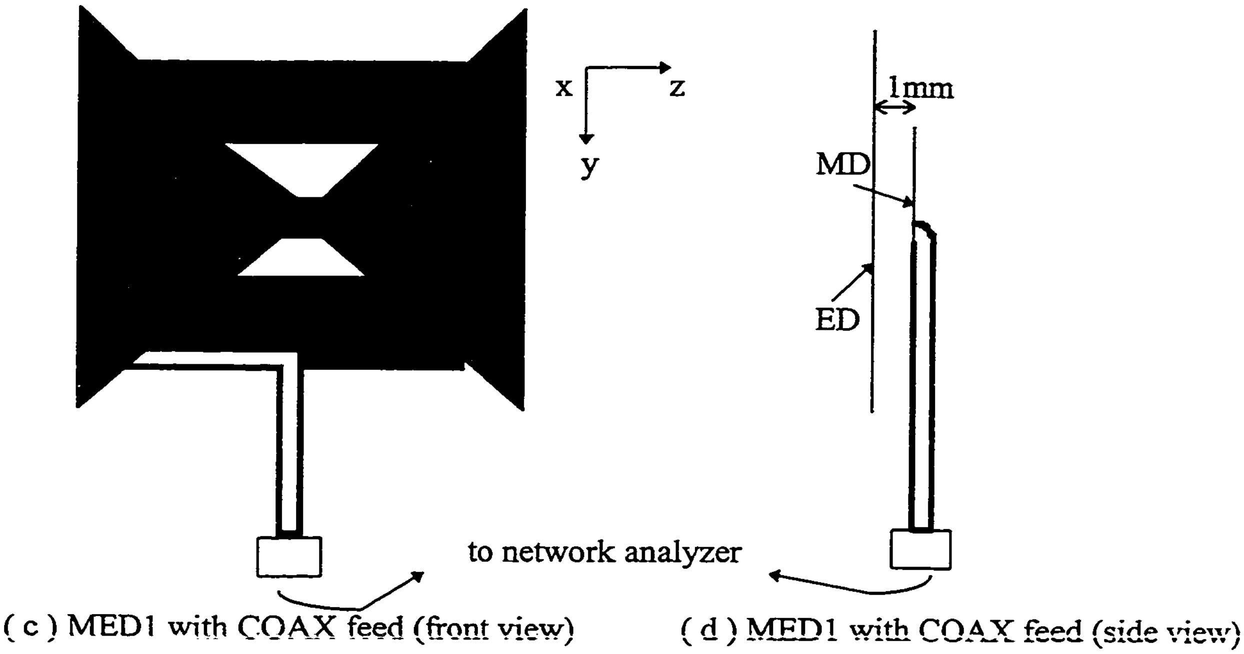

Figure 5.1 MED1 with COAX feed.

The antenna was built using copper of 0.254mm thickness. The coax feed used has a radius of 1mm. All the data were measured across the gap 'ab' on the magnetic dipole as shown in Figure 5.1 (a). The experimental setups and procedures were described in Chapter 3.

5.1.1 Input Impedance and Return Loss

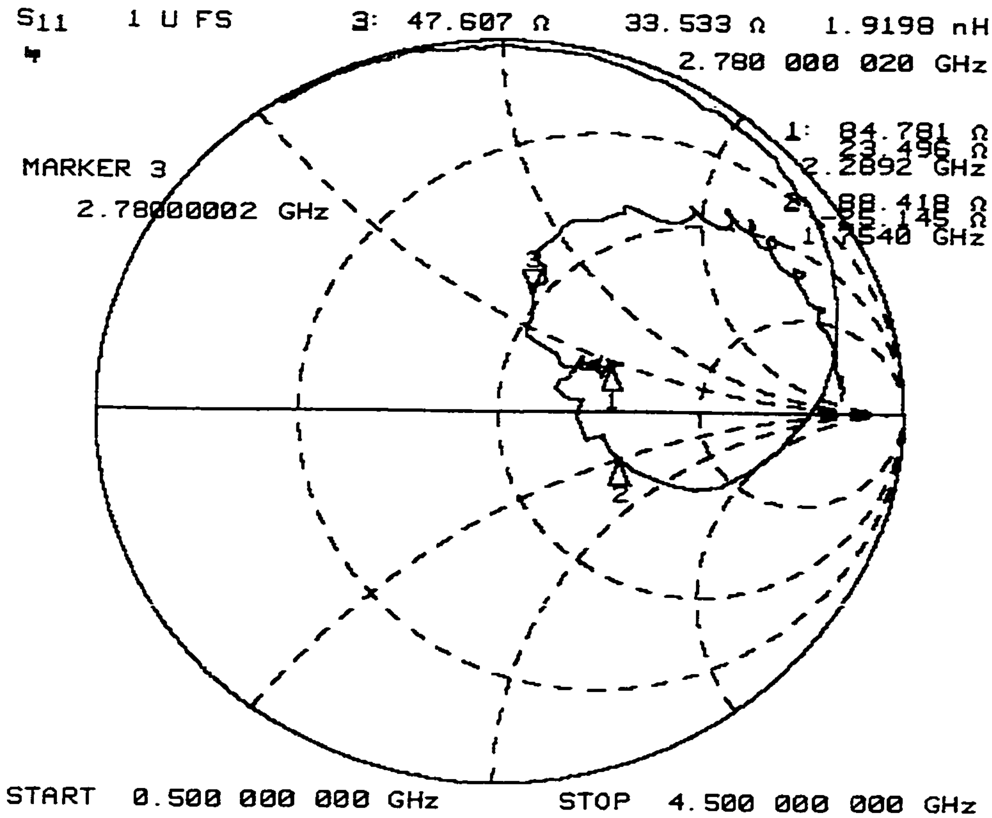

Figure 5.2 Measured input impedance of MED1

Figure 5.2 shows the input impedance of MED1 from 0.5GHz to 4.5GHz on a Smith Chart. The locus reveals a medium value (≈50Ω) of resistance and small value (<30Ω) of reactance for a wide range of frequency. For example, the input impedance are 88.4 - j25.1Ω at 1.75GHz (point 2), 84.8 + j23.5Ω at 2.29GHz (point 1), and 47.6 + j33.5Ω at 2.78GHz (point 3). Figure 5.3 shows the corresponding return loss of MED1.

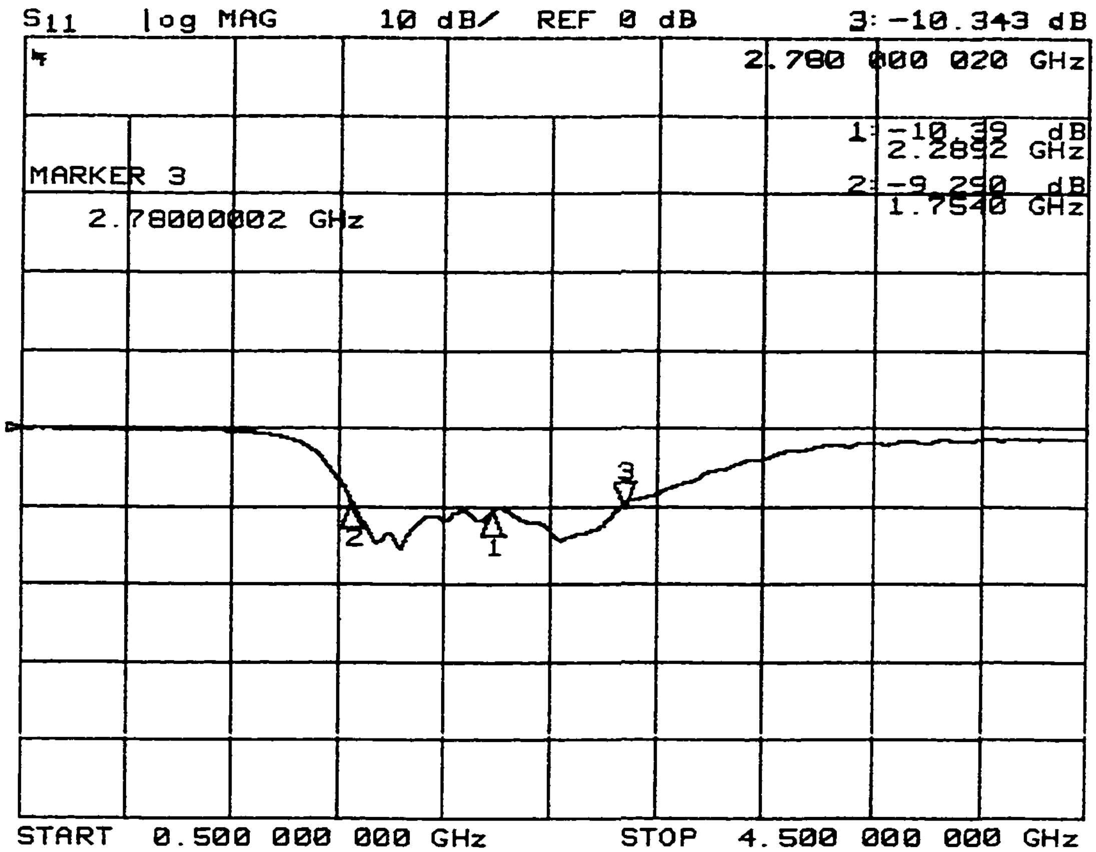

Figure 5.3 Measured return loss of MED1

The impedance bandwidth for voltage standing wave ratio (VSWR) < 2 is from 1.75 to 2.78GHz which corresponds to bandwidth ratio of 1:1.6. If point 1, which corresponds to 2.29GHz, is regarded as the center frequency; then the 10dB bandwidth is about 45% of the center frequency.

5.1.2 Radiation Pattern

The probe antenna used to measure the radiation patterns of MED1 was a horizontal dipole antenna of total length 83.3mm such that the resonant frequency is about 1.8GHz.

Figure 5.4 shows the experimental configuration inside the anechoic chamber. The setup outside the chamber, which is the same as shown in Figure 3.4, is not shown here.

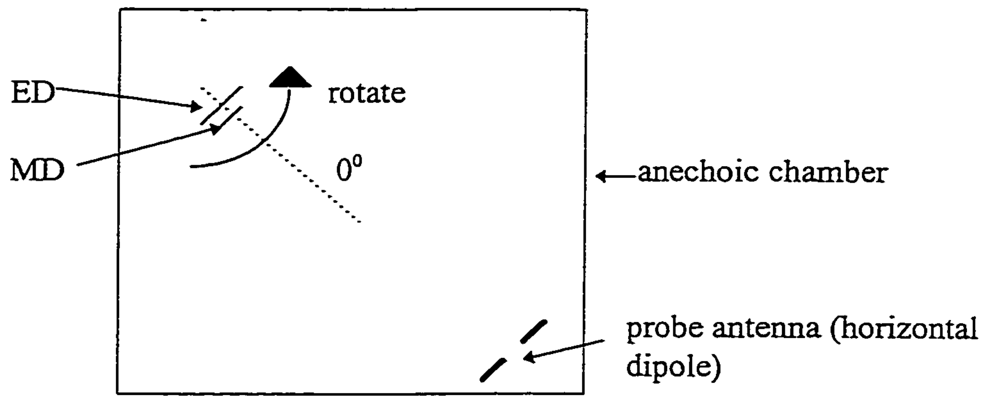

Figure 5.4 Experimental configuration inside the anechoic chamber to measure the radiation pattern of MED1 (top view)

The horizontal dipole was used to measure the far field of MED1 in the z direction (E_z) since it is the dominant field of MED1. Measuring E_z alone is sufficient to get the far field information of MED1. Figures 5.5 and 5.6 show the radiation patterns of MED1 on polar graphs at 1.8GHz and 2.8GHz respectively. The radiation pattern at 1.8GHz is very symmetric and as predicted. The maxima are oberved at 0° and 180° and the minima observed at 90° and 270°. At 2.8GHz, however, the pattern becomes nonsymmetric.

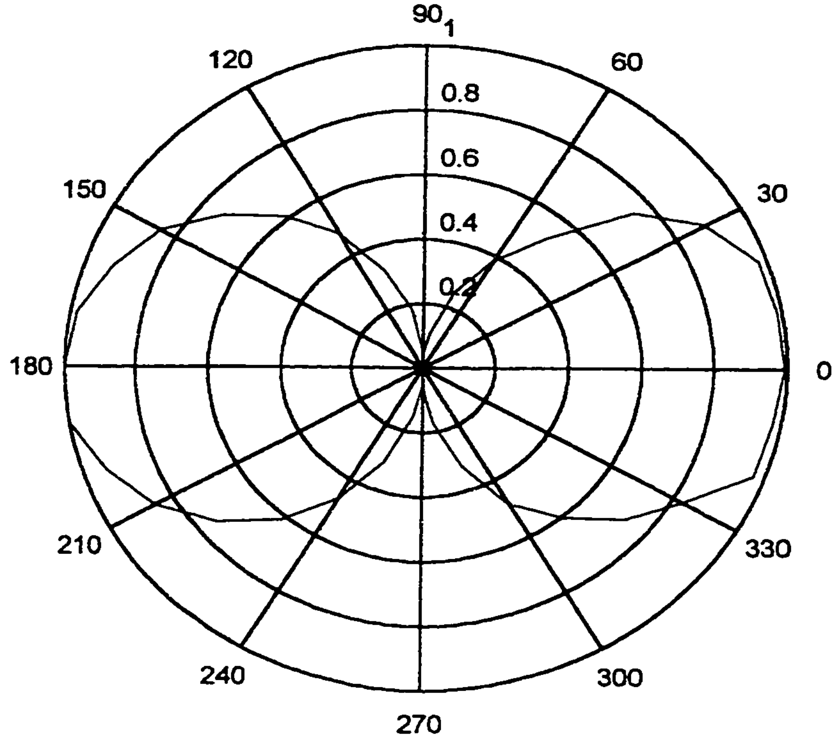

Figure 5.5 Radiation pattern of MED1 at 1.8GHz

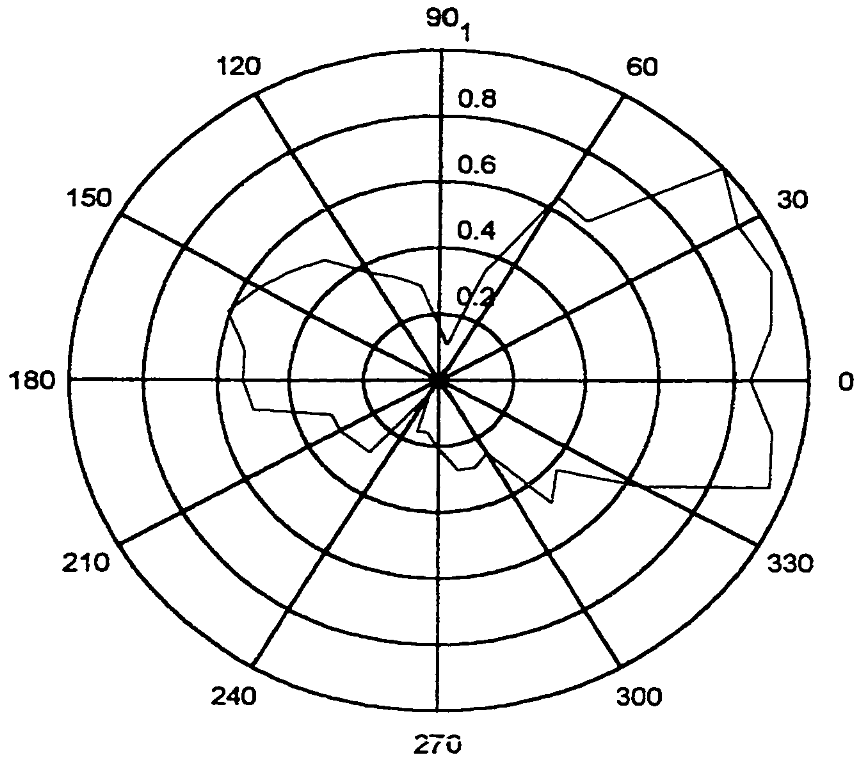

Figure 5.6 Radiation pattern of MED1 at 2.8GHz

5.1.3 Radiation Efficiency

Since the operating frequency range (assume 10dB return loss) of MED1 is from 1.8GHz to 2.8GHz and the operating frequency range of the waveguide used for antenna efficiency measurement is between 500MHz and 900MHz, it is then necessary to rescale the size of MED1 so that the operating range of it becomes coincident or close to the operating range of the waveguide. If we want to lower the bottom edge of the operating frequency range (1.8GHz) down to 700MHz, we will have to enlarge MED1 by a factor of 2.57. This makes the maximum length of MED1 12.1cm which is too large to fit in the waveguide since there is not enough clearance between the antenna and the walls of the waveguide. Nevertheless, due to similarities between MED1 and MED2, it is expected that the efficiency of these two antennas will be similar. As a guideline, we can refer to the efficiency measurement result of MED2 which will be presented in section 5.2.3.

5.2 MED2 Measurement

The exact dimensions of MED2 that was constructed for carrying the input impedance and radiation pattern measurements are shown in Figure 4.28 where its maximum length is 5.8cm. For efficiency measurements, however, the size of MED2 needed to be rescaled in order to lower the operating frequencies. We enlarged MED2 by a factor of 1.8. This makes the maximum dimension of MED2 equal to 10.44cm. The 10dB bandwidth of the MED2 after rescaling for efficiency measurement is between 750MHz and 2150MHz. The two versions of MED2 used to carry the experiments were built using copper of 0.254mm thickness. The feeding arrangement is the same as Figure 5.1 (a) and measurement signals were fed across the gap ‘ab’. The perspective view of MED2 is shown in Figure 4.29.

5.2.1 Input Impedance and Return Loss (performed on the original version of MED2)

Figure 5.7 shows the input impedance of MED2 from 0.5GHz to 4.5GHz on a Smith Chart.

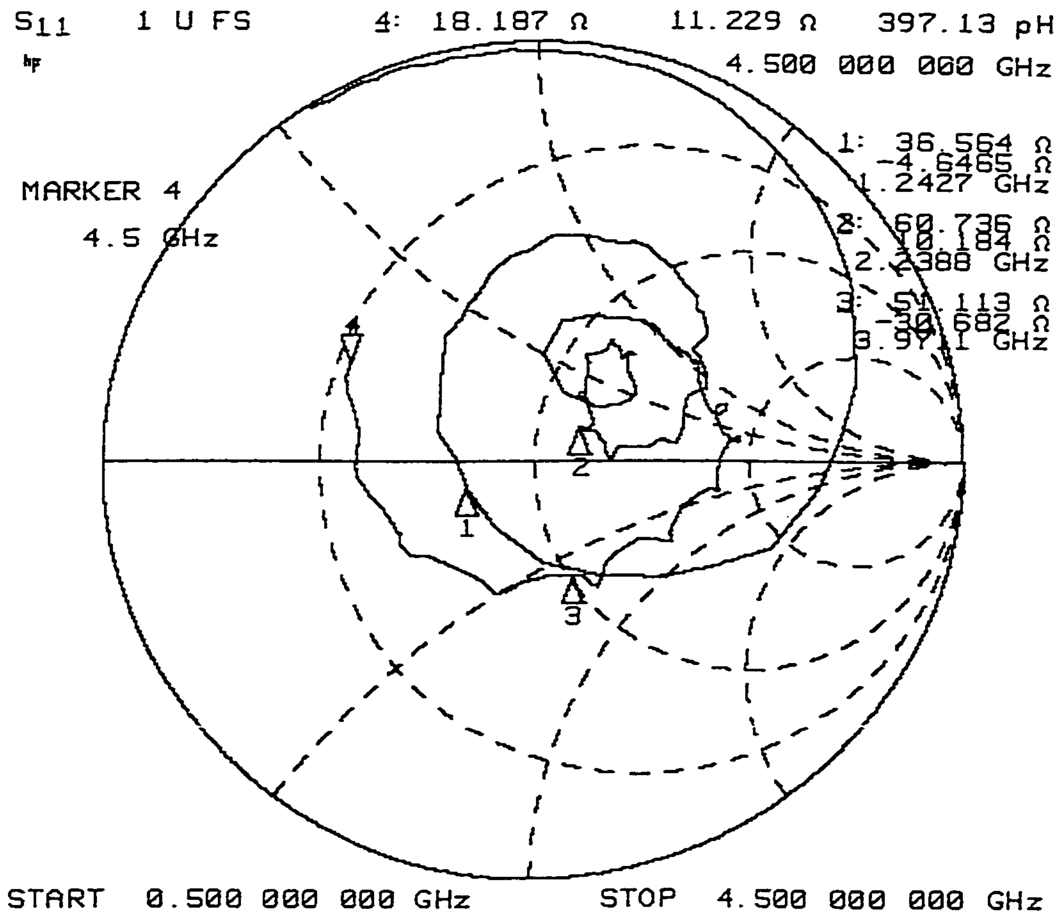

Figure 5.7 Measured input impedance of MED2

The locus loops around the center of the chart several times which implies there are multiple resonances in this frequency range. Figure 5.8 shows the corresponding return loss of MED2. MED2 is very wideband from 1.2GHz to 4.5GHz.

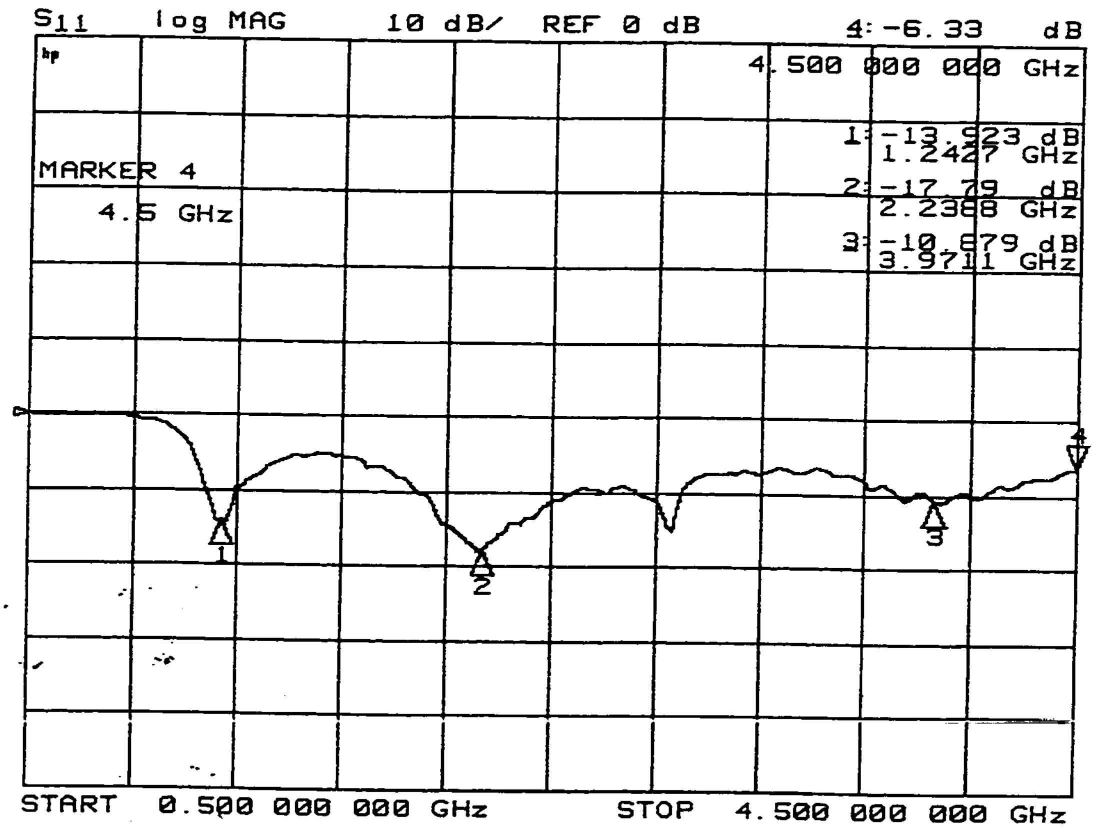

Figure 5.8 Measured return loss of MED2

5.2.2 Radiation Pattern (performed on the original version of MED2)

The measurement details are stated in section 5.1.2 and the experimental configuration is shown in Figure 5.4. Figures 5.9 and 5.10 show the radiation patterns of MED2 on polar graphs at 1.8GHz and 4.0GHz respectively. The radiation pattern at 1.8GHz is very symmetric. The maxima are observed at 0° and 180° and the minima at 90° and 270°. Like MED1, the radiation pattern become nonsymmetrical at the higher operating frequency.

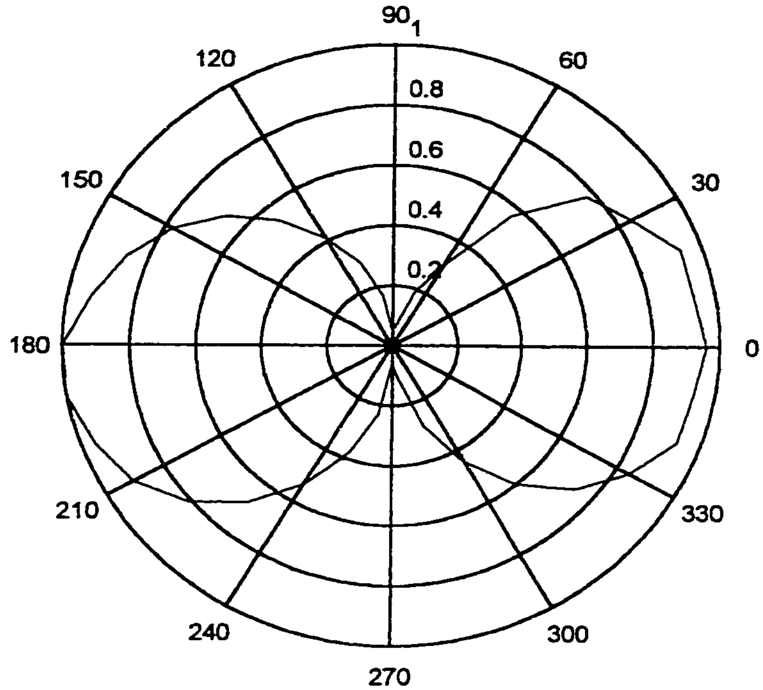

Figure 5.9 Radiation pattern of MED2 at 1.8GHz

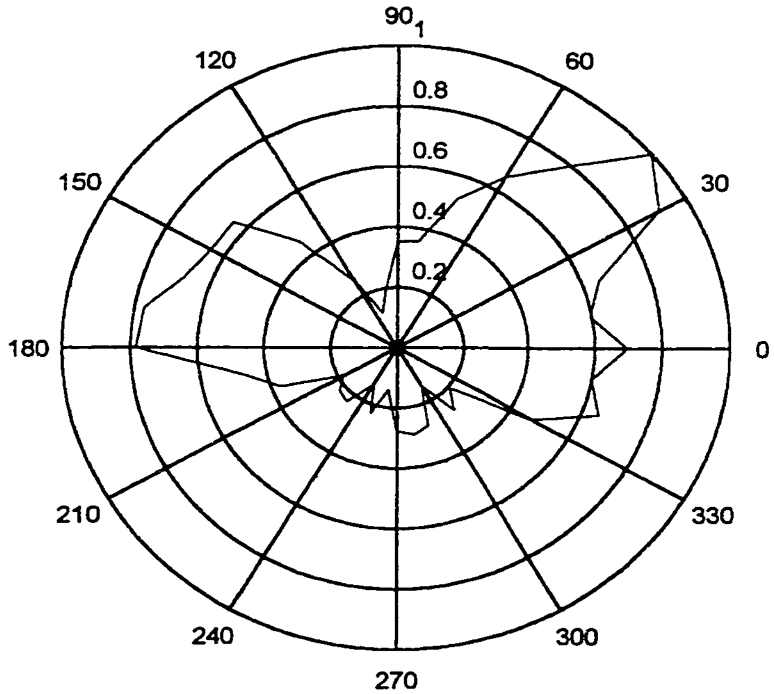

Figure 5.10 Radiation pattern of MED2 at 4GHz

5.2.3 Radiation Efficiency (performed on the enlarged version of MED2)

Antenna efficiency measurements are performed as discussed in Section 3.4. The antenna was enlarged by a factor of 1.8 to lower the operating frequencies for efficiency measurements. MED2 (and MED1) have a large surface area over which the current flows and should therefore be expected to have a low conduction loss. There should not be any dielectric losses or surface wave losses. The efficiency as a function of frequency from 500MHz to 900MHz is plotted in Figure 5.11.

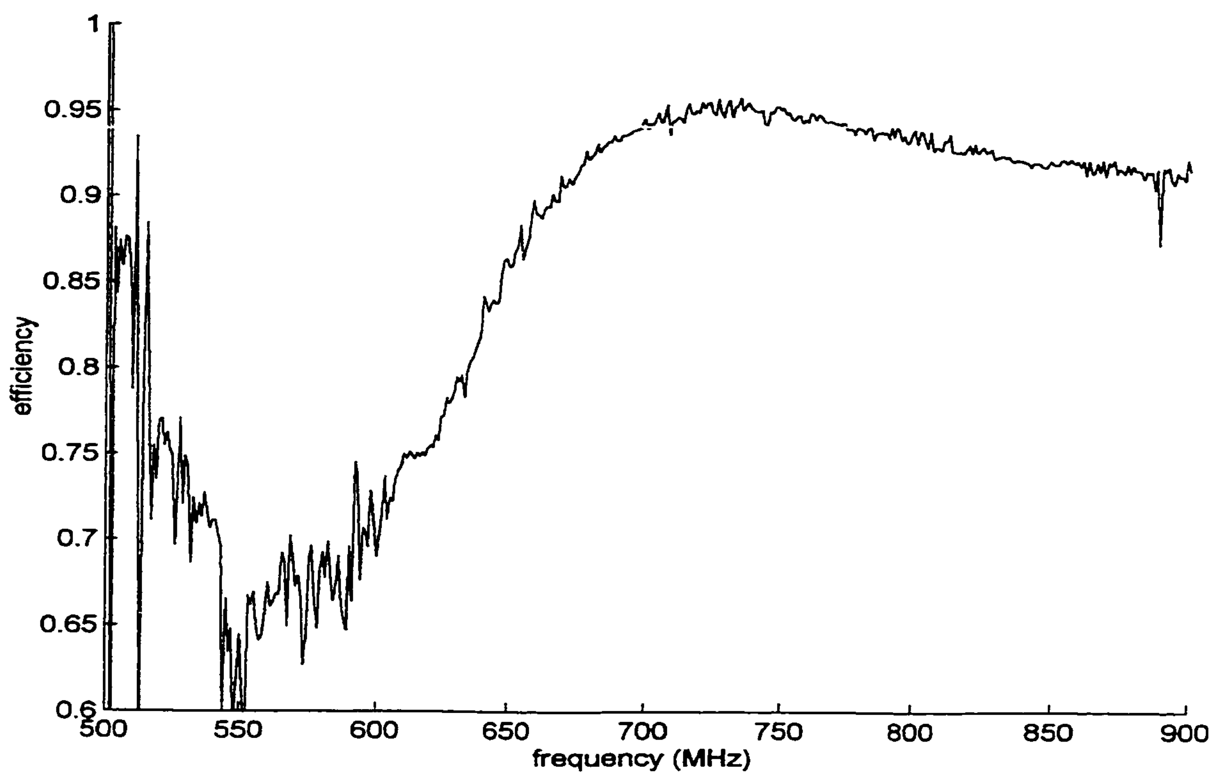

Figure 5.11 Broadband measured efficiency of MED2

There is a spurious area below 600MHz which can be ignored since this is not within the operating frequency range of the enlarged version of MED2. Figure 5.12 plots the efficiency as a function of frequency from 700MHz to 900MHz. The efficiency is over 92% in this range for the enlarged version of MED2 which corresponds to between 1.26GHz and 1.62GHz for the original version of MED2. Due to limited waveguide apparatus, we cannot measure the efficiency of MED2 above 900MHz.

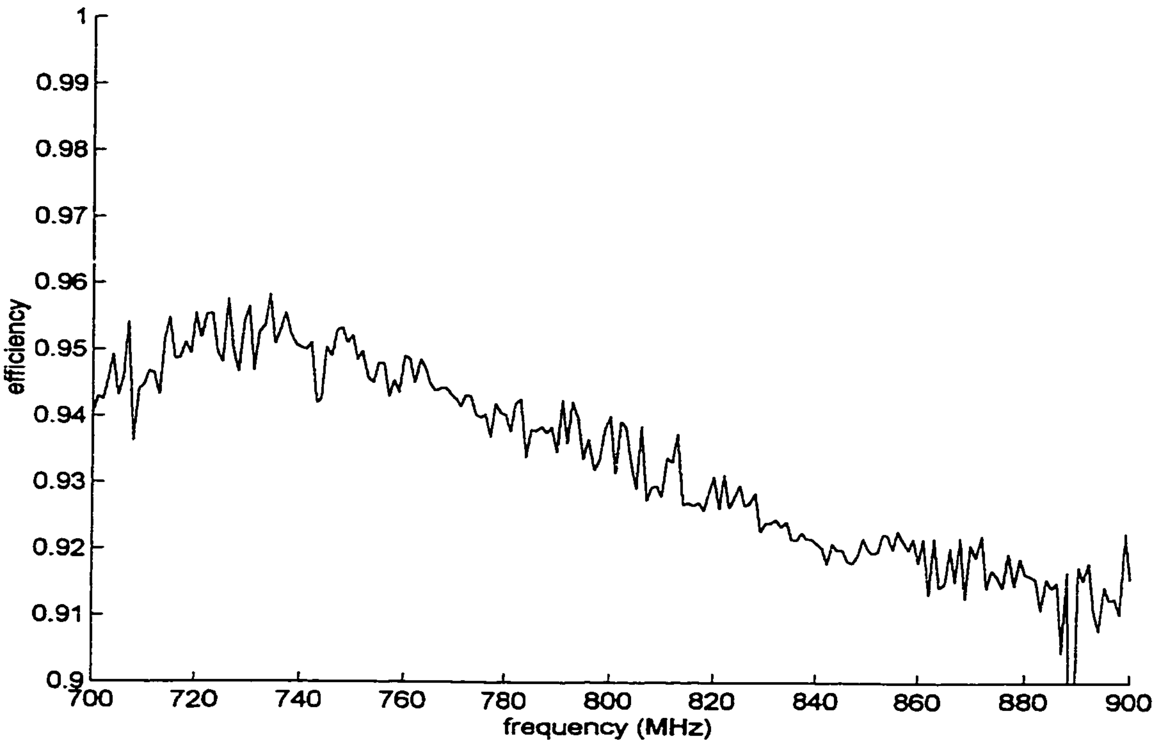

Figure 5.12 In band efficiency of MED2

Chapter 6: Modeling the Magnetic-Electric Dipole

6.1 An equivalent circuit of the MED

After extensive computer simulations and having built a physical antenna, it is often a good idea to derive an equivalent electrical circuit or model of the antenna. An accurate equivalent circuit or model of an antenna can help to characterize the response of the antenna within its operating frequency range. Unlike a computer simulation, an equivalent circuit is "transparent" and will let the engineer look at the input impedance of the antenna. With the equivalent circuit, the designers have another tool to analyze and optimize the performance of antenna input impedance and bandwidth.

6.2 Transmission line model

It is not possible to model an antenna, which operates at microwave frequencies, with solely lumped elements (R, L, C). The action of the antenna cannot always be modeled by a small number of lumped elements but it can be modeled by distributed components [1]. Instead, a combination of transmission lines and open and short circuited stubs are used. A stub is a length of transmission line, either open or short circuited, that is connected in parallel with the signal path.

According to Himdi, an aperture-coupled patch antenna can be modeled by transmission line analysis [2]. Since MED2 is more successful then MED1 in the context of bandwidth (refers to Chapter 5), we only model MED2.

The feeding method of the aperture-coupled patch antenna described in the reference is different from that of MED2; therefore, in order to use the approach described in the reference to model MED2, we have to make some modifications on the proposed equations which will be described later.

Figure 6.1 shows the constitute components of MED2 with some new variables.

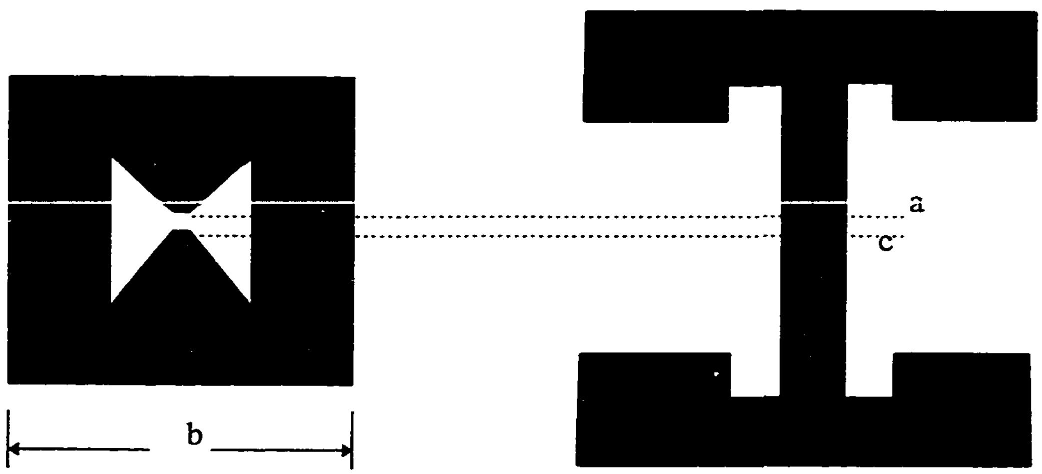

(a) Magnetic dipole (MD) (b) Electric dipole (ED)

Figure 6.1 Constitute components of MED2

According to transmission line analysis [2], the first step is to consider the metallic strip (ED) as a transmission line where TEM waves are propagating. Reflections occur at the ends of the line, where they are modeled as loads $G_{ED} + jB_{ED}$ (conductance and susceptance of the electric dipole). Transmission line of length l_{ED} and characteristic impedance Z_{CED} is used to model half of the metallic strip as shown in Figure 6.1 (b).

Input impedance Z_1 and Z_2 ($Z_1 = Z_2$) are observed in the a and c planes (edges of the feeding slot).

The above approach is depicted in Figure 6.2.

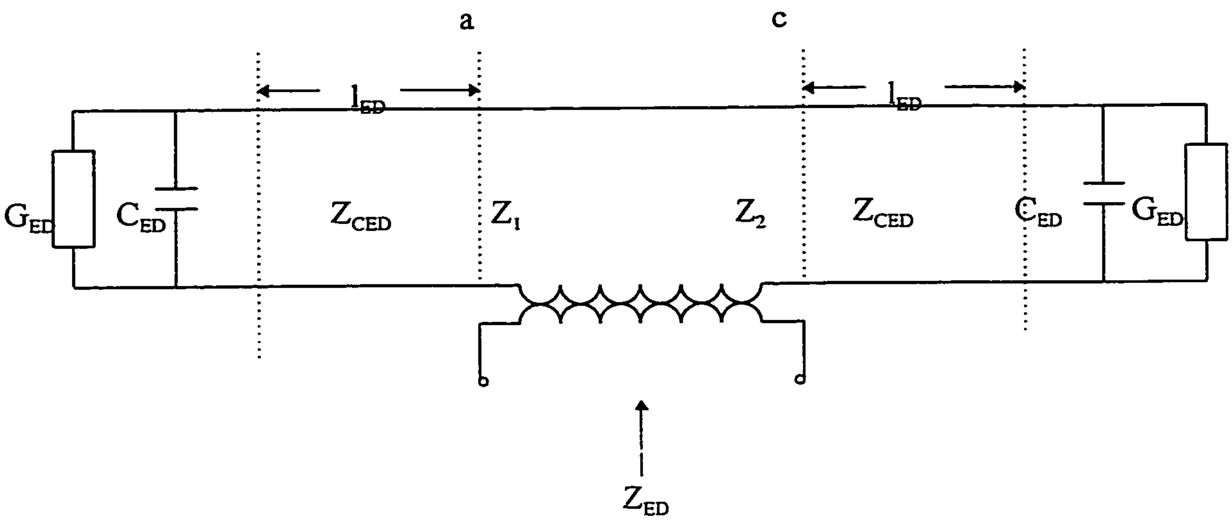

Figure 6.2 Equivalent transmission line and series input transformer of the electric dipole (ED) of MED2

The second step deals with the first input transformer. The slot (MD) of the ground plane collects part of the total current; the transformation ratio n_1 is then equal to the fraction of current flowing through the slot over the total intensity:

$$n_1 \approx \frac{2W_{MD}}{b} \tag{6-1}$$

For a terminated transmission line shown in Figure 6.3,

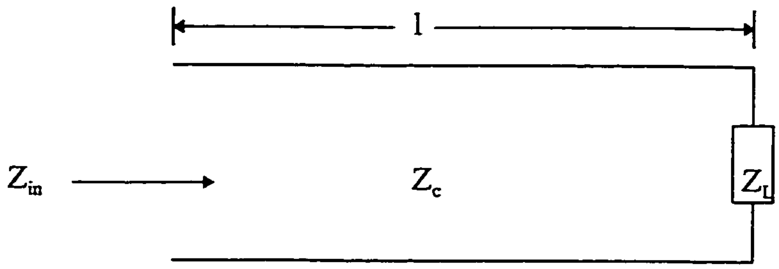

Figure 6.3 A terminated transmission line.

the input impedance Z_{in} looking toward the load can be expressed in the form [3],

$$Z_{in} = Z_c \frac{Z_L + jZ_c \tan\beta l}{Z_c + jZ_L \tan\beta l} \tag{6-2}$$

where Z_c and l are the characteristic impedance and length of the transmission line respectively. Z_L is the load impedance and β is the wave number.

From Figure 6.2 and equation 6.2, it can be shown that

$$Y_{ED} = \frac{1}{Z_{ED}} = \frac{2}{Z_{CED}} \cdot \frac{Z_{CED} + j\tan(\beta l_{ED}) \cdot \frac{1}{G_{ED} + j\omega C_{ED}}}{\left[\frac{1}{G_{ED} + j\omega C_{ED}} + jZ_{CED}\tan(\beta l_{ED})\right]} \tag{6-3}$$

The metallic slot (MD) is modeled with two short-circuited slot lines with characteristic admittance Y_{CMD}. The total equivalent circuit is given in Figure 6.4 where the open stub portion has been removed from the original version as shown in the reference due to the different feeding method.

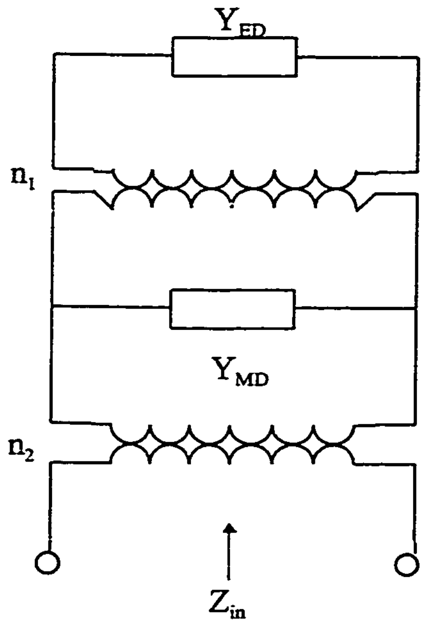

Figure 6.4 Equivalent circuit of MED2.

The susceptance component Y_{MD} includes the stored energy near the slot. The characteristic admittance Y_{CMD} can be determined using Cohn's method [4]; however, it is determined by "trial and error" in this thesis due to complexity. According to reference [2], the second transformation ratio n_2 should be calculated from the discontinuity ΔV in modal voltage of the feeding microstrip line, i.e $n_2 = \Delta V/V_0$ where V_0 is the slot voltage; however, since MED2 employs direct feeding upon the slot, therefore $n_2 = 1$ in the case of MED2.

For MED2, $l_{MD}/2$ is a reactive load, transformed along the width W_{MD}. Finally the slot (MD) admittance Y_{MD} is [5],

$$Y_{MD} = j2Y_{CMD} \frac{-\frac{Y_{CMD}}{2}\cot\left(\beta\frac{l_{MD}}{2}\right) + Y_{CMD}\tan(\beta W_{MD})}{Y_{CMD} + \frac{Y_{CMD}}{2}\cot\left(\beta\frac{l_{MD}}{2}\right)\tan(\beta W_{MD})} \tag{6-4}$$

The expression of the total input impedance is then given by [5],

$$Z_{in} = \frac{n_2^{\ 2}}{n_1^{\ 2}Y_{ED} + Y_{MD}} \tag{6-5}$$

6.3 Comparsion of model, measurements and simulation

A matlab program based on equations (6-3), (6-4) and (6-5) is used to evaluate Z_{in}. The values for all the variables are listed in Table 6.1.

Table 6.1 Input Values for the transmission line model

Variable	Value
l_{ED}	0.078m
l_{MD}	0.023m
W_{MD}	0.034m
G_{ED}	0.12mhos
C_{ED}	10e-15F
Z_{CED}	26Ω
Y_{CMD}	0.012mhos
n_1	0.4
n_2	1

It should be noted that all the values in Table 6.1 were determined by "trial and error". Exact values can be detemined by Cohn's method [4] which is beyond the scope of this thesis.

Figure 6.5 shows the calculated input impedance as a fuction of frequency from 1 to 4GHz based on transmission line model using the variable values as shown in Table 6.1.

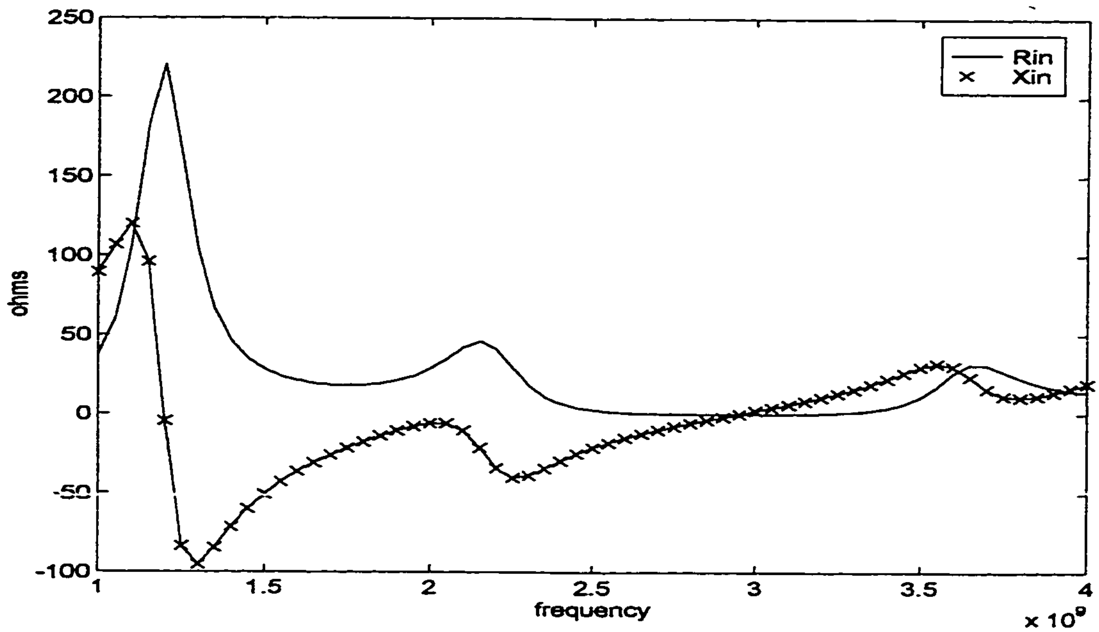

Figure 6.5 Predicted input impedance of MED2 based on transmission line model

Figure 6.6 shows the actual measurement results based on section 5.2.1.

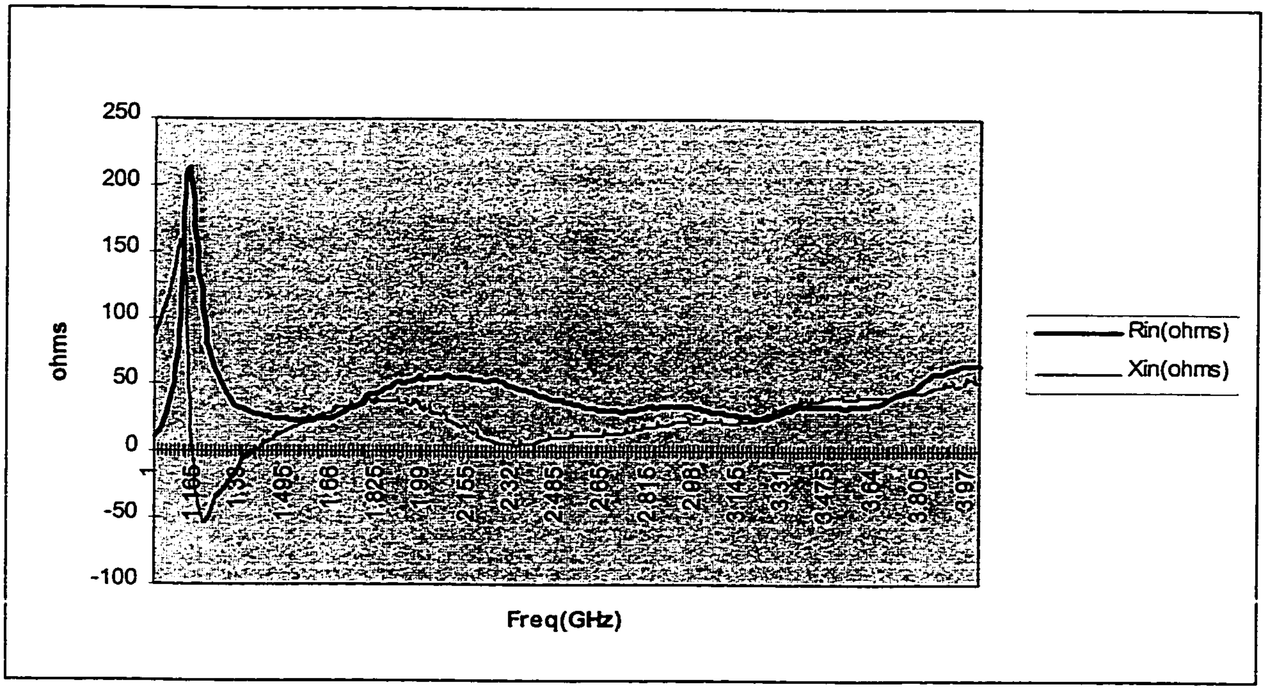

Figure 6.6 Measured input impedance of MED2

The two methods agree with each other very closely. The agreement between the two approaches supports the validity of the transmission line model, which gives the same curves as the actual measurement.

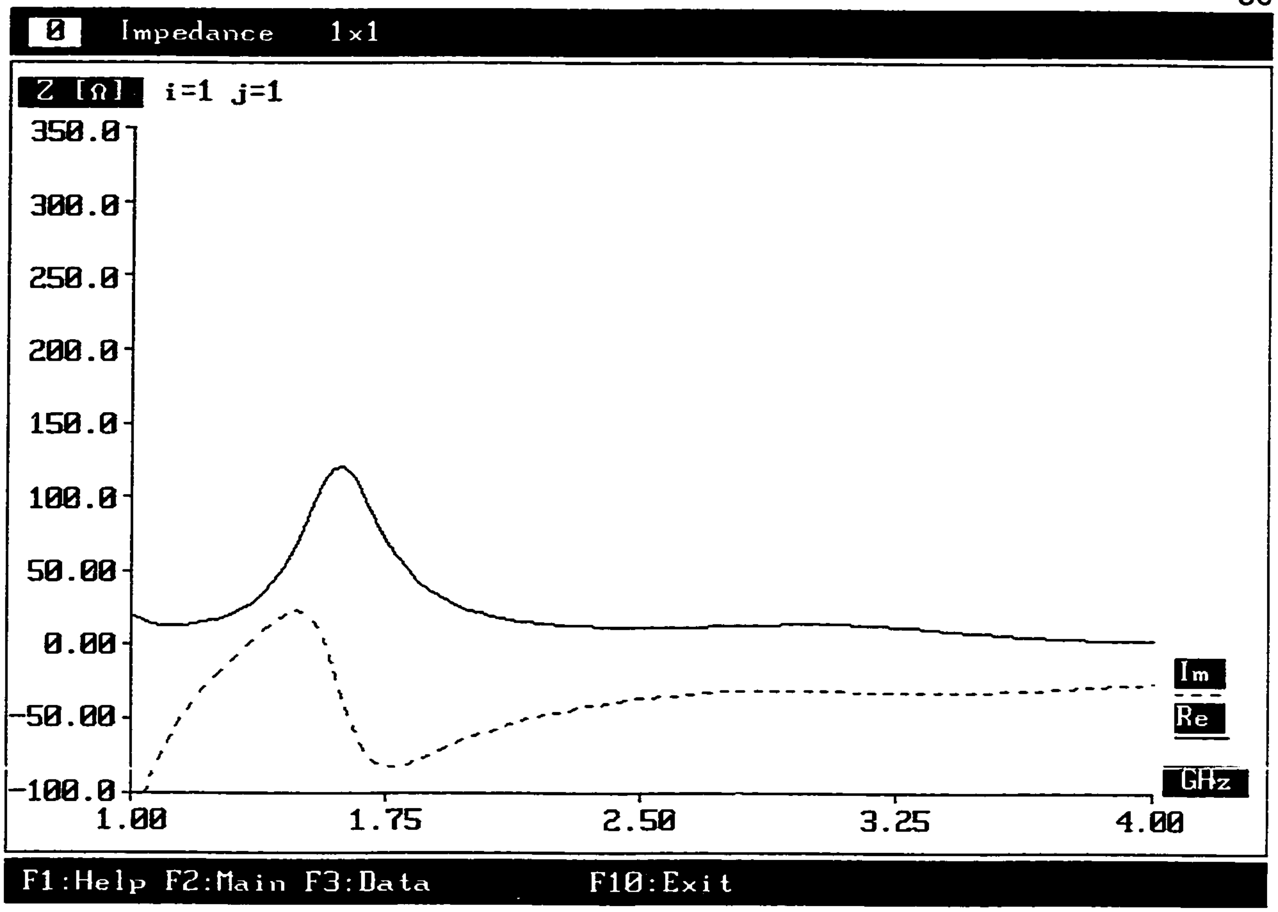

Figure 6.7 WIPL-D simulated input impedance of MED2

Figure 6.7 is the computer simulated results by WIPL-D. It seems that the simulation does not quite agree with the other two approaches, despite the similarity of the general shape of the curves. Therefore, transmission line analysis offers a better physical interpretation of MED2 than WIPL-D simulation does. Nevertheless, WIPL-D simulation is still a helpful and powerful tool for antenna design.

Notes

[1] J. G. McRory, *CAD for Linear and Nonlinear RF/Microwave Circuit Design*, TRLabs, 1996, p.23.

[2] C. Terret, M. Himdi, and J. P. Daniel, "Transmission line analysis of aperture-coupled microstrip antenna," *Electronic Letters*, vol. 25, no.18, Aug. 1989.

[3] R. E. Collin, *Antennas and Radiowave Propagation*, McGraw-Hill, 1985, pp. 463-464.

[4] M. Himdi and J. P. Daniel, " Characteristics of sandwich-slotlines in front of a parallel metallic strip," *Electrics Letters*, vol. 27, no. 5, Feb. 1991.

[5] M. E. Yazidi, M. Himdi, and J. P. Daniel, "Transmission line analysis of nonlinear slot coupled microstrip antenna," *Electronic Letters*, vol. 28, no.15, July 1992.

Chapter 7: The Shielded Slot Antenna

7.1 Construction of the Shielded Slot Antenna (SSA1)

Slot antennas, like the magnetic dipoles described in Chapter 4, are low profile, conformable to planar surfaces, simple and inexpensive to manufacture using modern print-circuit technology and mechanically robust which make them particularly suitable for portable device applications. The prototype of the Shielded Slot Antenna (SSA) started from a rectangular slot as shown in Figure 7.1.

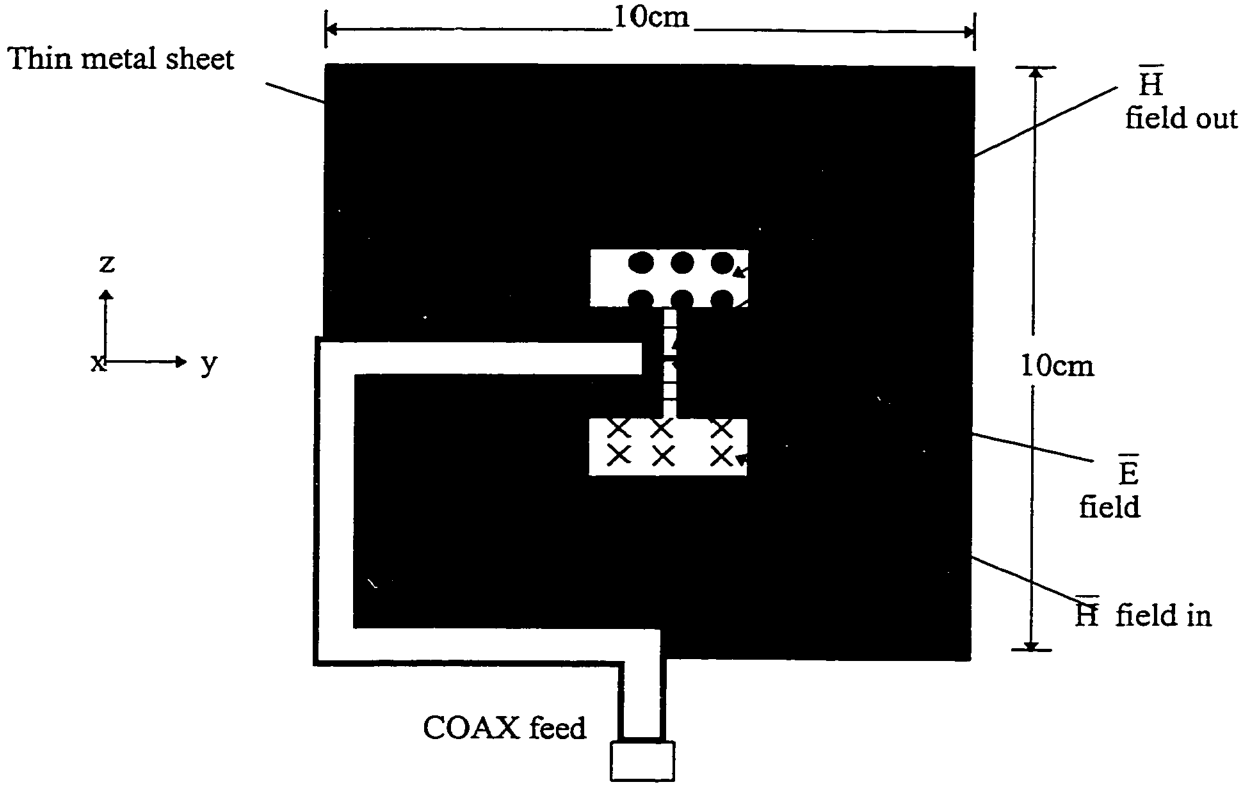

Figure 7.1 Rectangular Slot Antenna.

Figure 7.1 also shows the $\bar{E}$ and $\bar{H}$ field orientations and the exact dimensions of the slot antenna. The resonant frequency of this antenna is 1.19GHz.

Our objective was to build a shielded slot antenna which should have strong radiation on one side (the side facing away from the user) but weak radiation on the other side (the side facing toward the user); however, it is obvious that the slot antenna in Figure 7.1 has equal radiation on both sides.

Borrowing the idea from an electromagnetic wave polarizer which can block the electric field (when in the right orientation), 12 wires of radius 0.3mm were soldered to one side of the rectangular slot shown in Figure 7.1. The resulting slot antenna with $\bar{E}$ field polarizer is shown in Figure 7.2 which we will call SSA1.

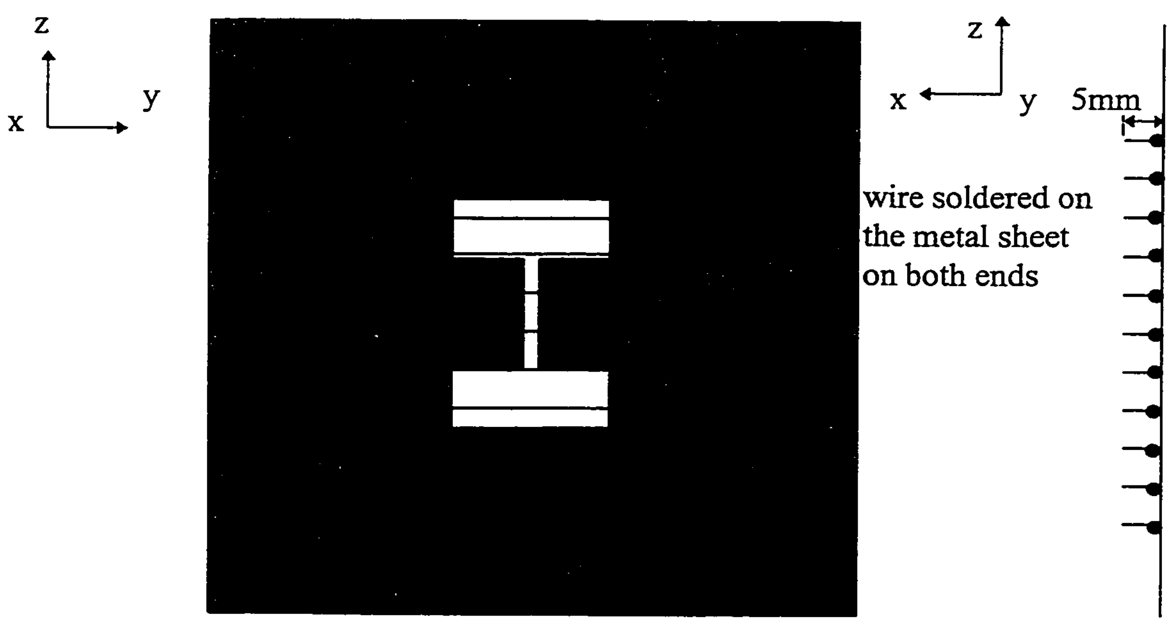

(a) Front view

(b) Side view

Figure 7.2 SSA1

Note that the coax feed line (not shown in Figure 7.2) and all the dimensions are the same as those in Figure 7.1.

The specific absorption rate (SAR) in human tissue is directly related to the near field of the transmitting antenna; the near field measurement described in Section 3.2 was performed on SSA1. It was found that the side with the wires has about 3db less radiation in the y-direction ($\bar{E}_y$). This can be explained as: when the $\bar{E}$ field in Figure 7.1 ($\bar{E}_y$) impinges upon the wires, current will be induced and flowing on the wires in the y direction. As a result, radiation is reflected or shielded on one side of the slot.

With the wires, the resonant frequency is increased from 1.19GHz to 1.57GHz. This prototype electromagnetic shield antenna does block some radiation on one side; however, it is too large to fit in any portable device and the shielding effect is insufficient. In view of this, we used WIPL-D to simulate some variations on the prototype.

7.2 Shielded Slot Antenna #2 (SSA2)

Since a "bow-tie" slot antenna is more broadband than a rectangular slot antenna, we began the WIPL-D simulation on a "bow-tie" slot with shielding wires. Figure 7.3 shows the corresponding antenna which we will call SSA2. Note that, unlike SSA1, there is no direct contact between the wires and the slot.

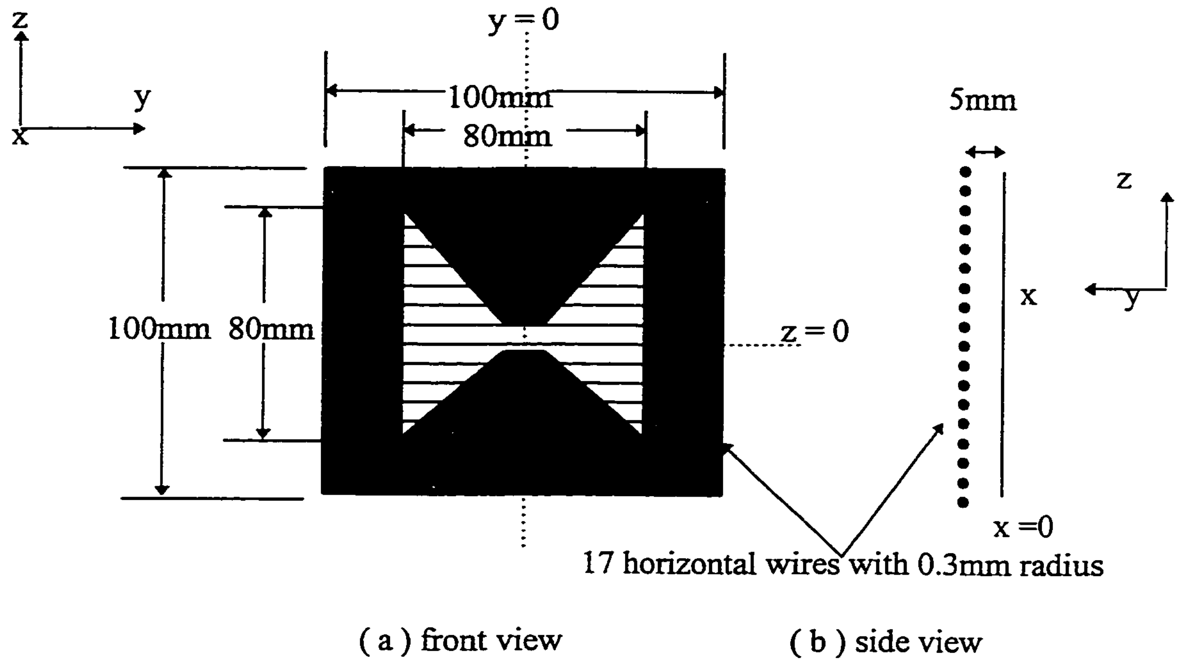

Figure 7.3 SSA2

According to WIPL-D, SSA2 has a minimum $|S_{11}|$ or return loss of 0.4 or 8dB at 1.8GHz. As shown in Figure 7.3, SSA2 is excited across the gap in the Z direction; therefore, the dominant electric field component of SSA2 is E_z. There is almost no electric field component in the y direction; therefore, we are not concerned with the E_y variation along the x-axis. Figure 7.4 and 7.5 show the WIPL-D simulation of the magnitude of E_z and E_x along the x-axis of the antenna ($z = 0$, $y = 0$) at 1.8GHz.

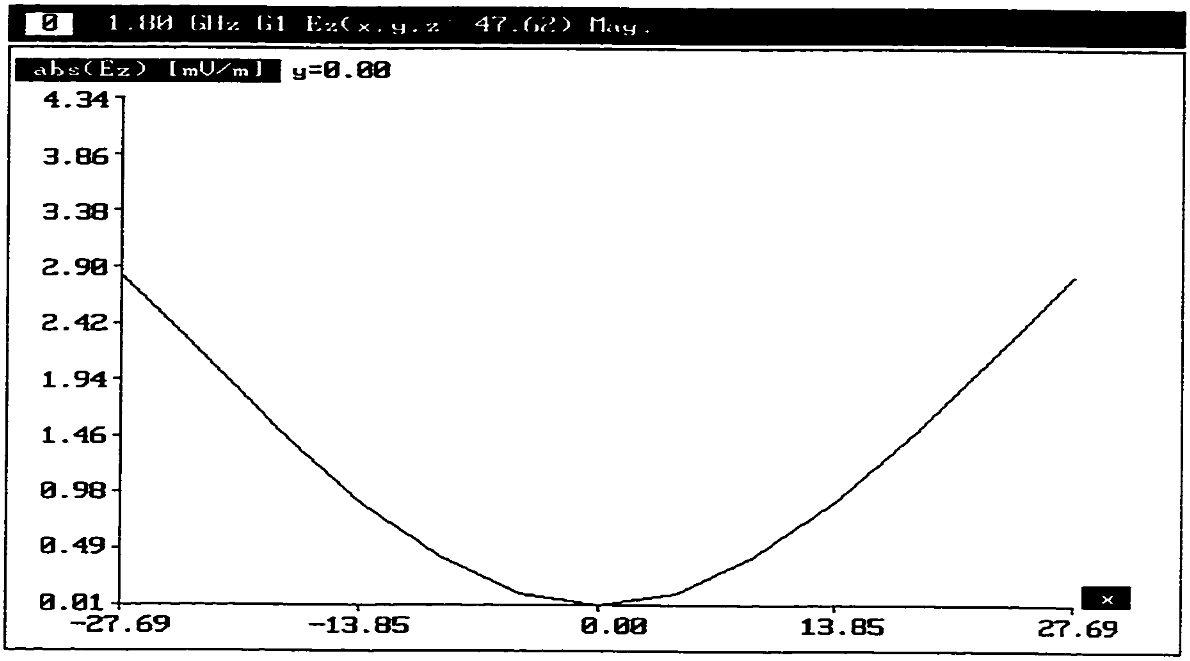

Figure 7.4 WIPL-D simulation of abs(E_z) of SSA2 at 1.8GHz

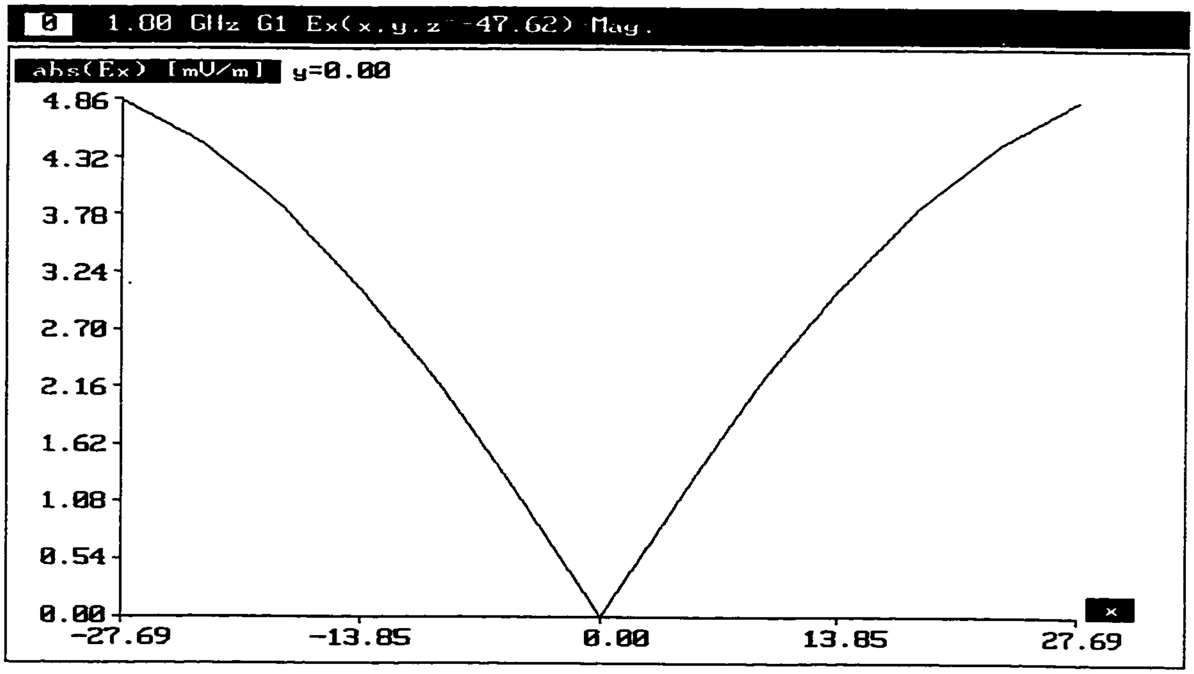

Figure 7.5 WIPL-D simulation of abs(E_x) of SSA2 at 1.8GHz

From the graphs, we know that the wires create no shielding effect since $|E_z|$ and $|E_x|$ are equal on both sides (+x and -x) of SSA2.

7.3 Shielded Slot Antenna #3 (SSA3)

Since SSA1 and SSA2 are too large to fit in portable devices, the length and the width of the next antenna prototype going to be simulated will be halved. Moreover, the wires are rotated 90° as compared with SSA2. The resulting antenna (SSA3) is shown in Figure 7.6.

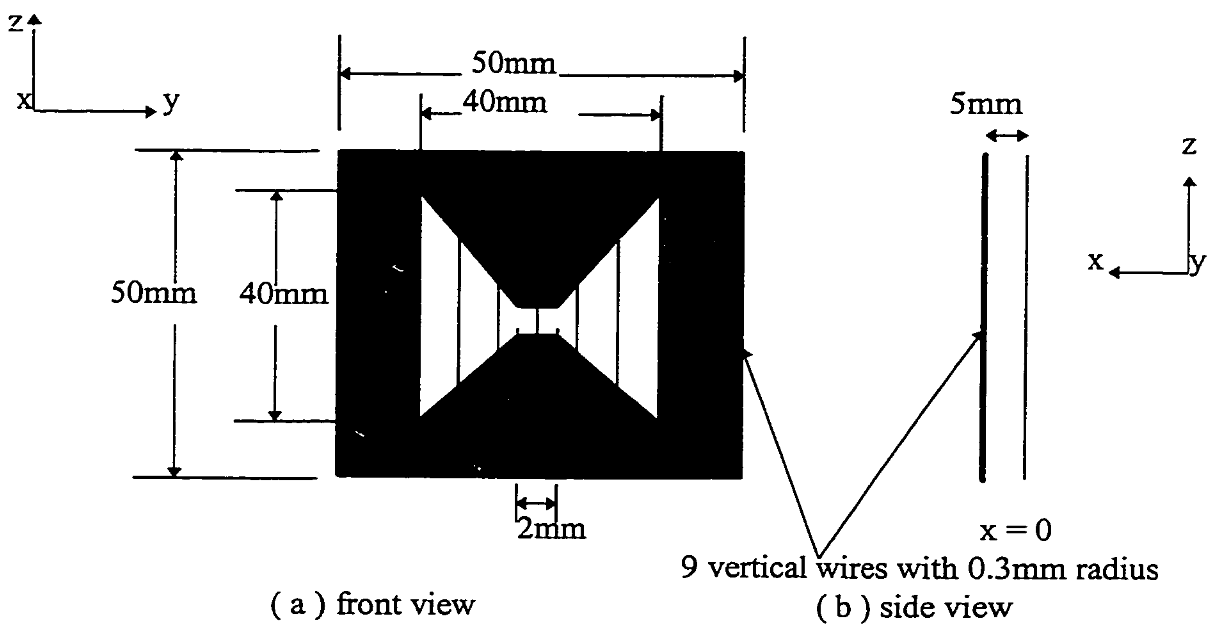

Figure 7.6 SSA3

According to WIPL-D, SSA3 has a minimum $|S_{11}|$ of 0.4 or 8dB at about 2.4GHz. Again, we are only concerned with the $|E_z|$ and $|E_x|$ variation along the x-axis (z = 0, y = 0). Figure 7.7 and 7.8 show the simulated results at 2.4GHz.

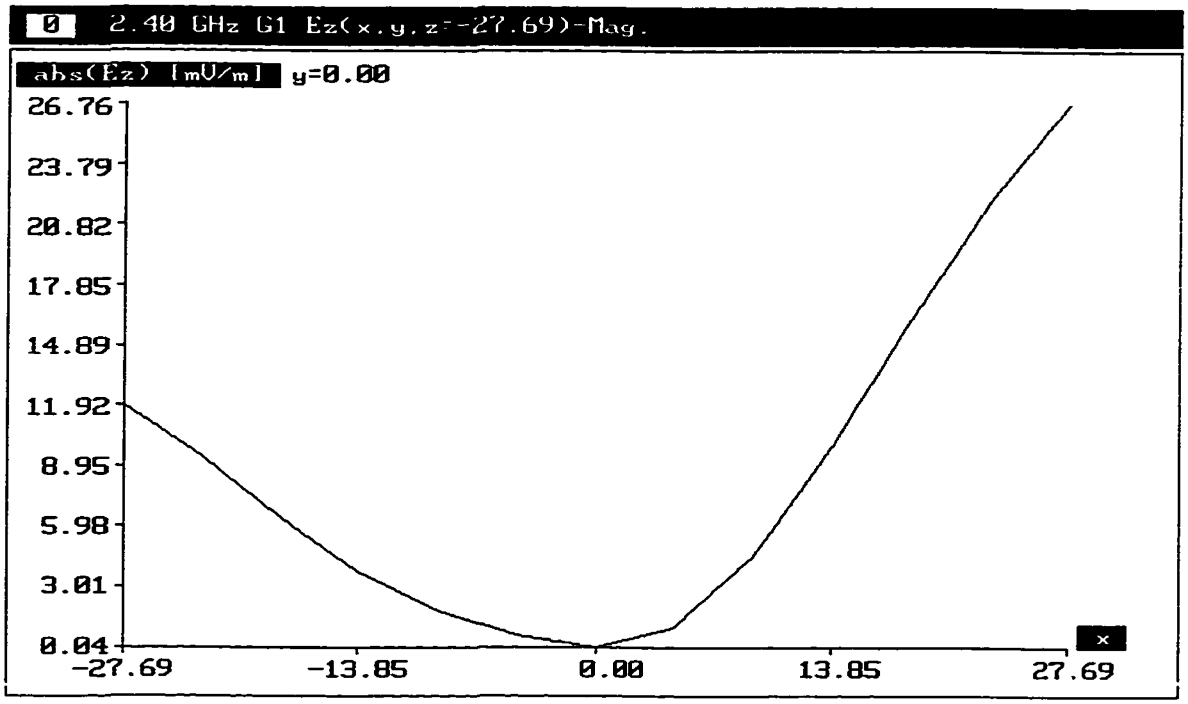

Figure 7.7 WIPL-D simulation of abs(E_z) of SSA3 at 2.4GHz

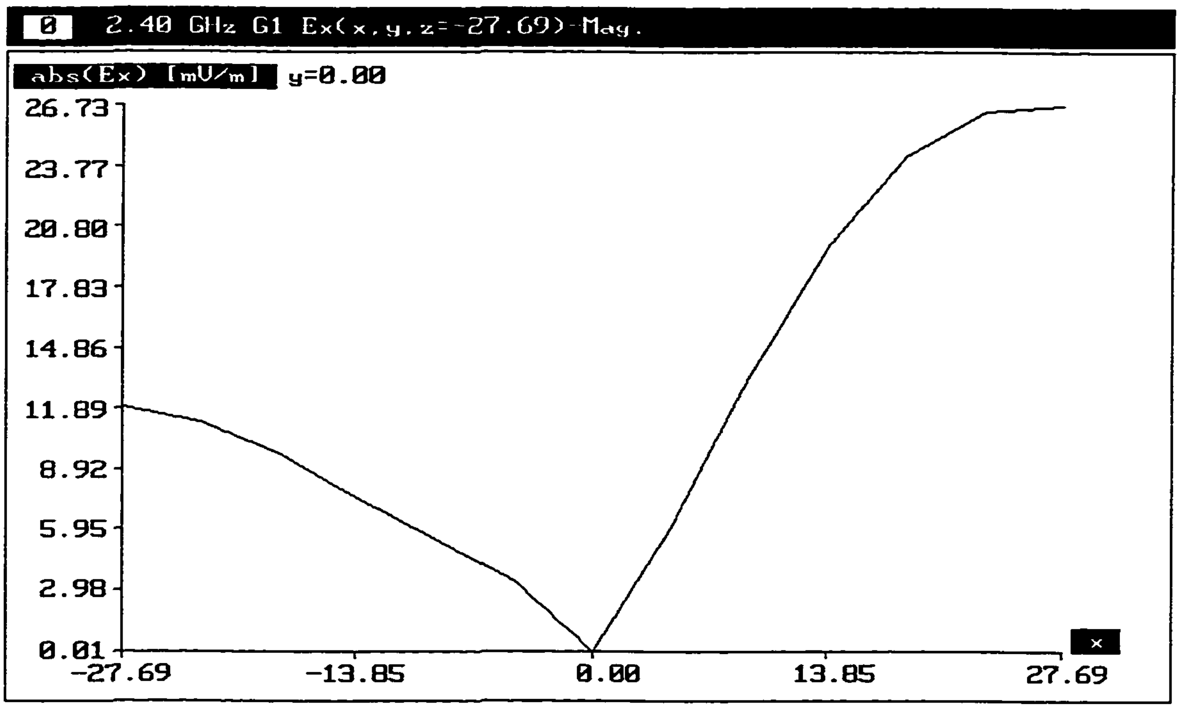

Figure 7.8 WIPL-D simulation of abs(E_x) of SSA3 at 2.4GHz

It is clear that SSA3 radiates more on the wire' side (+x). This is apparently because, with the correct alignment (z direction), the wires pick up some energy from the slot antenna and re-radiates it, and so the wires become a radiator instead of a shield.

7.4 Shielded Slot Antenna #4 (SSA4)

Figure 7.9 details SSA4. It can be considered as the combination of SSA2 and SSA3. It consists of vertical as well as horizontal wires soldered together creating a screen made up of rectangular grids.

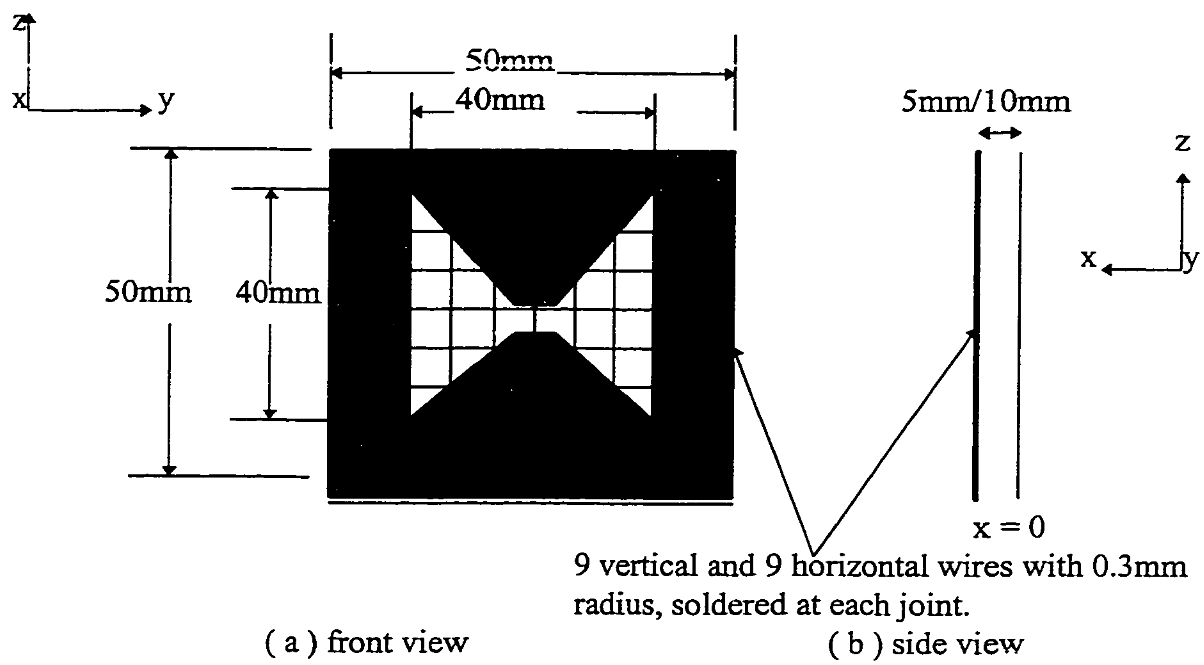

Figure 7.9 SSA4

The purpose of soldering the horizontal wires upon the vertical wires is to short the current flowing on the vertical wires as in the case of SSA3, thus preventing any reradiation from the vertical wires. If this is true, the screen would be a shield rather than a re-radiator. We simulated SSA4 by WIPL-D with the gap distance between the screen and the slot equaled to 5mm and 10mm respectively. However, the simulation results show that there is still more radiation on the screen side of the antenna irrespective to the gap distance.

7.5 Shielded Slot Antenna #5 (SSA5)

Antenna SSA5 is shown in Figure 7.10. It is modified from SSA4 by shorting the screen and the slot around the four boundaries with wires of 0.3mm radius and 10mm length.

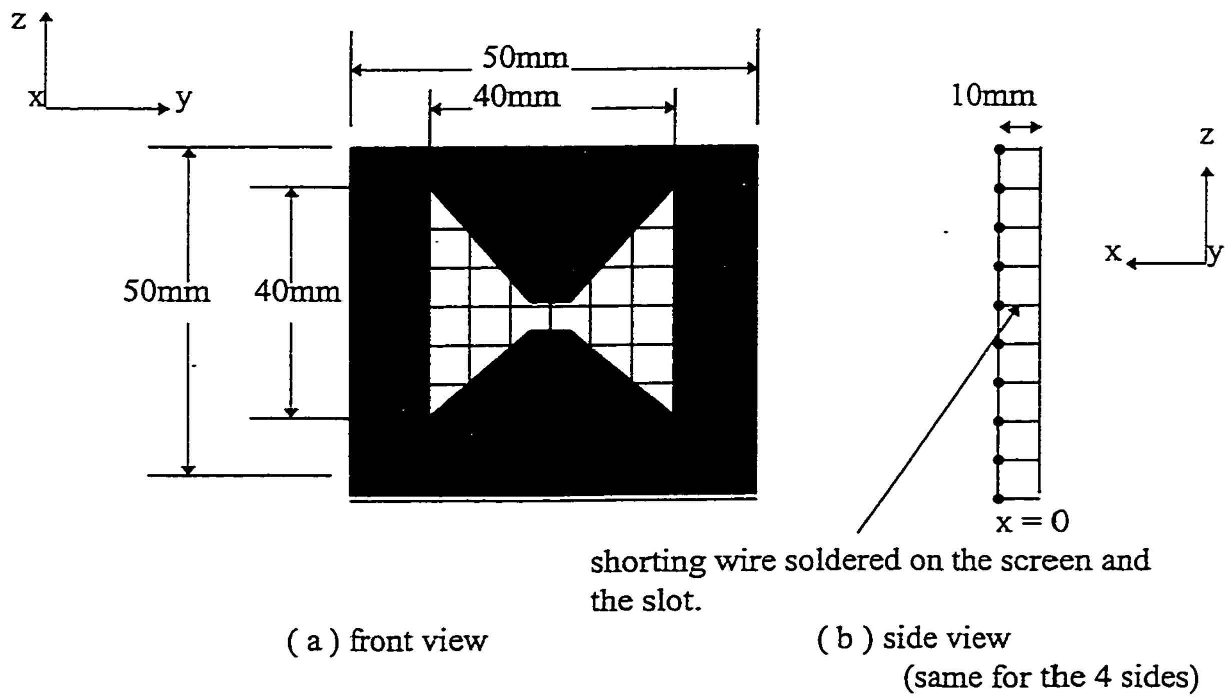

Figure 7.10 SSA5

This antenna resonates at a higher frequency than the other shielded slot antennas. The operating frequency should be at least 4GHz to achieve the 3dB return loss criterion. Below 3.5GHz, the return loss is very high and there is very little radiation. Figures 7.11 and 7.12 show the WIPL-D simulated results of $|E_z|$ and $|E_x|$ along the x-axis of SSA5 at 4.5GHz. At 4.5GHz, the return loss is about 5dB.

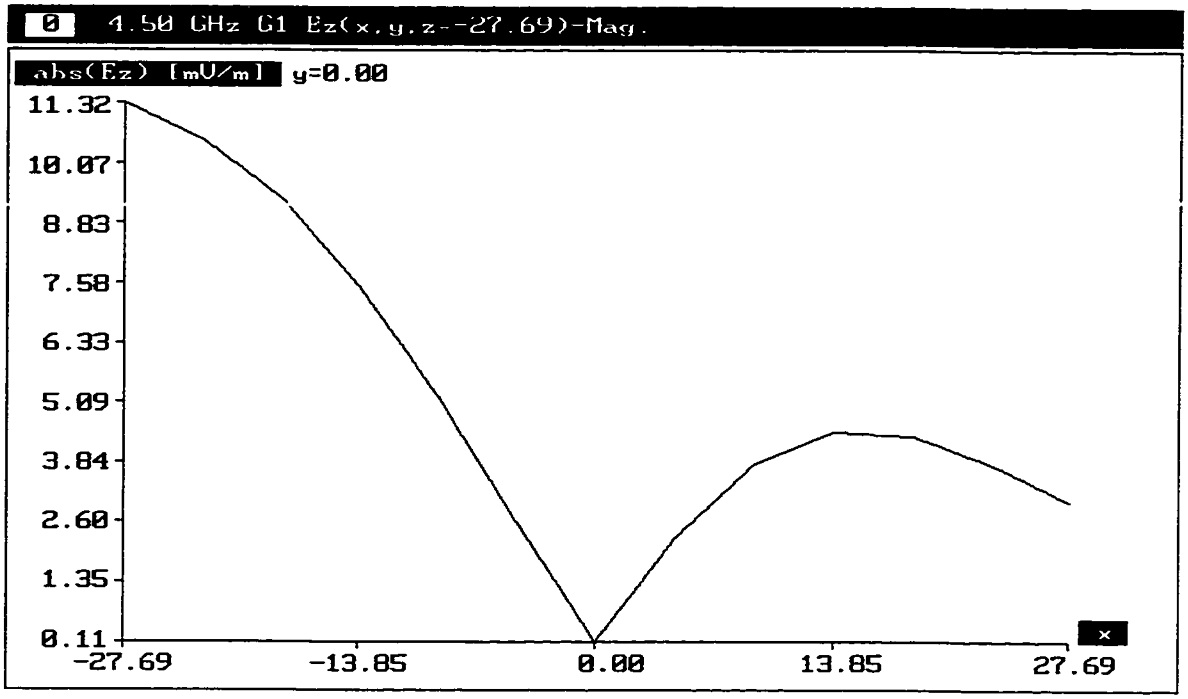

Figure 7.11 WIPL-D simulation of abs(E_z) of SSA5 at 4.5GHz

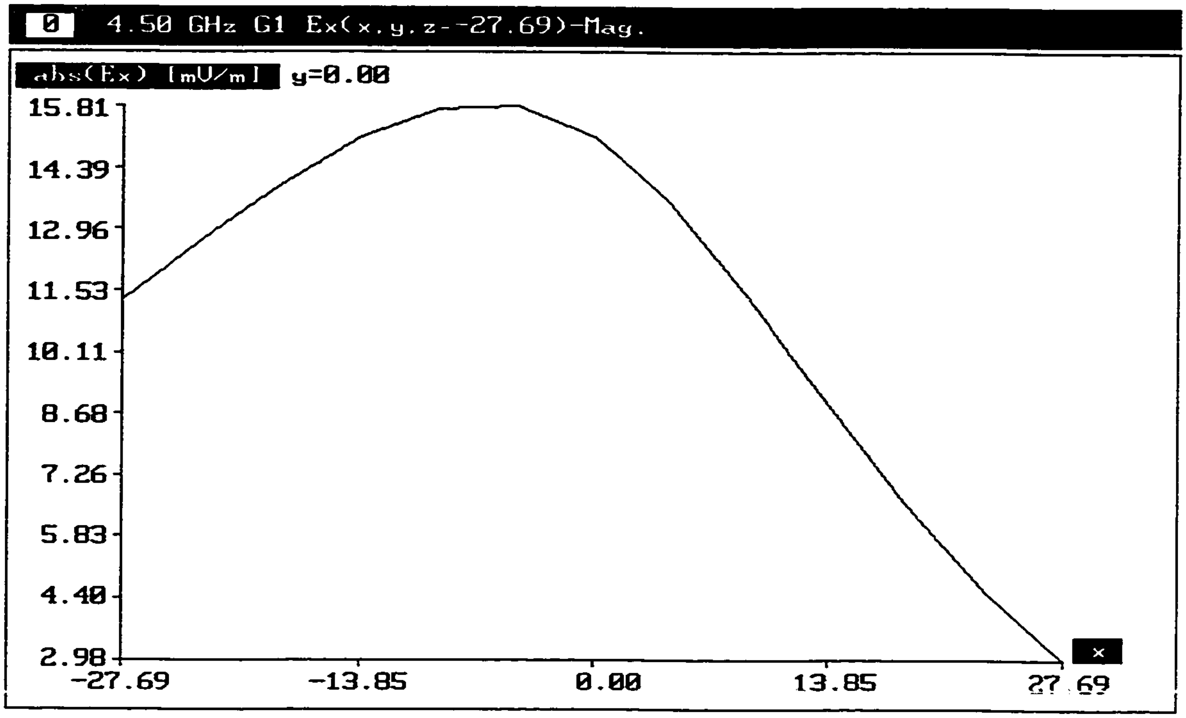

Figure 7.12 WIPL-D simulation of abs(E_x) of SSA5 at 4.5GHz

As shown in the graphs, the screen with the shorting wires acts as a good shield and blocks the radiation to the one side. As can be seen in Figures 7.11 and 7.12 and comparing the x = +27.69mm and x = -27.69mm points, there is about 11dB less radiation on the screen's side (x = +ve).

Based on the simulated results of SSA1 to SSA5, it can be concluded that in order to create a shielding effect, the screen must have direct electrical contact with the main slot antenna; otherwise, the screen becomes a radiator instead. Although SSA5 has a good shielding characteristic, it is not an ideal antenna. This is because 1) the shorting wires are very difficult to construct and they make the antenna very fragile, and 2) the operating frequencies are too high with respect to the overall size of the antenna.

7.6 Shielded Slot Antenna #6 (SSA6)

In order to make the antenna structure more robust, the shorting wires in the four boundaries of SSA5 were replaced by four shorting metal plates. The resulting structure (SSA6) is shown in Figure 7.13.

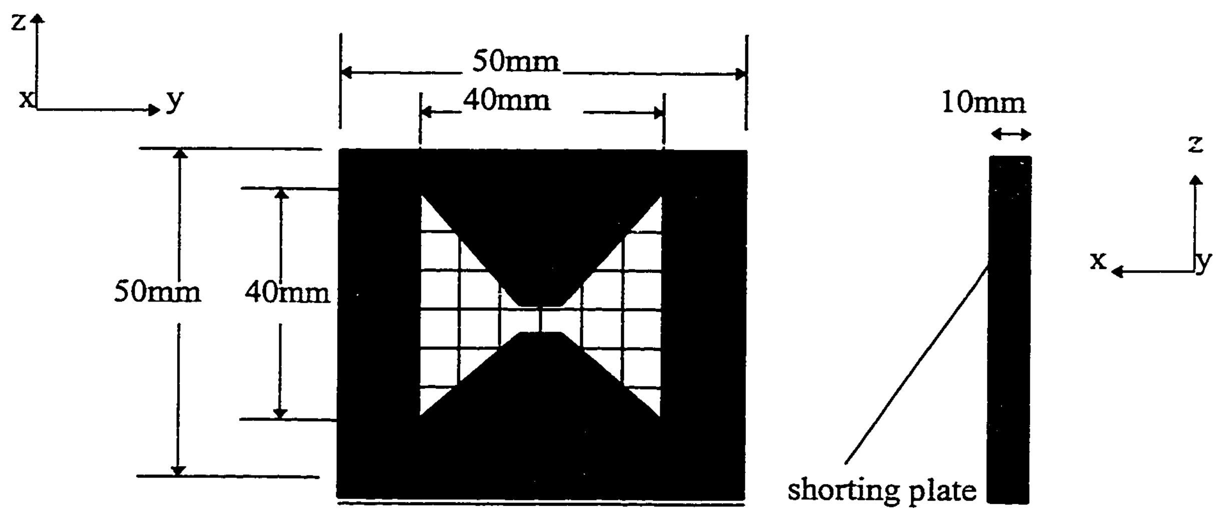

Figure 7.13 SSA6

The simulated return loss or $|S_{11}|$ plot of SSA6 from 1.4GHz to 2.4 GHz is shown in Figure 7.14.

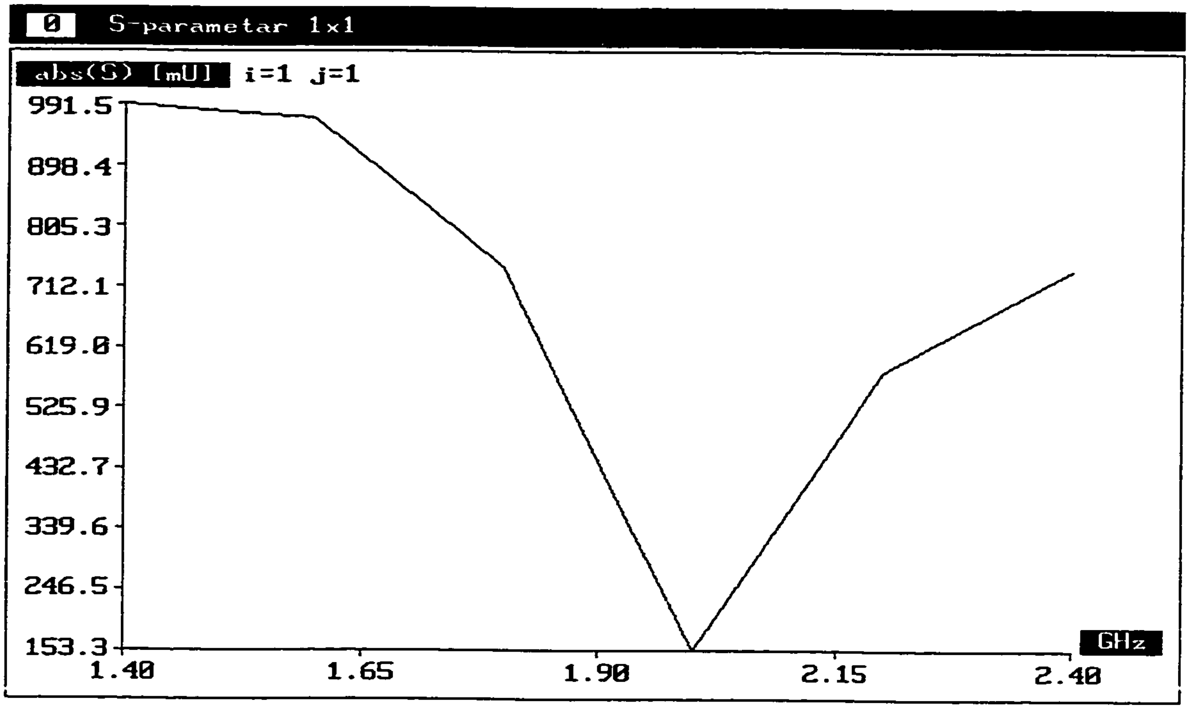

Figure 7.14 WIPL-D simulated return loss of SSA6

The antenna has a very good match at 2GHz with a return loss of 16dB. The 3dB bandwidth is about 400MHz, from 1.9GHz to 2.3GHz. This is a very good news since the operating frequencies are dropped a lot as compared with SSA5.

Since $|E_z|$ is the dominant electric field component, and it alone gives enough near field information, so from now on, only $|E_z|$ plot will be presented. Figure 7.15 is the WIPL-D simulation of $|E_z|$ along the x-axis of SSA6 at 2GHz.

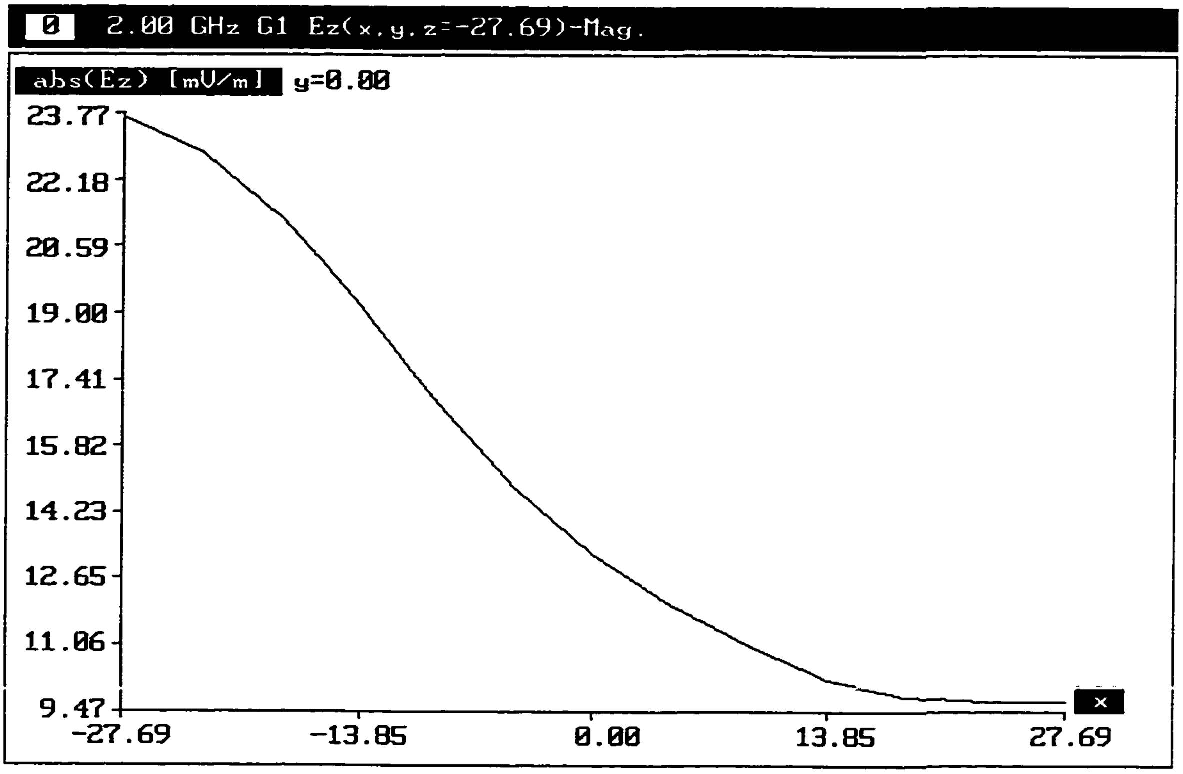

Figure 7.15 WIPL-D simulation of abs(E_z) of SSA6 at 2GHz

The magnitude of E_z is gradually decreasing, as x is moving from negative to positive. At ± 27.69mm from the x-plane, there is about 7.7dB difference in the magnitude of E_z. Similar results are obtained in the frequency range from 1.8GHz to 2.4GHz.

SSA6 has eliminated the drawbacks of SSA5: 1) fragile, and 2) high operating frequencies. The next step is to try to place an extra radiator on the other side of SSA6 so that more energy could be drawn from the slot, and hence reinforcing the shielding effect.

7.7 Shielded Slot Antenna #7 (SSA7)

SSA7 is constructed from SSA6 by adding an additional radiator on the other side of the slot. Recalling SSA3 that vertical wires with no direct electrical contact to the slot would become a radiator, so vertical wires are used as a radiator in SSA7 as shown in Figure 7.16.

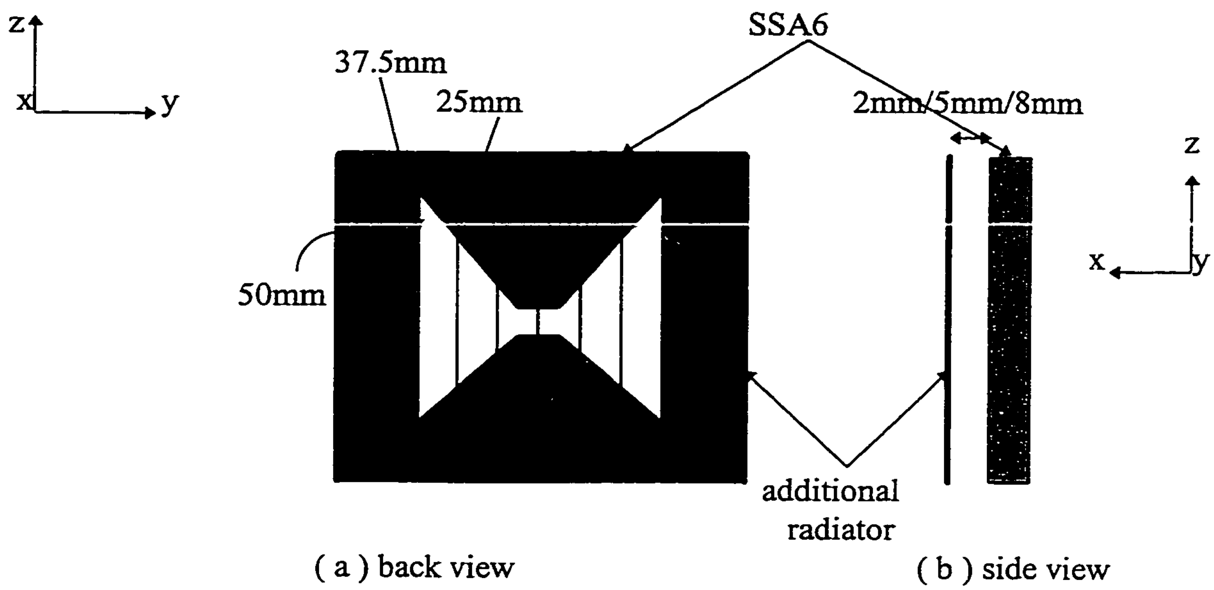

Figure 7.16 SSA7

The radiator's wires are made different length so that a broader bandwidth could be achieved. Figure 7.17 shows the simulated return loss for a gap distance equals to 5mm between the radiator's wires and the slot from 1.4GHz to 2.4 GHz.

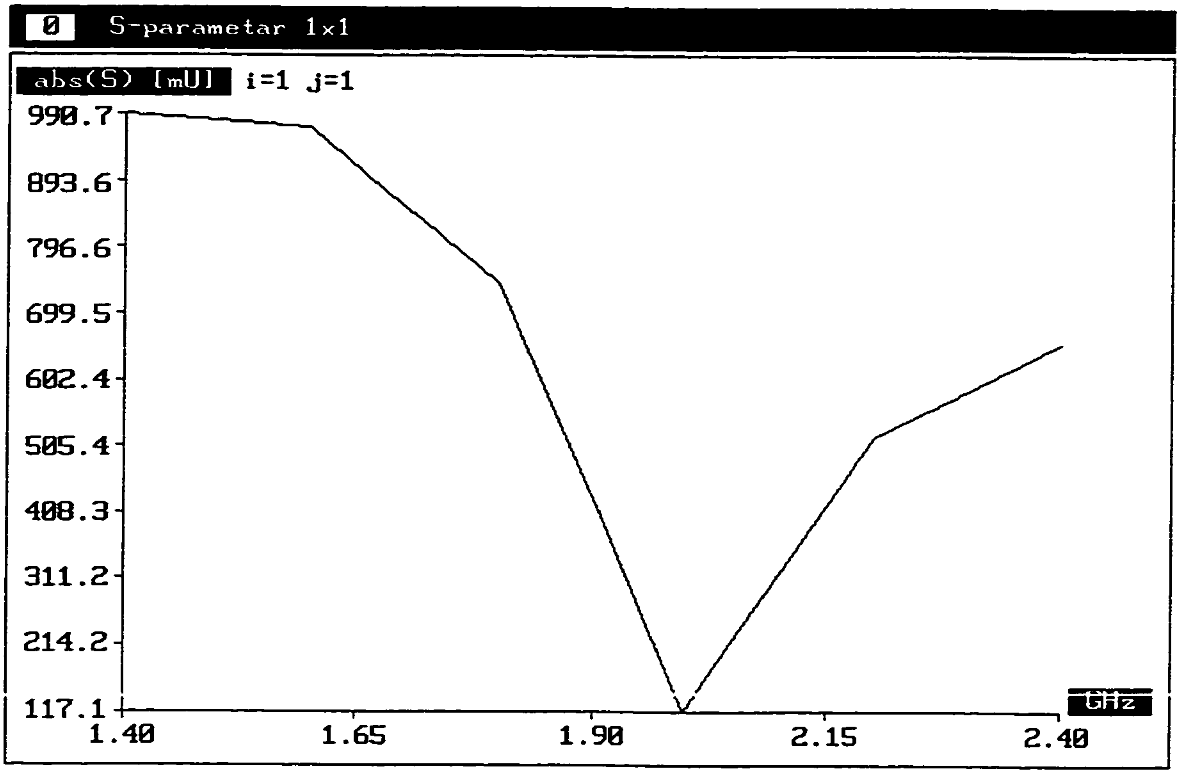

Figure 7.17 WIPL-D simulated return loss of SSA7 (radiator gap = 5mm)

The antenna has a very good match at 2GHz with a return loss of 18.6dB. The 3dB bandwidth is about 400MHz, from 1.9GHz to 2.3GHz. Figure 7.18 shows the WIPL-D simulation of $|E_z|$ along the x-axis of SSA7 at 2GHz.

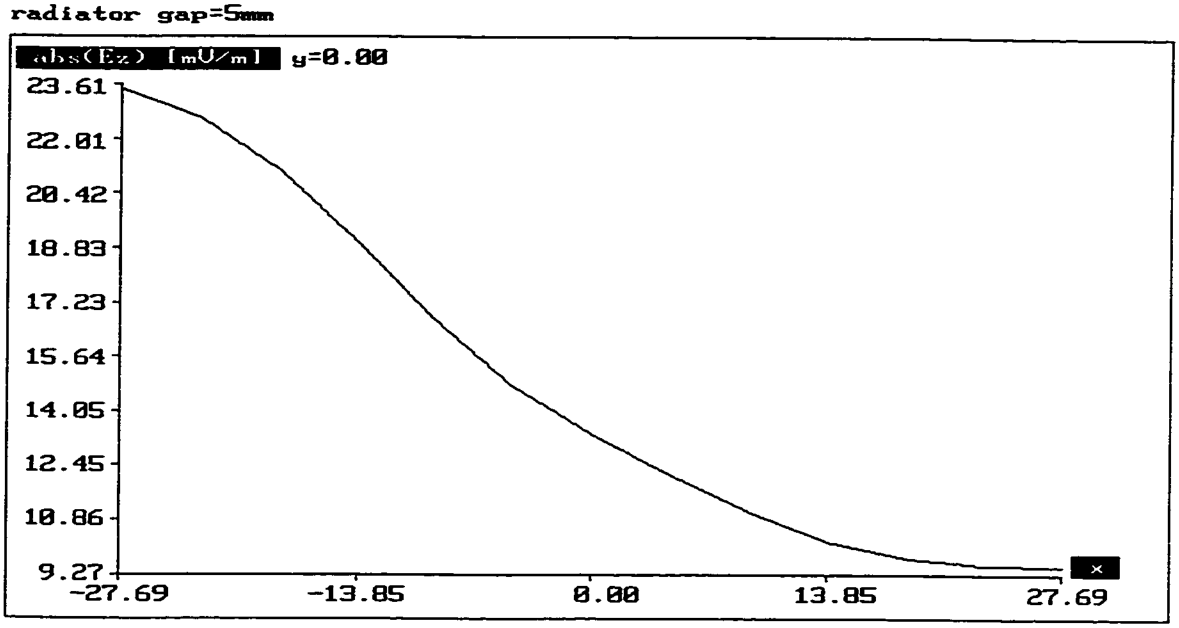

Figure 7.18 WIPL-D simulation of abs(E_z) of SSA7 at 2GHz

Other radiator gap distances (2mm and 8mm) also give similar results as shown in Figures 7.17 and 7.18. We found that the return loss and near field characteristics of SSA7 are almost the same as those for SSA6; therefore, the set of vertical wires as a radiator do not provide any beneficial effects.

7.8 Shielded Slot Antenna #8 (SSA8)

A rectangular metal plate of various length and width was added to SSA6 as an additional radiator to improve the radiation and the bandwidth. According to simulations, we found out that the longer the length (z direction) of the plate, the lower the operating frequencies; and the wider the width (y direction) of the plate, the broader the bandwidth. In order to maximize bandwidth, lower frequency and not enlarge the size of the overall antenna, a rectangular metal plate of length and width which are the same as the main antenna (50mm x 50mm) is used as the additional radiator. Figure 7.19 shows the resulting structure, SSA8.

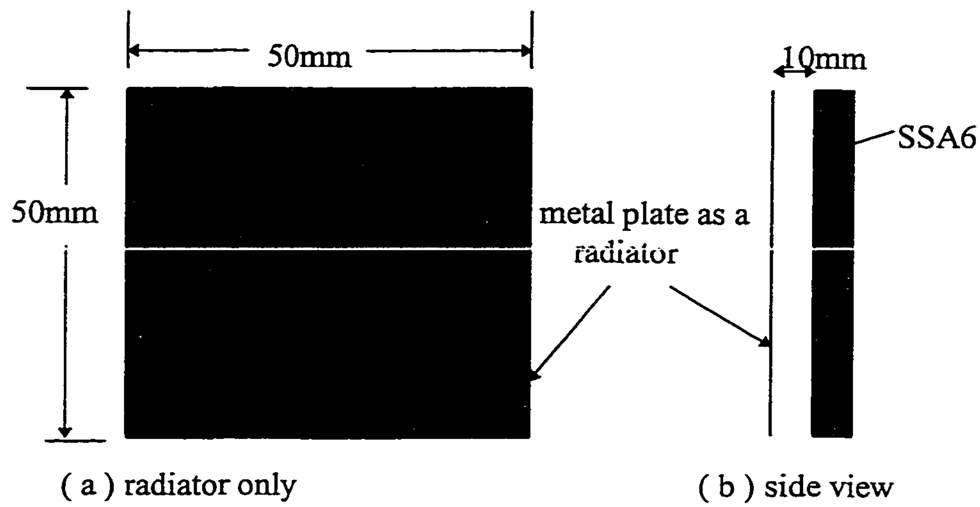

Figure 7.19 SSA8

The metal plate in SSA8 uses the available space most effectively. The WIPL-D simulated return loss from 1.4GHz to 2.8 GHz is shown in Figure 7.20.

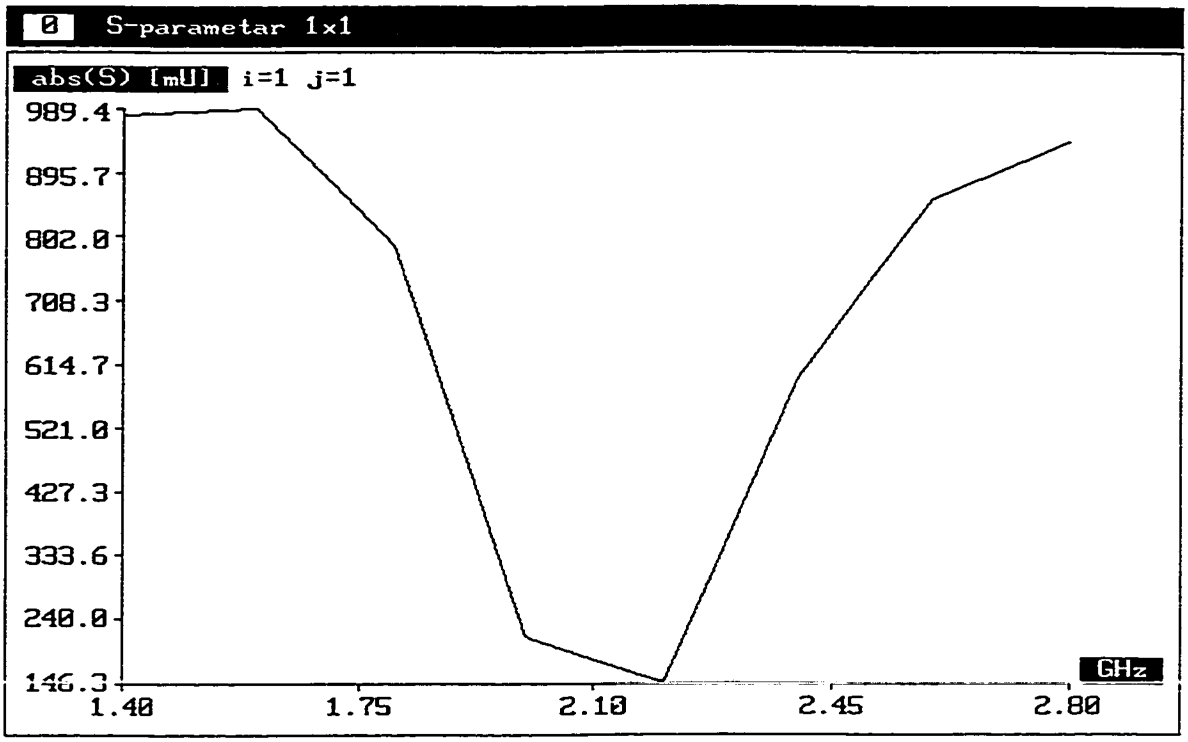

Figure 7.20 WIPL-D simulated return loss of SSA8

The simulated 10dB bandwidth is from about 1.9GHz to 2.3GHz which is quite broadband. Figure 7.21 shows the simulated $|E_z|$ plot along the x-axis of SSA8 at 2.2GHz, which reveals very good shielding characteristics. By comparing the x = +27.69mm and x = -27.69mm points, there is about 13dB less radiation on one side (x = +ve). Similar shielding characteristics are obtained from 1.6GHz to 2.8 GHz.

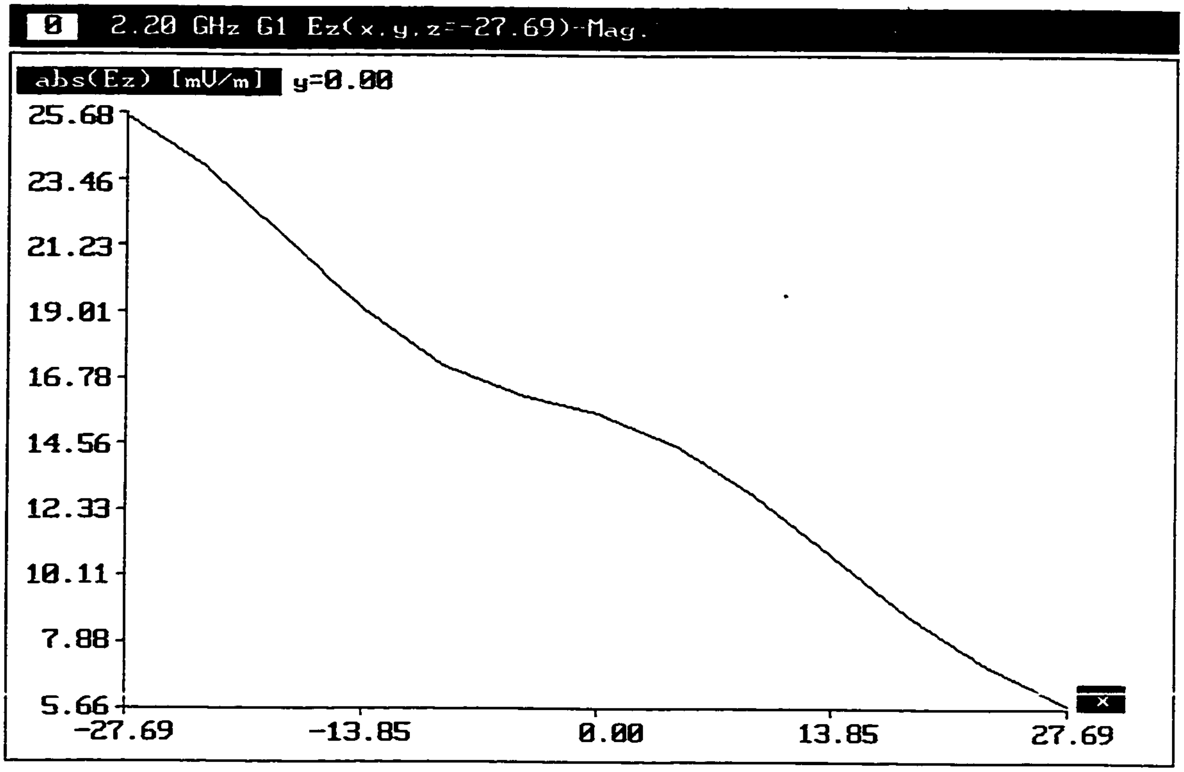

Figure 7.21 WIPL-D simulation of abs(E_z) of SSA8 at 2.2GHz

SSA8 was then built and experimentally tested on the bench. The experimental procedures were described on Chapter 3, and the experimental results are presented on Chapter 8.

Chapter 8: Experimental Results of SSA8

Figure 8.1 is the perspective view of SSA8. The exact dimensions of SSA8 that was constructed for carrying the experiments are shown in Figure 7.19. The antenna was built using copper of 0.254mm thickness, and the shield was built by wires of 0.3mm radius. The feeding arrangement is the same as MED1 shown in Figure 5.1 on Chapter 5.

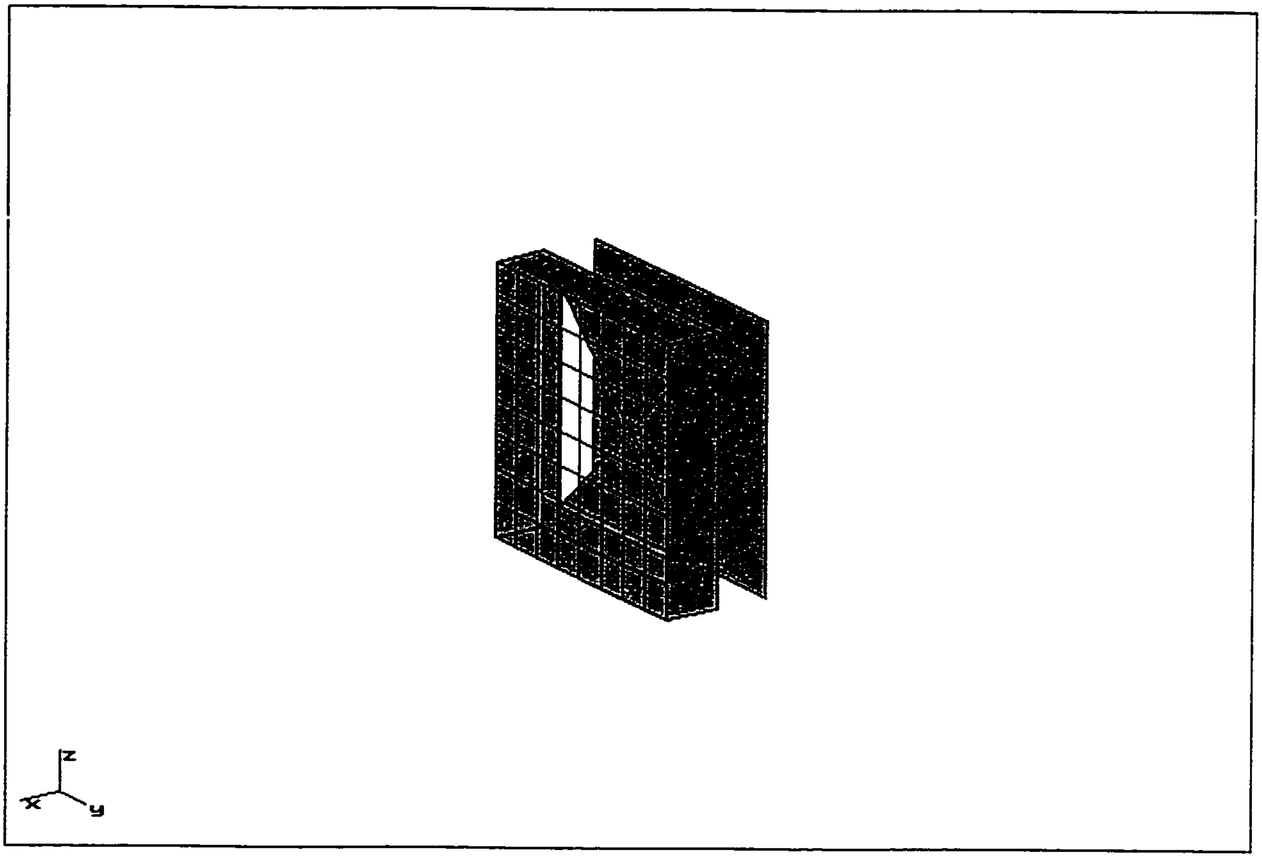

Figure 8.1 Perspective view of SSA8

8.1 Input Impedance and Return Loss

Figure 8.2 shows the input impedance of SSA8 from 0.5GHz to 4.5GHz on a Smith Chart. Figure 8.3 shows the corresponding return loss of SSA8. The 10dB bandwidth is from 2GHz to 2.15GHz where the center frequency is at 2.08GHz. Therefore the 10dB bandwidth is about 6.7% of the center frequency which is quite narrowband.

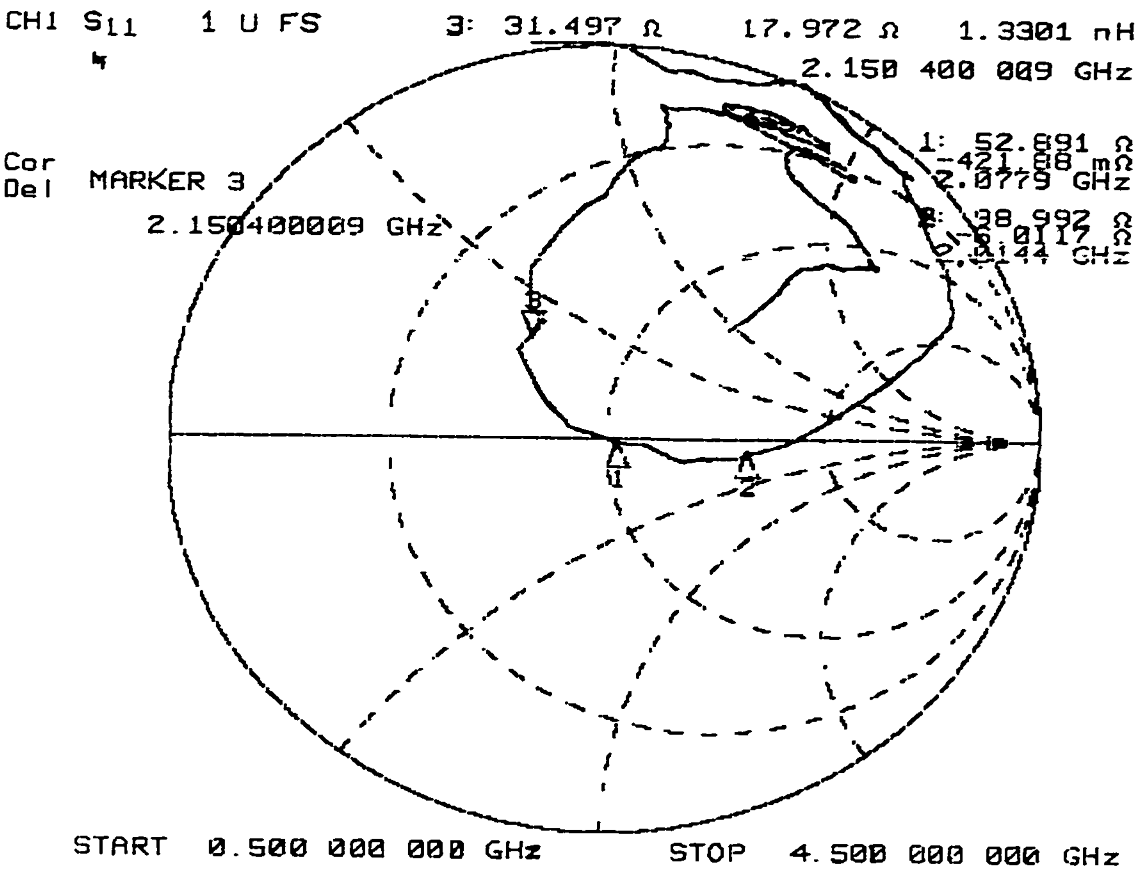

Figure 8.2 Measured input impedance of SSA8

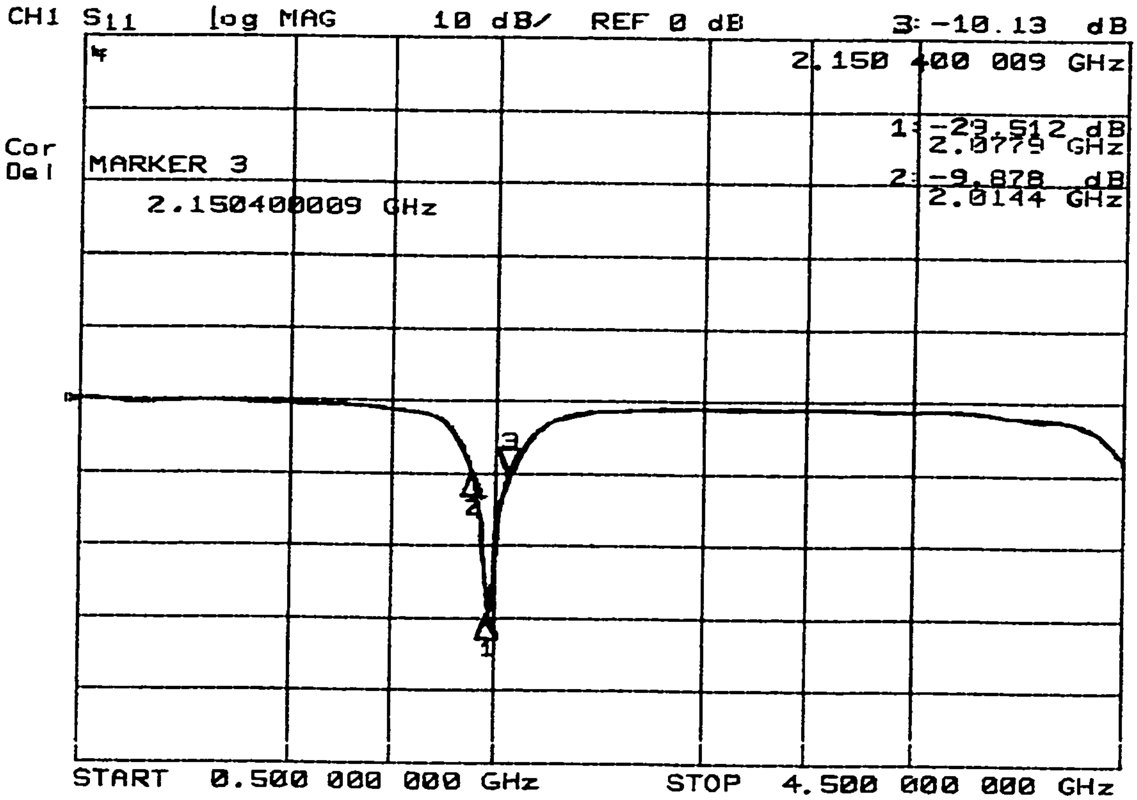

Figure 8.3 Measured return loss of SSA8

8.2 Radiation Pattern

The measurement procedures are described in Section 3.3, and the experimental configuration including the measuring probe antenna are the same as shown in Figure 5.4 in Section 5.1.2. Figure 8.4 shows the radiation pattern of SSA8 on polar graph at 2.08GHz. The maximum is observed at 180° where the measuring probe is directly facing the radiator's side of SSA8. The minima are at 90° and 270°, and there is a small back loop at 0° where the probe is directly facing the shield of SSA8.

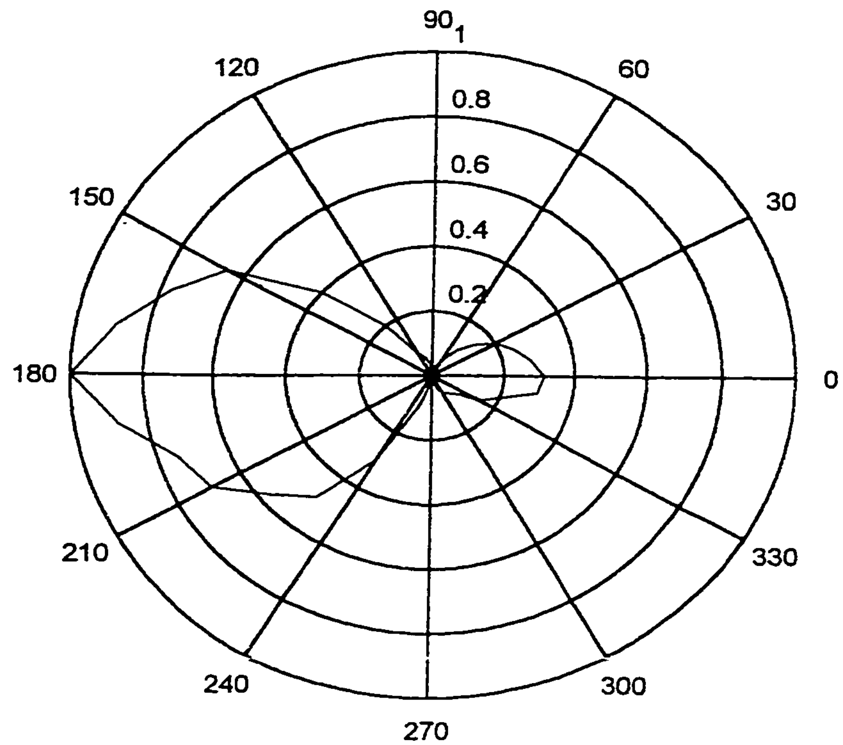

Figure 8.4 Radiation pattern of SSA8 at 2.08GHz

8.3 Near Field

Figure 8.1 shows the coordinate system adopted for this antenna. Figures 8.5 to 8.8 show the normalized S_{21} data in dB on both the radiator side and shield side of SSA8 at 2.08GHz. The x = 0 plane is coincident with the plane containing the "bow-tie" slot. The x = y = z = 0 point is at the center of the gap on the slot. Figure 8.5 shows a comparison of the electric field of the two points which are x cm from each side of the slot along the x-axis (y = 0, z = 0). Comparing the two points which are 2cm from each side of the slot, there is about 13dB or 20 times of radiated power difference. The difference is quite constant as x is increased from each side of the slot. The other three figures give similar information but with the measuring probe moving in different directions instead of the x direction.

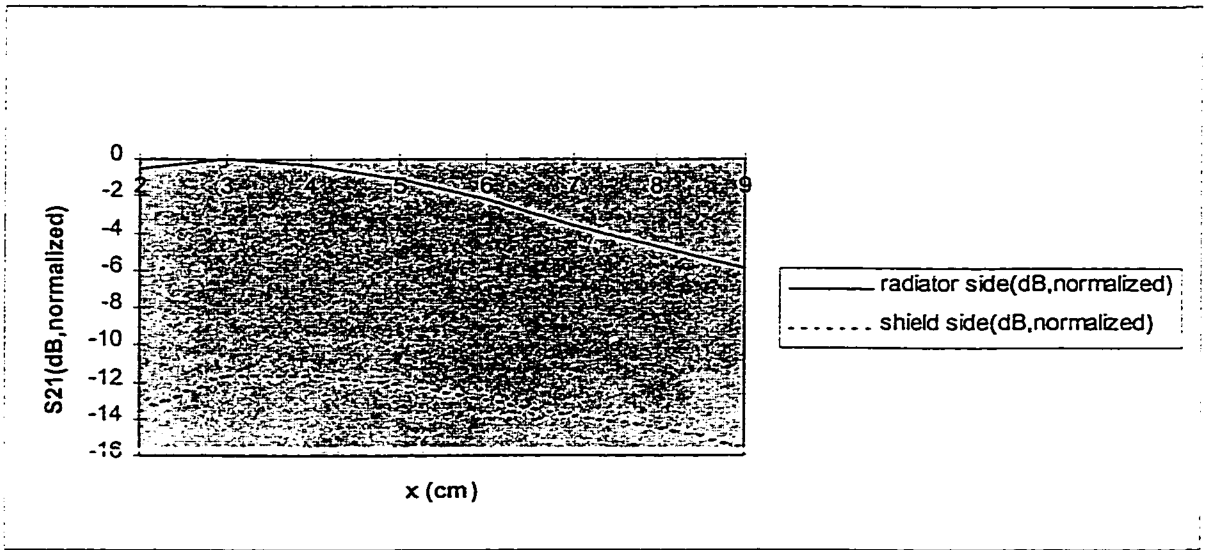

Figure 8.5 Electromagnetic radiation on both sides of SSA8
(y = 0cm, z = 0cm, f = 2.08GHz)

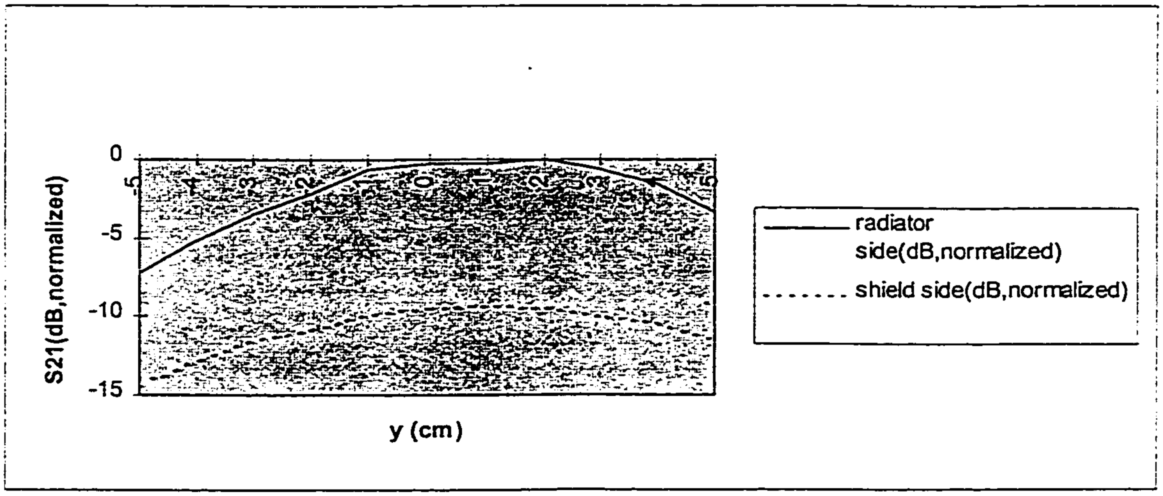

Figure 8.6 Electromagnetic radiation on both sides of SSA8
(x = ± 3cm,z = 0cm, f = 2.08GHz)

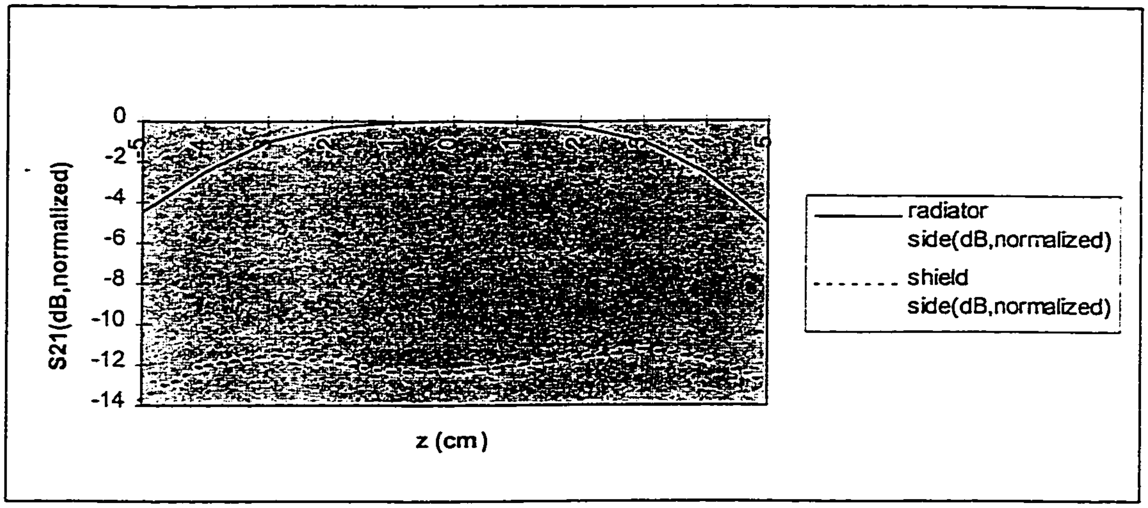

Figure 8.7 Electromagnetic radiation on both sides of SSA8
(x = ± 3cm,y = 0cm, f = 2.08GHz)

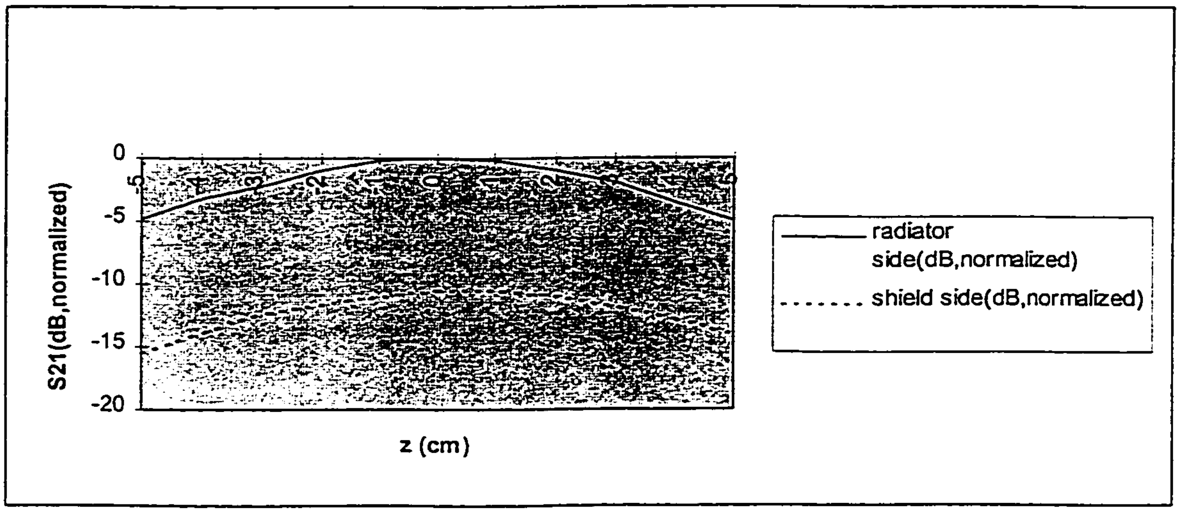

Figure 8.8 Electromagnetic radiation on both sides of SSA8
(x = ± 5cm,y = 0cm, f = 2.08GHz)

Chapter 9: Conclusions

9.1 Magnetic-Electric Dipole

Two novel ultra broadband Magnetic-Electric Dipole Antennas were constructed and tested. The antennas are made up of a parasitic electric dipole (a metallic strip) coupled to a magnetic dipole (a slot).

9.1.1 MED1

MED1 is made from a "bow-tie" strip and a "bow-tie" slot. The overall dimensions of the antenna are 47mm by 47mm by 1mm for the dipole case. For the monopole case, the vertical dimension will be halved. The 10dB return loss BW is over 1GHz from 1.75GHz to 2.78GHz. The bandwidth ratio for VSWR < 2 is 1:1.6. The radiation pattern is symmetric with the maxima at 0° and 180°, and minima at 90° and 270° at lower operating frequencies. At higher frequencies, however, the pattern became nonsymmetrical. The efficiency of the antenna should be above 92% over its operating range judging from the results of MED2.

9.1.2 MED2

MED2 is made from a "folded-H" strip and a "bow-tie" slot. The overall dimensions of the antenna are 58mm by 50mm by 0.2mm for the dipole case. The 10dB BW is over 2.8GHz from 1.15GHz to 3.97GHz. The bandwidth ratio for VSWR < 2 is

1:3.5. The radiation pattern is symmetric with the maxima at 0° and 180°, and minima at 90° and 270° at lower operating frequencies. At higher frequencies, however, the pattern becomes nonsymmetrical. The efficiency of MED2 is above 92% over its operating frequencies.

9.1.3 Transmission line model and WIPL-D simulation

Transmission line model of MED2 gives results that agree well with the experimental measurements; therefore, the method could be used to predict the input impedance of other Magnetic-Electric dipole antennas of different size and shape before physically building the actual antennas. WIPL-D simulation results, on the other hand, did not agree well with the experimental measurements. This might probably due to the exclusion of the low dielectric spacer (instead the dielectric was assumed to be air in our simulations) when simulating the antenna. Also, the excitation model of the antenna was not exactly the same as the actual case.

In conclusion, the two novel ultra-wideband magnetic-electric dipole antennas have achieved their design goals which are compact, mechanically robust and very broad band. They can be transformed into the equivalent monopole structures which are more common and practical than the corresponding dipole structures for portable equipment.

9.2 Shielded Slot Antenna

After simulated various versions of shielded slot antennas, a final version named SSA8 was constructed and tested This novel antenna consists of a "bow-tie" slot as a main radiator, a screen made of wires as a shield, and a metal plate as a re-radiator. The overall dimensions of the antenna are 50mm by 50mm by 20mm for the dipole case. For the monopole case, the size will be halved. The center frequency is at 2.08GHz. The 10dB BW is 6.7% of the center frequency, from 2.01GHz to 2.15GHz. At 2.08GHz, a maximum is observed in the radiation pattern of SSA8 when the radiator's side of the antenna is directly facing toward the measuring probe. Comparing the radiated power on both sides of SSA8, there is over 13dB difference along the x-direction, over 7dB difference along the y-direction, and over 10dB difference along the z-direction.

To conclude, the novel shielded slot antenna (SSA8) has achieved its design goal which is a substantial reduction of radiation on one side of the antenna. Further work should focus on reducing the size of the antenna since eventually we want to integrate the shielded slot antenna into the cellular phone handset. Work should also continue toward increasing the bandwidth of the antenna by building a multiple resonant version of the antenna.

Bibliography

American National Standards Institute, IEEE C95.1-1991: *IEEE Standard for Safety Levels with Respect to Human Exposure to Radio Frequency Electromagnetic Fields, 3 kHz to 300 GHz*, 1991, Piscataway, NJ 08855-1331.

Balanis, C. A. *Antenna Theory : Analysis and Design*, John Wiley & Sons, 1997.

Balzano, Q., O. Garay, and F. R. Steel, "Energy deposition in biological tissue near portable radio transmitters at VHF and UHF," *27th Conference IEEE Vehicular Technology Group*, March 1977.

Brown, G. H., and O. M. Woodward, Jr., "Experimentally determined impedance characteristics of cylindrical antennas," *Proceedings. IRE*, vol. 33, 1945.

Bulter, C. M., and D. R. Wilton, "Evaluation of potential integral at singularity of exact kernel in thin-wire calculations," *IEEE Transactions Antennas Propagation*, vol. AP-23, no. 2, March 1975.

Chatterjee, I., Y. G. Gu, and O. P. Gandhi, "Quantification of electromagnetic absorption in humans from body-mounted communication transceivers," *IEEE Transactions Vehicular Technology*, vol. VT-34, May 1985.

Cleveland, R. F., and W. T. Athey, "Specific absorption rate (SAR) in models of the human head exposed to hand-held UHF portable radios," *Bioelectromagnetic*, vol. 10, Jan. 1989.

Collin, R. E. *Antennas and Radiowave Propagation*, McGraw-Hill, 1985.

Dubost, G. *Flat Radiationg Dipoles and Applications to Arrays*, John Wiley & Sons, 1981.

Foster, K. R. "Health effects of electromagnetic fields: defusing the controversy," *Microwave Journal*, vol. 40, May 1997.

Guy, A. W., and C. K. Chou, "Specific absorption rates of energy in man models exposed to cellular UHF mobile-antenna fields," *IEEE Transactions Microwave Theory Technology*, vol. MTT-34, June 1986.

Hall, P. S. "New wideband microstrip antenna using log-periodic technique," *Electronics Letters*, vol.16, no. 4, Feb. 1980.

Hewlett Packard HP 8720C Network Analyzer Operating Manual, Hewlett-Packard Company, 1992.

Himdi, M., and J. P. Daniel, " Characteristics of sandwich-slotlines in front of a parallel metallic strip," *Electrics Letters*, vol. 27, no. 5, Feb. 1991.

Hizal, A., and Y. K. Baykal, "Heat potential distribution in an inhomogeneous spherical model of a cranial structure exposed to microwaves due to loop or dipole antennas," *IEEE Transactions Microwave Theory Technology*, vol. MTT-26, Aug. 1978.

Jensen, M. A., and Y. Rahmat-Samii, "EM interaction of handset antennas and a human in personal communications," *Proceedings of the IEEE*, vol. 83, no. 1, Jan. 1995.

Johnston, R. H., and J. G. McRory, "An improved small antenna efficiency measurement method," *IEEE AP-S magazine*, Oct. 1998.

Kolundzija, B. M., J. S. Ognjanovic, T. K. Sarkar, and R. F. Harrington, *WIPL-D V1.0 Operating Menu*, Artech House, 1997.

Kumar, G., and K. C. Gupta, "Broad-Band microstrip antennas using additional resonators gap-coupled to the radiating edges," *IEEE Transactions on Antennas and Propagation*, vol. AP-32, no.12, Dec. 1984.

Lo, Y. T., and S. W. Lee, *Antenna Handbook : Antenna Fundamentals and Mathematical Techniques*, Chapman & Hall, 1993.

McRory, J. G. *CAD for Linear and Nonlinear RF/Microwave Circuit Design*, TRLabs, 1996.

Meier, K., V. Hombach, R. Kastle, R. Y. Tay, and N. Kuster, "The dependence of electromagnetic energy absorption upon human-head modeling at 1800MHz," *IEEE Transactions on Microwave Theory and Techniques*, vol. 45, no. 11, Nov. 1997.

Newman, E. H., P. Bohley, and C. H. Walter, "Two methods for the measurement of antenna efficiency," *IEEE Transactions on antenna & propagation*, vol. AP-23, no. 4, July 1975.

Okoniewski, M., and M. A. Stuchly, "A study of the handset antenna and human body interaction," *IEEE Transactions on Microwave Theory and Techniques*, vol. 44, no. 10, Oct. 1996.

Pozar,D. M., and B. Daufman, "Comparison of three methods for the measurement of printed antenna efficiency," *IEEE Communications*, vol. 36, no. 1, Jan. 1988.

Sanchez-Hernandez, D., and I. D. Robertson, "A survey of broadband microstrip patch antennas," *Microwave Journal*, Sept. 1996.

Stuchly, M. A., A. Kraszewski, S. S. Stuchly, G. W. Hartsgrove, and R. J. Spiegel, "RF energy deposition in a heterogeneous model of man: Near-field exposures," *IEEE Transactions Biomedical Engineering*, vol. BME-34, Dec. 1987

Stuchly, S. S., M. A. Stuchly, A. Kraszewski, and G. W. Hartsgrove, "Energy deposition in a model of man: Frequency effects," *IEEE Transactions Biomedical Engineering*, vol. BME-33, July 1986, pp.702-711.

Terret, C., M. Himdi, and J. P. Daniel, "Transmission line analysis of aperture-coupled microstrip antenna," *Electronic Letters*, vol. 25, no.18, Aug. 1989.

Wheeler, H. A. "The radiansphere around a small antenna," *Proceedings IRE*, Aug. 1959.

Wilton, D. R., and C. M. Bulter, "Efficient numerical techniques for solving Pocklington's equation and their relationships to other methods," *IEEE Transactions Antennas Propagation*, vol. AP-24, no.1, Jan. 1976.

Yazidi, M. E., M. Himdi, and J. P. Daniel, "Transmission line analysis of nonlinear slot coupled microstrip antenna," *Electronic Letters*, vol. 28, no.15, July 1992.